

STUDY AND DESIGN OF ARRAY AND BEAMSTEERING ANTENNAS FOR
MILLIMETER WAVE BAND APPLICATIONS

by

Saeideh Shad



A dissertation

submitted in partial fulfillment

of the requirements for the degree of

Doctor of Philosophy in Electrical and Computer Engineering

Boise State University

August 2021

© 2021

Saeideh Shad

ALL RIGHTS RESERVED

BOISE STATE UNIVERSITY GRADUATE COLLEGE

DEFENSE COMMITTEE AND FINAL READING APPROVALS

of the dissertation submitted by

Saeideh Shad

Dissertation Title: Study and Design of Array and Beamsteering Antennas for millimeter wave Band Applications

Date of Final Oral Examination: 20 April 2021

The following individuals read and discussed the dissertation submitted by Saeideh Shad, and they evaluated their presentation and response to questions during the final oral examination. They found that the student passed the final oral examination.

Hani Mehrpouyan, Ph.D. Chair, Supervisory Committee

Wan Kuang, Ph.D. Member, Supervisory Committee

Hao Chen, Ph.D. Member, Supervisory Committee

Payam Nayeri, Ph.D. External Examiner

The final reading approval of the dissertation was granted by Hani Mehrpouyan, Ph.D., Chair of the Supervisory Committee. The dissertation was approved by the Graduate College.

To my parents who sacrificed too much for me.

ACKNOWLEDGMENTS

It was a wonderful journey doing my PhD at Boise State University, I enjoyed every single moment of it, burning the midnight oil at the office, exciting moments of achieving simulation and experimental results, and early morning jogging on the Greenbelt. I would like to thank to those who were with me on this wonderful journey. First of all, I would like to express my special appreciation and thanks to my adviser, Dr. Hani Mehrpouyan, for giving me this opportunity to work in your research group. Many thanks for your invaluable supervision, motivation, and insightful encouragement during the whole period. You always gave me freedom on choosing my research topics and supported me in my research from idea to implementation. Thanks for lots of advice with great patience.

I would also like to thank my committee members, Dr. Hao Chen, and Dr. Wan Kuang. I always enjoyed my technical discussions with them during courses that I took with them.

Also, I would like to thank all members in our group for your help and friendship.

I would like to extend my thanks to Chris Davis and Philip Boysen for your helpful technical assistance and for the hours and days you spent antenna prototyping.

Finally, at the end, I would like to express a deep sense of gratitude to my lovely family - my mother, father, sister, and brother, for being with me. Thank you for your support, prayers, and inspiration. I am much indebted to my parents, your affection and perseverance are always with me on my life's journey.

ABSTRACT

Millimeter wave (mmWave) communication systems have attracted significant interest regarding supporting high data rate of Gigabit/s communications for the new generation of wireless communication networks. MmWave communication systems have frequency ranges in between 30 and 300 GHz wherein an enormous amount of unused bandwidth is available. Although the available bandwidth of mmWave frequencies is promising for high data rate communications, the propagation characteristics of mmWave frequencies are significantly different from microwave frequency band in terms of path loss, diffraction and blockage, and atmospheric absorption. In general, the overall losses of mmWave signals are significantly larger than that of microwave signals in point-to-point wireless communications. To compensate the high propagation losses, due to the limited output power that the current RF active components can deliver in millimeter waves, the use of directional and beam-steerable antennas become necessary in mmWave wireless systems. The use of directional antennas can effectively alleviate the signal interference in mmWave communications. High-gain directional antennas can be used at both the transmitting and receiving ends, resulting in a significantly enhanced Signal-to-Noise ratio (SNR) and improved data security, and can be used in long-range mmWave point-to-point communications. Moreover, directional antenna beams with limited spatial coverage need to be steered either electronically or mechanically to obtain a better substitute link for non-Line of Loss (LOS) communications. Therefore, this dissertation mainly focuses on antenna design for mmWave frequency band applications. High gain and beam-steerable

antennas with the merits of low profile, high gain, high efficiency and low cost are studied to address the new challenges of high frequency band antennas. First, waveguide-based technology is employed to propose a new wideband high gain antenna for 60 GHz band applications. Then, for beam-steerable antenna applications to steer the antenna beam in a specific direction, different structures of cylindrical lens antennas are studied. First, a compact two-dimensional lens antenna is designed and proposed at 28 GHz, and then a possible design of a wideband beam-steerable lens antenna is discussed and presented. Finally, a fully metallic wideband metasurface-based lens antenna is explored. The antenna is realized based on an array of periodic unit-cells to reduce the loss of the dielectric part in the conventional lens antennas. This property is exploited to design wideband cost-effective fully metallic antenna at mmWave frequencies.

TABLE OF CONTENTS

ACKNOWLEDGMENTS	v
ABSTRACT	vi
LIST OF TABLES	xi
LIST OF FIGURES	xii
LIST OF ABBREVIATIONS.....	xviii
CHAPTER ONE: INTRODUCTION.....	1
1.1 Pass to MmWave Communications	1
1.2 Challenges at mmWaves	3
1.2.1 Free space pass loss (FSPL)	3
1.2.2 Atmospheric losses	4
1.2.3 Blockage, and scattering effects	5
1.3 Research Objectives	5
1.4 Dissertation outline	7
CHAPTER TWO: HIGH GAIN ANTENNA AT MMWAVE FREQUENCIES	8
2.1 Introduction	8
2.2 Planar Antenna Array.....	10
2.3 Slotted waveguide array antenna	14
2.4 Gap waveguide array antenna.....	18
CHAPTER THREE: 60 GHZ WAVEGUIDE-FED ARRAY ANTENNA BY MULTI- STEPED SLOT APERTURE	22

3.1	Introduction.....	22
3.2	Antenna Design and Configuration.....	22
3.3	Basic Subarray design	24
3.4	Feeding Network.....	25
3.5	Dielectric Loading.....	26
3.6	Experimental Results.....	34
3.7	Assembly Consideration.....	38
3.8	Conclusion	40
CHAPTER FOUR: MULTIBEAM LENS ANTENNA ARRAY		42
4.1	Background.....	42
4.2	Lens Antenna	44
4.3	Luneburg Lens	48
4.3.1	Basic operation of Luneburg lens	50
4.4	Cylindrical Luneburg Lens Antenna	53
4.4.1	Geodesic lens	54
4.4.2	Cylindrical LL based on partially filled - air filled Parallel Plate Waveguide	55
4.4.3	Metal-posts as an Artificial Dielectric Material.....	56
CHAPTER FIVE: BEAM-STEERING LENS ANTENNA FOR POINT TO MULTIPOINT COMMUNICATIONS AT 28 GHZ BAND		59
5.1	Introduction.....	59
5.2	Analysis and Design of the Multi-Beam Lens	61
5.3	Feed Design.....	62
5.4	Lens Design.....	63

5.5	Experimental Results	67
5.6	Conclusion.....	71
CHAPTER SIX: WIDEBAND BEAM-STEERABLE CYLINDRICAL LENS ANTENNA WITH COMPACT INTEGRATED FEED ELEMENT.....		72
6.1	Introduction	72
6.2	Analysis and Design of the Multi-Beam Lens.....	73
6.2.1	Feed Design.....	73
6.2.2	Lens Design.....	75
6.3	Single feed element integration with the lens.....	77
6.4	Multi-beam	78
6.5	Experimental Results	81
6.6	Conclusion.....	85
CHAPTER SEVEN: WIDEBAND METALLIC CYLINDRICAL LENS ANETNAN ..		87
7.1	Introduction	87
7.2	Electromagnetic waves in Periodic structures.....	89
7.3	Unit Cell of Periodic Structures.....	94
7.4	Effective Refractive Index.....	95
7.5	Unit Cell Design	96
7.6	Lens Design	100
7.7	Measurement results	108
CHAPTER EIGHT: CONCLUSIONS		113
8.1	Summary	113
8.2	Future Work.....	115
REFERENCES		117

LIST OF TABLES

Table 2.1.	Planar array antenna at mmWave band.	14
Table 3.1.	Design Parameters For 4×4–Element Array	34
Table 4.1.	Lens Classification Based On Physical Characteristics.	46
Table 5.1.	Radiation characteristics of the nine individual ports of the proposed antenna	69

LIST OF FIGURES

Figure 1.1	MmWave region of the electromagnetic spectrum.....	3
Figure 1.2	Average sea level atmospheric absorption at mmWave frequencies.....	5
Figure 2.1	(a). Corporate Feed Network. (b). Inline series Feed Network	11
Figure 2.2	(a). Substrate Integrated Waveguide, (b). Rectangular hollow waveguide structure.....	13
Figure 2.3	Geometry of the most common slotted waveguide antenna [1].	15
Figure 2.4	(a) Surface Currents distribution for TE₁₀ mode in rectangular waveguide walls [1]. (b) Sensitive and least-sensitive places for joining walls. [3]...	16
Figure 2.5	Surface current distortion in slotted waveguide antennas. (a) Current cut in broad-wall slot antenna. (b) Narrow-wall slot antenna without the problem of disturbing current. (c). Flatness problem	17
Figure 2.6	Antenna configuration in [2]	17
Figure 2.7	Basic principle operation of gap waveguide. (a) PEC – PMC Parallel plate electromagnetic wave Cut off (b) TEM local waves propagation [3].....	19
Figure 2.8	Different gap waveguide geometries and desired modes of propagation. (a) Ridge gap waveguide. (b) Groove gap waveguide. (c) Microstrip gap waveguide. (d) Inverted-microstrip gap waveguide [4].....	19
Figure 2.9	A ridge waveguide-fed Patch Antenna Array[5].	21
Figure 2.10	The schematics of the three 16×16 slot array designed in gap waveguide technology. (a). Groove gap waveguide slot array. (b). Ridge gap waveguide slot array. (c). Inverted microstrip gap waveguide slot array. [65].....	21
Figure 3.1.	Configuration of the proposed cavity-backed 4 × 4 slot array antenna. ...	23
Figure 3.2.	2 × 2-element slot aperture array.....	24

Figure 3.3.	Exploded view of the proposed cavity-backed 2×2 subarray	24
Figure 3.4.	Feeding cavity of the array ($wa \times la = 2.2 \text{ mm} \times 4 \text{ mm}$, $wb \times lb = 1 \text{ mm} \times 4 \text{ mm}$, $wn = 13.3 \text{ mm}$). (b) Magnetic field distribution in the cavity. ..	25
Figure 3.5.	a) Simulated reflection coefficient for different values of l_b with fixed value of $w_b = 1 \text{ mm}$. (b). Simulated reflection coefficient for different values of w_a with fixed value of $w_b = 1 \text{ mm}$, $l_b = 3.8 \text{ mm}$, and $l_a = 4 \text{ mm}$	26
Figure 3.6.	Reflection coefficient of the antenna for different values of the d parameter (dielectric plate separation from the aperture).....	28
Figure 3.7.	Radiation pattern of the antenna for different values of the d parameter (dielectric plate separation from the aperture) in E- and H- planes.	28
Figure 3.8.	Electrical filed distribution over the aperture of the antenna.....	29
Figure 3.9.	Simulated radiation pattern in E- and H-planes at (a) 58, (b) 60, (c) 62, (d) 64 GHz.....	31
Figure. 3.10.	Simulated realized gain of proposed antenna with and without dielectric layer	32
Figure 3.11.	Configuration of the 8×8 -element array antenna.....	32
Figure 3.12.	Simulated radiation pattern in E- and H-planes at (a) 58, 60 GHz, (b) 62, 64 GHz.....	33
Figure 3.13.	Simulated realized gain performance of the 8×8 -elemen array antenna...	33
Figure 3.14.	Prototype of the proposed array antenna.	34
Figure 3.15.	Comparison of simulated and measured input reflection coefficient of the fabricated prototype.....	35
Figure 3.16.	Simulated and measured radiation patterns in E- and H-planes at (a) 58, (b) 61, and (c) 64 GHz.....	36
Figure 3.17.	Frequency behavior of directivity, gain, and efficiency.	37
Figure 3.18.	Frequency response of the antenna with parametric study of wb parameter	39
Figure 3.19.	The effects of the height of layer composed of coupling slots	39

Figure 3.20.	Illustration for analysis of misalignment of the proposed array antenna ..	40
Figure 3.21.	Simulated reflection coefficient characteristics of the structure considering misalignment.	40
Figure 4.1.	Focusing antennas: (A) lens; (B) reflector	46
Figure 4.2.	(a) Off-body feed homogenous lens and (b) an integrated feed Luneburg lens.	47
Figure 4.3.	Shaped integrated dielectric lens antenna.	47
Figure 4.4.	Luneburg lens ray tracing paths for three different points on the sphere/cylinder perimeter, each shown in a separate colour	50
Figure 4.5.	Refractive index variation of a standard Luneburg lens [6].....	51
Figure 4.6.	Half hemisphere Luneburg lens.....	53
Figure 4.7.	Cylindrical Luneburg lens.	53
Figure 4.8.	(a) Antenna configuration, (b) Multi-beam radiation pattern.....	55
Figure 4.9.	LTSA-fed cylindrical Luneburg lens antenna	56
Figure 4.10.	(a)-(f) Cross-section view of possible profiles of cylindrical Luneburg lens.	56
Figure 4.11.	Air-filled symmetric parallel-plate waveguide modified Luneburg lens ..	57
Figure 4.12.	Surface-wave structure with (a) square metal posts and (b) cylindrical metal posts.	57
Figure 4.13.	Geometry of the PBG structure with (a) a 3D view of the periodic and regular square metal posts in square lattice in a parallel-plate waveguide and (b) the cross-sectional view and transverse resonance equivalent circuit of the structure. (c) Cross-sectional view of the rotationally symmetric corrugated flare [103].	58
Figure 4.14.	APWLLs with circular posts. (a) Top view with square lattice (b) Top view with hexagonal lattice. (c) Cross-sectional view: $D=0.38$ mm, $P=0.78$ mm, $h= 1.9$ mm.	58
Figure 5. 1.	View of the Antenna structure. The optimized parameters are: $h1 = 1$ mm, $h2 = 1.2$ mm, $w1 = 2.2$ mm, $l0 = 1$ mm, $l1 = 4$ mm, $l2 = 3$ mm, $wf = 7$ mm, $hf = 3$ mm, $R = 50$ mm, $h = 5.3$ mm	62

Figure 5.2.	Simulated antenna radiation patterns in H- and E-planes for optimized value of <i>R_{plateR_{lens}}</i>	66
Figure 5.3.	The simulated radiation patterns at 28 GHz of the single feed element....	66
Figure 5.4.	(a) Simulated reflection coefficients and mutual couplings of the proposed PPW lens, (b) Simulated H-plane Co-Pol broadside radiation patterns of the proposed PPW lens antenna at representative scan angles.	67
Figure 5.5.	Prototype of the proposed array antenna	68
Figure 5.6.	The measured, (a) input reflection coefficient for all ports and, (b). port coupling coefficients of the fabricated prototype.....	69
Figure 5.7.	The measured plane radiation patterns of the fabricated PPW LL antenna at 28 GHz.	69
Figure 5.8.	Simulated and Measured antenna directivity and gain for all ports of the fabricated PPW LL antenna.	70
Figure 6.1.	Antenna configuration.	73
Figure 6.2.	Simulated reflection coefficients of the antenna when the matching pin is loaded in the waveguide.	75
Figure 6.3.	Co- and Cross-polarizations radiation patterns of the single-fed PPW Luneburg-based lens for different frequencies in, (a) H-plane, (b) E-plane.	77
Figure 6.4.	Simulated, (a) reflection coefficients of multiple feed elements, (b) mutual coupling between adjacent feeds.....	79
Figure 6.5.	Simulated E-field distribution by activating center and edge feeds at (a). 24 GHz, (b). 38 GHz	80
Figure 6.6.	Simulated Co-Pol radiation patterns of the antenna at different frequencies for feed elements in the H-plane	80
Figure 6.7.	Simulated antenna realized gain for center feed.	81
Figure 6.8.	Prototype of the proposed multibeam lens antenna.....	82
Figure 6.9.	The measured frequency response of the antenna, (a), measurement setup (b) input reflection coefficient for all ports and, (c). port coupling coefficients between adjacent ports of the fabricated prototype.	84

Figure 6.10.	Fabricated antenna setup in an anechoic chamber	85
Figure 6.11.	The measured H-plane radiation patterns of the fabricated PPW LL antenna at Ka-band.....	86
Figure 7.1.	Primitive unit cell.....	90
Figure 7.2.	Periodic array of unit cell and direct lattice vectors in x and y direction..	91
Figure 7.3.	Reciprocal lattice vectors	92
Figure 7.4.	Brillouin zone; the primitive unit cell in reciprocal space	92
Figure 7.5.	Irreducible Brillouin Zone; Brillouin zone symmetry in (a). up/down, (b). left/right, (c). 90-degree rotational symmetry.	92
Figure 7.6.	Key points of symmetry on Brillouin zone	93
Figure 7.7.	A typical unit cell in periodic metasurface.....	97
Figure 7.8.	The irreducible Brillouin zone for the proposed unit cell in HFSS.	97
Figure 7.9.	Effective refractive index for a square pin-unit cell when h is varied. The other parameters are $p = 1.4 \text{ mm}$, $g = 0.3 \text{ mm}$, $a = 0.8 \text{ mm}$	99
Figure 7.10.	Effective refractive index for a square unit cell when g is varied and $p = 1.4 \text{ mm}$, $a = 1.4 \text{ mm}$, $h = 0.8 \text{ mm}$	99
Figure 7.11.	Effective refractive index for the proposed unit cell, where $a = 0.8 \text{ mm}$, $h = 0.8 \text{ mm}$, $p = 1.4 \text{ mm}$, $g = 0.3$	100
Figure 7.12.	The full metal cylindrical Luneburg Lens Antenna configuration with top and bottom plates.	103
Figure 7.13.	Description of antenna parameters. $W = 66 \text{ mm}$, $R0 = 50 \text{ mm}$, $h0 = 4.4 \text{ mm}$, $ht = 2 \text{ mm}$, $hb = 3.15 \text{ mm}$, $g = 0.3 \text{ mm}$, $Ww = 7 \text{ mm}$, $hw = 3.55 \text{ mm}$, $hin = 2 \text{ mm}$, $hm = 2 \text{ mm}$, $hf = 1.2 \text{ mm}$, $wm = 1.6 \text{ mm}$, $lm = 2.5 \text{ mm}$, $h0$	104
Figure 7.14.	Simulated reflection coefficients of the antenna	105
Figure 7.15.	Antenna radiation pattern in different frequencies at : (a) H-plane, (b) E-plane	106
Figure 7.16.	(a) 3D radiation pattern of antenna at 30GHz, (b). Pattern of E-plane (YZ plane), (c). Pattern of H-plane (XY Plane).....	107

Figure 7.17.	Realized Gain of the proposed antenna	107
Figure 7.18.	Fully metallic cylindrical Luneburg lens antenna prototype made of aluminum with CNC mill.	108
Figure 7.19.	Measured input reflection coefficient of the fabricated prototype.....	109
Figure 7.20.	Comparison of simulated and measured input reflection coefficient of the fabricated prototype.....	109
Figure 7.21.	Radiation pattern setup in the anechoic chamber.....	110
Figure 7.22	Measured radiation patterns in E- and H-planes at (a) 26, 30, 34, 38 GHz.	110
Figure 7.23.	Measured radiation patterns in E-plane at (a) 26, 28, 30, 34, 38 GHz. ...	111
Figure 7.24.	Measured peak realized gain and directivity	112

LIST OF ABBREVIATIONS

mmWave	millimeter wave
SNR	Signal to Noise Ratio
SINR	Signal to interference plus Noise Ratio
LOS	Line of Sight
NLOS	None Line of Sight
ETSI	European Telecommunications Standards Institute
FCC	Federal Communications Commission
FSPL	Free Space Path Loss
WPAN	Wireless Personal Area Network
AMTS	Automated Maritime Telecommunications System
LTE	Long-Term Evolution
4G	Fourth Generation
5G	Fifth Generation
LL	Luneburg Lens
2D	Two Dimensional
SIW	Substrate Integrated Waveguide
PEC	Perfect Electric Conductor
PMC	Perfect Magnetic Conductor
GWG	Gap Waveguide
LTCC	low temperature co-fired ceramic

PPW	Parallel plate waveguide
GRIN	Graded index
TM	Transverse Magnetic

CHAPTER ONE: INTRODUCTION

1.1 Pass to MmWave Communications

The rapid increase of mobile data growth and the use of smartphones are creating unprecedented challenges for wireless communication systems. Wireless communications generations from the Automated Maritime Telecommunications System (AMTS)/ Nordic Mobile Telephone (NMT) first generation (1G) through the Long-Term Evolution (LTE) fourth generation (4G) have worked with essentially limited bandwidth. They are limited to a carrier frequency spectrum ranging between 700 MHz and 2.6 GHz. To overcome a global bandwidth shortage to deliver high quality, low latency video and multimedia applications for wireless devices, wireless carriers require support with a new wireless spectrum beyond the 4G standard. Even with the advances of 4G LTE, the network is running out of bandwidth and suffering from traffic growth over the years. A fast growing number of users want more services that consume ever-increasing bandwidth. The solution is to add more bandwidth to wireless networks [7]-[8]. MmWave wireless communications is the next breakthrough frontier for wireless networks in the mobile cellular industry, for emerging wireless local area networks, personal area networks, and for vehicular communication [9].

The fifth generation (5G) of wireless systems open up to more spectrum at untapped mmWave frequency bands. The use of high frequency bands could allocate more bandwidth for data commutations. This leads to delivery of faster, higher-quality video and multimedia contents. MmWave generally corresponds to the radio spectrum between 30

GHz to 300 GHz, with wavelengths between one and ten millimeters. Figure 1.1 shows mmWave spectrum for the next generation of wireless networks. There is a large amount of unused spectrum at these higher frequencies and it will alleviate concerns about wireless traffic congestion. Furthermore, wireless systems will support mobile data rates of several gigabits per second, which is thousands of times greater than today's cellular and WiFi networks [9].

In recent years, the standardization regulatory bodies such as the European Telecommunications Standards Institute (ETSI) and the United States Federal Communications Commission (FCC), have directed their attention towards five mm-wave frequency bands as the main candidates for 5G backhauling:

- 28 GHz (27.5-29.5 GHz)
- 38 GHz (37.5-40 GHz)
- 42 GHz (40.5-43.5 GHz)
- V-band (ETSI: 57-66 GHz , FCC: 57-71 GHz)
- E-band (71-76 GHz & 81-86 GHz)

The use of mmWave frequencies is growing in many applications such as automotive anti-collision radar at 77 GHz [10], vehicle-to-vehicle communication [11], high resolution mmWave [12], satellite cross-link communication in space [13], indoor wireless data transmission at 60 GHz, and outdoor millimeter point-to-point backhaul terminals [14].

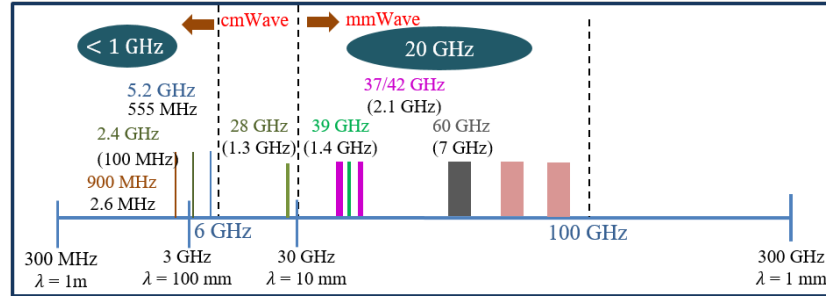


Figure 1.1 MmWave region of the electromagnetic spectrum

1.2 Challenges at mmWaves

There are challenges associated with operating in mmWave frequency bands that need to be addressed. In microwave systems, transmission loss is accounted for principally by the free space loss. However, in mmWave bands additional loss factors come into play. As a result of the propagation characteristics at mmWave frequencies, three distinct challenges arise [15] [16]:

- High level of free space path loss
- Absorption loss due to atmospheric gases and rainfall
- Blockage, and scattering effects

1.2.1 Free space pass loss (FSPL)

According to the Friis transmission equation, the power transmitted from one antenna is received by another antenna under idealized conditions in a certain distance is given by [17]:

$$P_r = P_t + G_t + G_r + 20 \log_{10}\left(\frac{\lambda}{4\pi R}\right) \quad (1.1)$$

where P_r is the receiving signal output power, P_t is the transmitting signal output power, G_r and G_t are the receiving and transmitting antenna gains, and λ is the wavelength, and R is the distance between the antennas. In fact, free-space path loss (FSPL) is more critical

in mmWave spectrum than lower frequencies due to a limitation related to their wavelength. For example, comparing FSPL in a 60 GHz system with those in both conventional 2.4 GHz and 5 GHz, the 60 GHz link suffers 27.96 dB and 21.58 dB higher loss than 2.4 GHz and 5 GHz respectively. This loss affects the link budget and becomes a huge challenge when transmitting over a large distance. For a given power, the shorter the wavelength, the shorter the transmission range [18]. In order to improve signal to noise ratio (SNR) at the receiver and thereby increase the transmission range we need to increase the power of the transmitting signal, or use more directive antennas. Due to the limited output power that the current active components can deliver in mmWaves, we can only increase the antennas gains in order to increase the communication distance and compensate FSPL. Therefore, high gain and low loss antenna is one of the most necessary components of mmWave short- and long-range wireless communication systems.

1.2.2 Atmospheric losses

Moreover, transmission losses occur when mmWave traveling through the atmosphere. Figure 1.2 depicts average atmospheric losses at mmWave frequencies in dB/km. These losses are greater at certain frequencies. For example, as shown in Figure 1.2, absorption loss, due to atmospheric gases such as molecules of oxygen, water vapor and other atmospheric gaseous, reaches its peak value at a frequency of 60 GHz. At mmWaves, the size of raindrops, are significant compared to the wavelength. For raindrops, the size introduces severe energy losses, depending on the magnitude of the rainfall [19]. Considering the amount of the atmospheric losses at mmWaves, these frequencies can be used for various secure short and long rang wireless communications. For instance, due to the high atmospheric absorption at 60 GHz, relatively secure high data

rate communications with a low probability of intercept can be performed for short range point-to-point wireless systems such as local area networks. On the other hand, according to Figure 1.2 the negligible atmospheric absorption at 28 and 38 GHz make these frequencies good candidates for long-range radio links in the emerging 5G cellular.

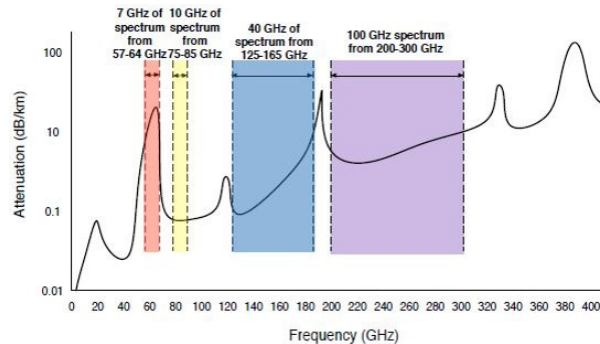


Figure 1.2 Average sea level atmospheric absorption at mmWave frequencies

1.2.3 Blockage, and scattering effects

In addition, in wireless networks, signals at mmWave frequencies due to the very short wavelength are more susceptible to blockage and interference compared to low frequency waves. For example, obstacles such as walls, humans and objects have high penetration losses at mmWave. This means that obstacles can easily disrupt mmWave signals. This forms the major challenge to the use of mmWave frequencies in 5G systems [3].

1.3 Research Objectives

In order to address three aforementioned challenges, the above facts and unique characteristics of mmWave frequency, it is generally agreed that the SNR reduces considerably due to the extreme losses at high frequencies applications. Therefore, according to the Friis transmission equation, due to the limited power of commercial mmWave transmitters, in order to support the advancement of mmWave band for wireless

communications, and improve SNR at the receiver and thereby compensate for the high propagation losses and increase the transmission range, the use of high-gain antennas are required. This results in a significantly enhanced SNR and improved data security, which can be used in short- and long-range mmWave point-to-point communications systems.

Furthermore, the objective of this dissertation is to demonstrate the feasibility of designing high-gain and beam steerable antennas in the millimeter-wave range. More specifically, this work focuses on the following points:

1. In the first part of this dissertation, we focus on the design, fabrication, and measurement of high-gain multilayer waveguide-based antenna operating within 60 GHz for high-speed communication systems. We introduce the subject and the background needed in order to better understand the operation of the antenna. Some of the traditional transmission line issues and challenges at high frequencies are discussed in this section. The antenna structure with simple mechanical assembly and low loss property is demonstrated and each part of the antenna explained.
2. In the second part of the dissertation, the design and fabrication of high-gain beam-steerable Luneburg-based lens antennas operating within the 28 GHz band, and Ka-band (26.5 GHz-40 GHz) are demonstrated for high-gain and multi-beam applications. The antennas with fan-beam property are designed based on the utilization of thin dielectric materials, and metasurface technology forming cost-effective wideband properties.

1.4 Dissertation outline

This dissertation is outlined as follows:

- Chapter 2 outlines different designs and technologies of high gain antennas used for mmWave applications. It introduces the background of the investigation on millimeter-wave antennas and arrays.
- Chapter 3 outlines the design, fabrication process flow, and measurements of a waveguide-based high gain antenna array operating within the 60 GHz band.
- Chapter 4 outlines an overview of lens antennas. Different structures of cylindrical Luneburg lens antennas are presented and discussed.
- Chapter 5, 6, and 7 outlines the design, fabrication, and measurements of narrow band and wideband lens antennas operating within the 28 GHz and Ka-band (26.5 GHz-40 GHz).
- Chapter 8 concludes the results of this research and discusses future advancements and applications.

CHAPTER TWO: HIGH GAIN ANTENNA AT MMWAVE FREQUENCIES

2.1 Introduction

In recent years, due to the emergence of high data rate communications there have been significant developments on multi-Gigabit wireless communication systems in V-band (40 GHz to 75 GHz), E-band (60 GHz to 90 GHz) and W-band (75 GHz to 110 GHz). For example, the 7GHz of unlicensed band around 60 GHz offers significant opportunities for applications such as high-speed short-range wireless personal area network (WPAN) communications and real time video streaming at rates of several Giga bite per second (Gbps). However, a major issue in designing such a high data rate 60 GHz radio is the limited link budget over indoor distances, especially for non-line-of-sight (NLOS) situations. Therefore, to ensure a sufficient link budget at mmWave band, due to the high propagation path loss, high noise figure of the receiver and low output power of the transmitter, we can only increase the antennas gain in order to increase the communication distance and compensate free-space path losses. High gain antennas with fixed beams are the most essential components for short- and long-range communication systems in mmWave band. This enables high S/N ratio for point-to-point high-speed data communications [3].

Typical antennas for high gain applications are reflector, and horn antennas [20], providing excellent high gain performance. Existing approaches, depending on the required gain, are rather expensive, bulky, and heavy for commercial mmWave systems. The design

of antenna array at mm-wave frequencies is a very complex job and includes several design challenges [21]:

- The size of the antenna array should be reduced to integrate the whole array in portable high frequency devices. The small size of the array structure increases the fabrication error and complexity. In addition, to achieve the desired high gain performance and avoid the grating lobes, the inter-element spacing is kept small. The close proximity of these elements causes high mutual coupling which degrades the array performance. The mutual coupling is an important issue, which needs special attention. Different mechanisms are chosen to reduce the mutual coupling.
- The losses in the feed lines of the array become appreciable in mm-wave frequencies and need special care in the design. This high loss reduces the system sensitivity and efficiency.
- The antenna array is desired to be integrated with other components e.g. the front end detector and amplifier circuits for the implementation of low cost mm-wave systems. Different antenna integration technologies e.g. system-on-chip, system-in-package or standard laminate substrates are chosen according to the nature of application and gain requirement [16]. This requires the meticulous selection of the antenna materials with known characteristics and low loss at mm-wave frequencies. Also the electromagnetic interference between the antennas and other front end modules hamper the operation of both the antennas and circuits.

For achieving promising trade-off between high performance and cost, various types of high gain mmWave antennas such as printed antenna arrays, waveguide-based slot arrays, and gap waveguide arrays are investigated in the following sections. Different

structures and the challenges regarding the practical implementation of designs are introduced and discussed.

2.2 Planar Antenna Array

Primarily, planar array antennas are one of the most popular types of array antenna. Planar array with different configurations including dipole [22], Yagi-Uda [23], and leaky-wave [24] are popularly developed and implemented in wireless devices over a wide range of frequencies at microwave frequencies, due to their remarkable features such as low profile, low cost and ease of manufacturing. Although, planar antenna arrays are usually the preferred choice because of the ease of fabrication/integration and costs, they suffer from design complexity and excessive transmission-line losses when designed for high gain applications in mm-wave frequency. In printed high gain antennas, the feed network of the antenna is a significant problem when the size of the antenna aperture is large. There are various types of feed distribution networks. Corporate (parallel) and inline series feed networks are the two most common feeding technologies in printed antenna design. For passive antenna, the most popular feed network type is a corporate feed network, shown below in Figure 2.1. This technique integrates the RF feed network with the radiating elements on the same substrate. Another feed technique is the inline series shown in Figure 2.1 (b). In a series-fed, the input signal fed from one end of the feed network is coupled serially to the antenna elements. Considering the structures of the feed networks in high gain array antennas, printed array antennas have shown several electrical disadvantages. They suffer significantly from high dielectric/ohmic losses and surface wave leakage [25]. Specially, the large number of the long microstrip lines in the corporate feed network, in

the presence of discontinuities, bends, and steps, creates a huge amount of losses [26]. These losses are very important especially when increasing the operating frequency.

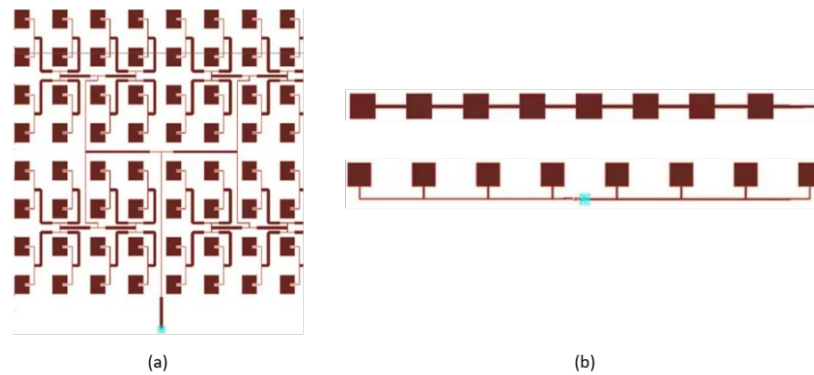


Figure 2.1 (a). Corporate Feed Network. (b). Inline series Feed Network

In mmWave applications, we need to come up with some solutions to reduce these losses. Minimizing losses of the microstrip feed network results in high efficiency planar antenna arrays. As a solution:

- Thin substrates can be used to decrease the dielectric loss in the feeding network of the array [27]-[28]. However, in order to achieve a 50 line impedance, a narrower strip must be utilized on a thin substrate, which increases conductive losses. Due to the higher resistance, narrower strip lines have higher conductive losses [29].
- Another technique to minimize feed network loss is to use a multi-layer feed network. Manipulating the feed network length per wavelength as short as possible minimizes conductor loss [30]. By using a multi-layer feed network design, the feed length per wavelength can be minimized considerably. In recent years, planar array antenna based on thin layers of low temperature co-fired ceramic (LTCC) technology have been widely introduced in many works at

mmWave applications [31]–[36] This is multilayered fabrication technology composed of very thin ceramic/silicon substrates. It features the flexibility to integrate the feeding structure and radiators of the antennas in a multilayered substrate using the perpendicular interconnection.

- Another alternative to achieve a high efficiency planar array antenna is to use a waveguide feed network. Hollow waveguide feeding structures have been known for many years for their high efficiency and high power applications [37]. They have lower losses with respect to traditional planar technologies. In this case, one of the solutions to increase radiation efficiency of planar array antenna is to incorporate a low loss waveguide feed network with dielectric based radiating elements. However, this results in significant increase in the antenna weight and dimensions. The non-planar structure of hollow waveguides makes it difficult to use them in integration with passive and active components.
- Regarding the non-planar structure of the hollow waveguide feeding network, the substrate integrated waveguide (SIW) or post-wall waveguides is introduced in [38] as an attractive technology with the advantages of both planar transmission lines and hollow waveguides (see Figure 2.2). The structure of SIW is similar to a rectangular waveguide structure filled with dielectric, where two rows of metalized via holes replace the narrow walls of the waveguide. The upper and lower metal plates and via holes form a current loop in the cross-section, similar to a metal waveguide. All these via holes should be placed closely to avoid possible leakage. SIWs have a planar profile which makes them interesting for integration with active components [39]–[40]. However, due to

the presence of dielectric, SIW faces the same problem as microstrip transmission lines and has shown higher loss than hollow waveguides. Moreover, radiation losses and leakage can occur in the walls, because the via holes do not provide a perfect shielding [38]-[41]. The losses can be partly reduced by using low loss dielectrics, but these materials are expensive, and also quite soft. Therefore, it becomes difficult to machine and make via holes through those types of planar structures. Leakage and surface waves may become a major problem in microstrip array antennas, especially in a big distribution network. Considering all the aforementioned techniques and technologies in improving the radiation property of the planar array antenna, Table 2.1 summaries some of the design of planar array antennas reported at mmWave band in terms of operation frequency, size, impedance, maximum gain, and antenna efficiency.

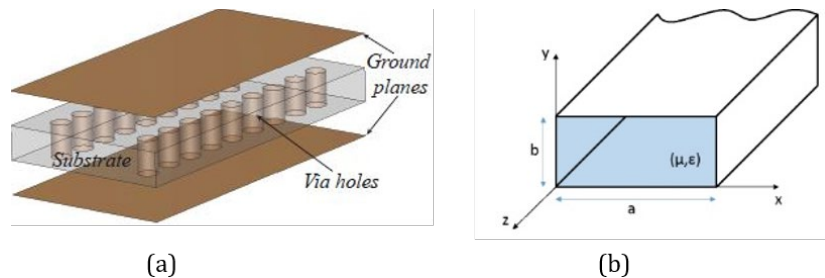


Figure 2.2 (a). Substrate Integrated Waveguide, (b). Rectangular hollow waveguide structure

Taking into account the results of the antennas in Table 2.1, the planar array antennas with different technologies are not suitable for high gain applications at mmWave band. Although they have a planar profile, their efficiency drops significantly at high frequencies. Achieving high gain and high efficiency properties is one of the key challenges with substrate-based antennas in mmWave communications. In order to

increase the efficiency of the array antenna and achieve higher gain, in the following section we are going to introduce and explain another category of high gain array antenna.

2.3 Slotted waveguide array antenna

Slotted waveguide array antennas have been known for many years for high efficiency and high power applications [1]. Slotted waveguide antennas are free from feeding loss and can be applied for sub-arrays in high-gain antennas. Waveguide antennas more especially have the advantage of both low feeding loss and compact size in mmWave band even though the size of the aperture is large. However, the manufacturing cost of waveguide antennas is generally very high because they usually consist of metal blocks with complicated three-dimensional structures. The most common geometry of slotted

Table 2.1. Planar array antenna at mmWave band.

Ref	Antenna Type	Frequency Band [GHz]	Number of Elements	Max Gain [dBi]	Antenna Efficiency
[40]	Mirostrip	58-67	64×64		
[42]	SIW	54-68	4×4	39	15%-20%
[39]	L-probe patch-Stripline	53-71	4×4	18	35%-45%
[43]	Cavity-backed dipole-SIW	56.1-70.6	8×8	17.5	54%
[44]	Loop loaded dipole	57-64	50 elements	26.7	70%
[45]	(PCB)	56.7-63		25	63.7%
[33]	Yagi(PCB)	54.86–	4×4	18	53%
[46]	LTCC	65.12	8×8	23	44.4%
[32]	Cavity-backed patch	57.5–67	8×8	30.1	49.5%
[47]	LTCC	136.7–	8×8	21.8	38.3%
	SIW-LTCC	146.5	8×8	21.3	35%
		129.2–146			

waveguide antenna is shown in Figure 2.3. The basic principle of the slot antenna is based on disturbing the surface current on the waveguide walls by implementing slots in longitudinal/transversal directions (Figure 2.4). In slotted waveguide array antennas, for higher gain and larger numbers of the radiating slots, hollow waveguide feeding distribution networks have been applied to feed the radiating slots of the array. Hollow waveguide distribution networks have low loss and high efficiency capabilities, which makes them suitable for the applications that require higher gain applications [48]-[49]. They do not suffer from dielectric loss in comparison with planar array antenna. However, the tiny gaps between the antenna blocks in array configurations can cause leakage and radiation losses (see Figure 2.5). Actually, these gaps can disturb the surface current on the walls and consequently change the antenna efficiency and disturb the overall performance of the antenna. Therefore, the fabrication of a complex waveguide structure is a challenging task, especially at mmWave frequencies. The key challenge is to achieve good electrical contact between the building blocks. This increases fabrication cost and manufacturing complexity and requires precise assembly fabrication techniques. This will normally not

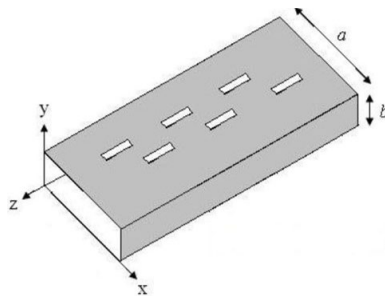


Figure 2.3 Geometry of the most common slotted waveguide antenna [1].

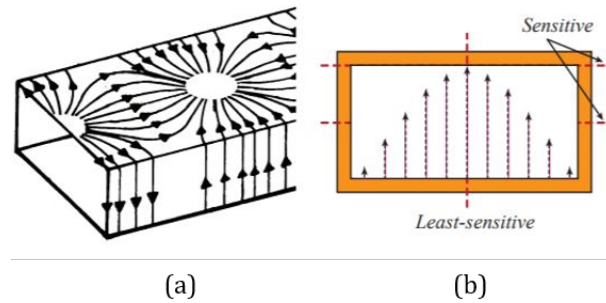


Figure 2.4 (a) Surface Currents distribution for TE_{10} mode in rectangular waveguide walls [1]. (b) Sensitive and least-sensitive places for joining walls. [3]

be possible to feed each radiating element in parallel (full corporate-feed) because of the space limitations associated with keeping the element spacing smaller than one wavelength (λ_0) to avoid grating lobe [50]. Therefore, Multi-layer corporate distribution networks have been implemented to feed radiating elements. In this case, radiating elements are fed in parallel plates by a corporate-feed network, formed by waveguide power dividers. However, it is very difficult to achieve good electrical contact between the vertical walls and the upper layer in a distribution network [51], [52]. To overcome the problem of leakage due to the assembly in the broad-wall slotted waveguide antenna, a narrow-wall slotted waveguide can be used (Figure 2.5). This antenna can be manufactured without disturbing and cutting the surface current on the waveguide walls. Flatness of the metal layers is another key factor to assure good electrical contact between plates. A high quality flatness especially in a large surface, is not an easy task. Good alignment of the two blocks must be achieved in order to remove the gaps between the two split. This needs lots of screws to assure good contact, and is not always successful. These strict mechanical requirements lead to complex and high-precision manufacturing techniques and novel ideas. For example, the antenna in [2] (see Figure 2.6) is composed of a multi-layer corporate-fed feeding network consisting of many thin copper plates. In order to achieve good electrical contact between all the plates, the authors used the diffusion bonding

fabrication technique which is very expensive to have mass product this antenna. Diffusion bonding is a solid-state welding technique capable of joining metals. Diffusion bonding is typically implemented by applying both high pressure and high temperature to the materials to be welded. Considering the traditional planar technologies and challenges in the manufacturing of slot array antennas at high frequencies, there exists a big gap between the planar transmission lines such as microstrips, SIW and non-planar hollow waveguides in terms of performance such as loss and fabrication flexibility. Therefore, one of the main current research challenges is to find a transmission line solutions with flexible and low-cost fabrication and low-loss at the same time. This is possible by using the new metamaterial-based gap waveguide technology [3].

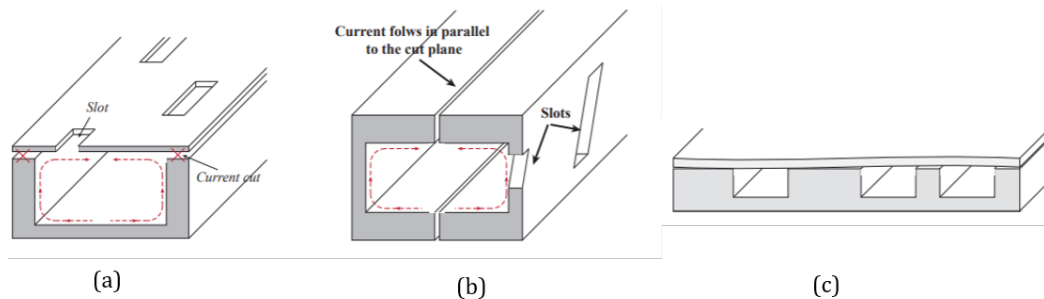


Figure 2.5 Surface current distortion in slotted waveguide antennas. (a) Current cut in broad-wall slot antenna. (b) Narrow-wall slot antenna without the problem of disturbing current. (c). Flatness problem

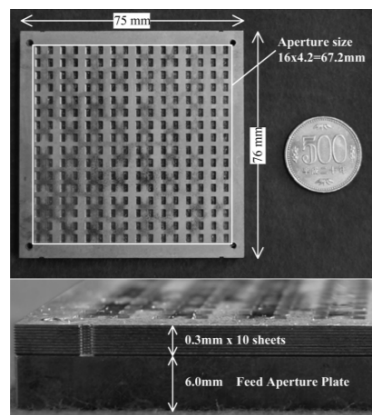


Figure 2.6 Antenna configuration in [2]

2.4 Gap waveguide array antenna

In 2009, gap waveguide (GWG) technology was introduced by Kildal et al. as an alternative to hollow waveguides and microstrip lines at high frequency applications; this technology demonstrates a performance comparable to that of a rectangular waveguide transmission line if the dimensions are properly chosen [53]-[54].

The basic principle operation of gap waveguides is the cut-off of a PEC/PMC parallel plate waveguide configuration, to control the propagation of waves in desired directions between the two plates. This idea is shown in Figure 2.7. For the air gap between the two plates smaller than $\lambda/4$ no wave can propagate between the plates, due to the boundary conditions at the plates. By introducing a metal strip in the PMC surface, a TEM mode will be able to propagate along the strip.

In practice, the PMC condition is artificially realized by using Artificial Magnetic Conductors (AMCs) to emulate the high impedance boundary condition of a PMC surface [55]. In gap waveguides, the AMC is realized in the form of periodic textured structures (e.g. metal pins or mushroom structures) in combination with a smooth metal plate, with an air gap between them. When the air gap is smaller than a quarter wavelength there is a cut-off of all mode propagation within the gap due to the high surface impedance created by periodic texture [56]. This can be used to control the propagation direction without leaking away in other directions. Based on the guiding-line, propagation characteristics and the band gap structure, the gap waveguide can be made in different versions. Ridge gap waveguide [57] groove gap waveguide [58], microstrip gap waveguide [59], and inverted microstrip-ridge gap waveguide [60] are the four different varieties of gap waveguide technology. Figure 2.8 shows four different gap waveguide configurations and their

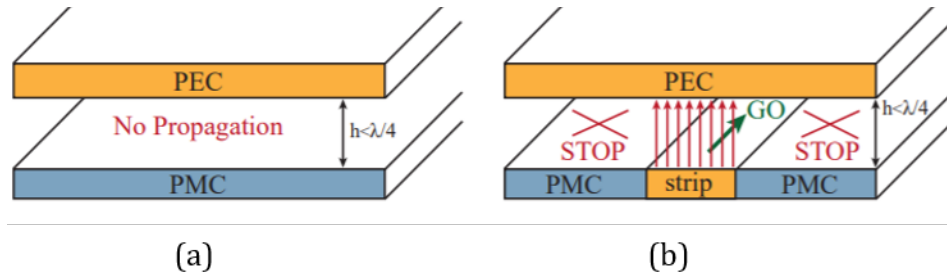


Figure 2.7 Basic principle operation of gap waveguide. (a) PEC – PMC Parallel plate electromagnetic wave Cut off (b) TEM local waves propagation [3].

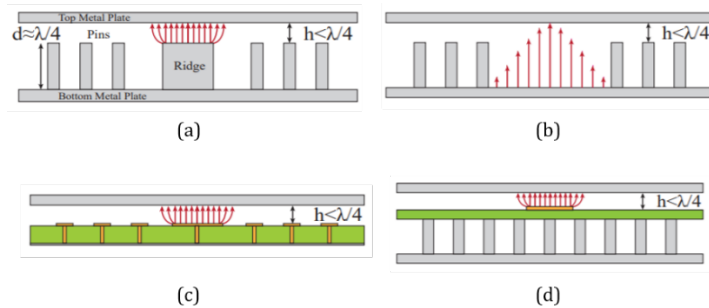


Figure 2.8 Different gap waveguide geometries and desired modes of propagation. (a) Ridge gap waveguide. (b) Groove gap waveguide. (c) Microstrip gap waveguide. (d) Inverted-microstrip gap waveguide [4].

fundamental modes. Gap waveguides have interesting characteristics such as low loss, flexible planar manufacturing, and cost-effectiveness, especially at millimeter-wave frequencies. [4]. The advantage compared to microstrip transmission lines and SIW is that the gap waveguide has a planar profile with low loss, since the wave propagates in the air. This new technology has almost no dielectric loss (especially in ridge and groove gap waveguide configurations), and it is mechanically more flexible to fabricate and assemble than hollow waveguide structures. Electrical contact between the building blocks is not needed in these guiding structures. This offers new opportunities for making cost-effective antennas and in particular corporate-feed networks [61][62][63]. Therefore, gap waveguides can be mass-produced by the usage of some low cost fabrication techniques such as injection molding, die pressing, plastic hot embossing, or die-sink EDM [64].

GWGs antenna are either full metal constructions or metal-PCB hybrid structures. They have a planar profile, and can be used as low loss distribution networks for an antenna array. As an example, Figure 2.9 shows a prototype of a metal-PCB hybrid structure in which patch array antenna is fed with a ridge GWG feed network. The antenna efficiency is more than 75 % over the bandwidth of 15.5% (57.5–67.2 GHz), which is more than conventional patch array antennas. In recent years, GWG array antenna have received extensive interest for applications at mmWave band. Several low-profile array antennas with high efficiency and wide impedance bandwidth based on gap waveguide technology have demonstrated the advantages of this new guiding structure with flexible mechanical assembly and low loss. Figure 2.10 depicts some of the prototypes of high gain array antennas with GWGs constructions.

The main challenge of gap waveguide components is the realization of the textured structure (pin surface) with a cost-effective method. Due to the relatively complex pattern and physical dimensions of the textured structure, the fabrication of the product presents a challenging task, especially at mmWave frequencies.

In this section, we reviewed the three most common array technologies for high gain applications at mmWave band. Some of the issues of the traditional planar technologies, challenges in manufacturing of slot array antennas, and new structures of gap waveguide array antenna at high frequency applications have been reviewed. We presented some of the key characteristics of these antennas. As discussed above, there exists a big gap between the planar transmission lines and the non-planar hollow waveguides in terms of performance such as loss and fabrication flexibility. Moreover, the new guiding

technology, GWG array antenna, exhibits promising features such as planar geometry, and low losses in comparison to waveguide slot array antenna.

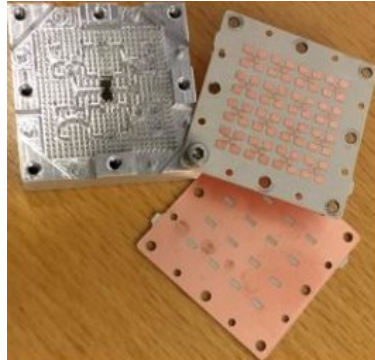


Figure 2.9 A ridge waveguide-fed Patch Antenna Array[5].

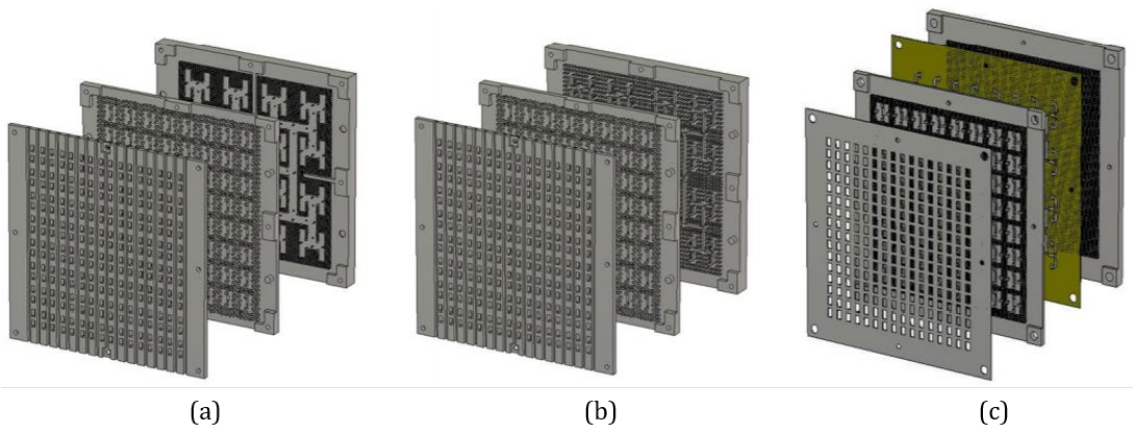


Figure 2.10 The schematics of the three 16×16 slot array designed in gap waveguide technology. (a). Groove gap waveguide slot array. (b). Ridge gap waveguide slot array. (c). Inverted microstrip gap waveguide slot array. [65]

CHAPTER THREE: 60 GHz WAVEGUIDE-FED ARRAY ANTENNA BY MULTI- STEPPED SLOT APERTURE

3.1 Introduction

This section presents a center feed high gain and high efficiency 4×4 -element slot array antenna in the 60 GHz band. The feeding network of the antenna is designed only with a single-layered square quad-ridge cavity structure, which is excited through a rectangular slot of the same size as a standard WR-15 rectangular waveguide. The proposed antenna avoids the utilization of any conventional power dividers in the feeding network so that the complexity of the design and fabrication is reduced. To adjust the problem of the narrow bandwidth of the proposed cavity for the array, a stepped design of rectangular slots is employed for each radiating slot of the subarray. Furthermore, the overall radiating aperture of the antenna is equipped with a dielectric layer, which decreases the mutual coupling among array elements. As a result, a broad bandwidth antenna with high efficiency and low sidelobes in both E- and H-planes is achieved over the 60GHz band. The antenna has been fabricated and tested. Measurement results show an operating bandwidth of around 11.6% from 57.7–64.7 GHz. A gain of more than 23 dBi associated with the sidelobes of less than -15.2 dB is achieved, and higher than 66% antenna efficiency over the frequency range from 58-64.4GHz.

3.2 Antenna Design and Configuration

The configuration of the proposed multilayer slot aperture array antenna is shown in Figure 3.1. The antenna is separated into three main layers, i.e., the radiating layer, the

feeding layer, and the dielectric layer. The radiating and feeding layers are connected together electrically and the dielectric layer is separated with a gap from the radiating layer. The exploded view of the layers forming the antenna are shown in Figure 3.1. The feeding distribution network is implemented with a single quad-ridge cavity feeding technique connected to a standard WR-15 rectangular waveguide. The input power from the waveguide port is divided into four feeding slots via the quad-ridge cavity structure. Each feeding slot couples the power upward into a 2×2 coupling cavity. Then, the coupling slots feed the radiating layer. As shown in Figure 3.1, the radiating layer is composed of four separate layers. Each layer consists of 4×4 rectangular radiating slots. Furthermore, the radiating aperture of the antenna is loaded by a dielectric layer to improve radiation characteristics of the antenna. In the following, we demonstrate and discuss the design of the proposed antenna for the proposed subarray and complete array.

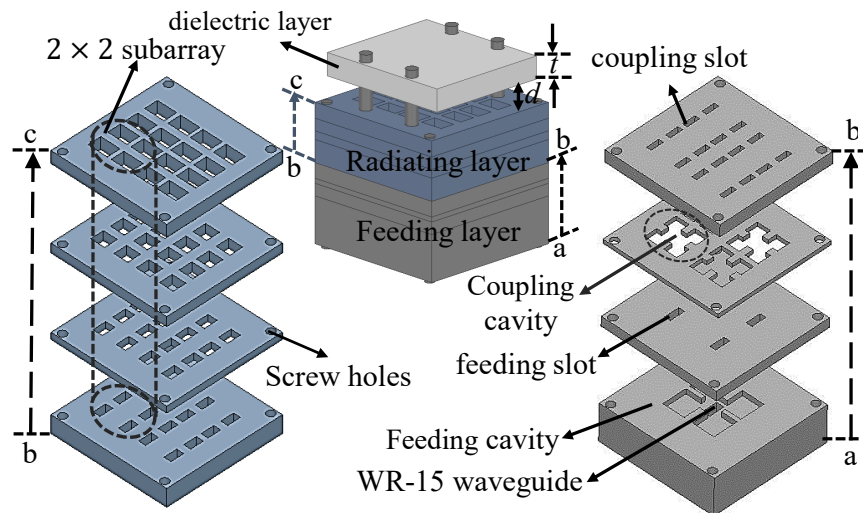


Figure 3.1. Configuration of the proposed cavity-backed 4×4 slot array antenna.

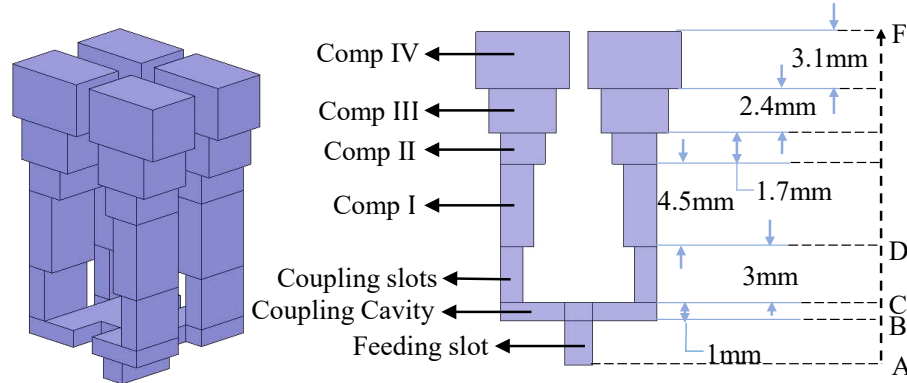


Figure 3.2. 2×2 -element slot aperture array

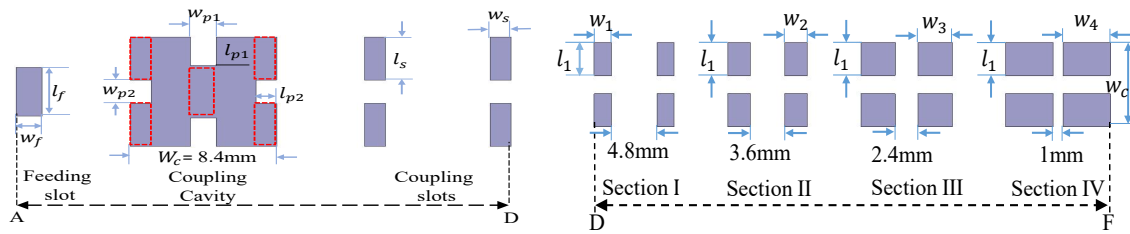


Figure 3.3. Exploded view of the proposed cavity-backed 2×2 subarray

3.3 Basic Subarray design

The 2×2 -element slot aperture array is shown in Figure 3.2. It comprises of seven main components: Comp I, Comp II, Comp III, Comp IV, Coupling slots, Cavity, and the Feeding slot (see Figure 3.2). The Cavity has a quad-ridge configuration based on a conventional cavity feeding structure [66]. In general, these structures have efficient and compact topologies in which a single feeding aperture at the bottom surface of the cavity distributes power into four radiating slots. Considering the structure of the cavity, as shown in Figure 3.3, four coupling slots are positioned symmetrically in every cavity free-space in x and y directions. The red dash-lines on the corners of each cavity show the exact positions of the slots with respect to the center of the cavity. The coupling slots act as an interface layer between the cavity and radiating layer.

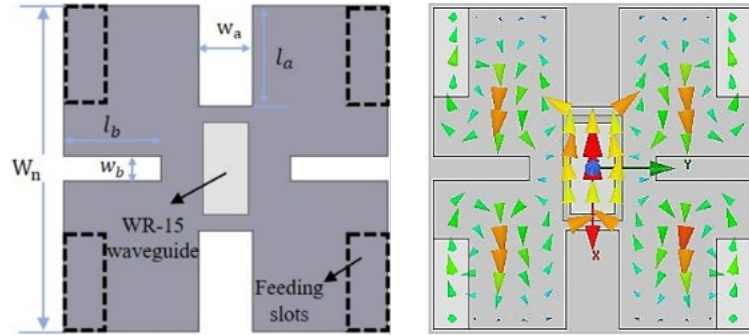


Figure 3.4. Feeding cavity of the array ($w_a \times l_a = 2.2 \text{ mm} \times 4 \text{ mm}$, $w_b \times l_b = 1 \text{ mm} \times 4 \text{ mm}$, $w_n = 13.3 \text{ mm}$). (b) Magnetic field distribution in the cavity.

3.4 Feeding Network

To feed a larger 4×4 -element array, we need to design a wideband feeding distribution network. In order to decrease the complexity of the feeding network, instead of designing an arrangement of conventional T-junction power dividers or an H-junction power distribution we propose to use a single quad-ridge backed-cavity to assemble the feeding network of the array. As shown in Figure 3.4, the Feeding Cavity is connected to the input transmitter through a transverse rectangular slot etched on the bottom surface of the cavity. In this case, this slot has the same size as a standard WR-15 waveguide. The input signal propagating in the WR-15 waveguide is divided into four paths through the four feeding slots positioned at each corner of the cavity. As shown in Figure 3.5 symmetrical field distribution can be seen with respect to the center of the cavity in the y direction. Note that the distance between the feeding slots should be large enough to accommodate four subarrays next to each other, while being compact enough to ensure proper spacing for the radiating slots to avoid high grating lobes. This method is promising for high frequency antenna designs since their structures are too simple to be realized by conventional fabrication techniques. To achieve desirable impedance matching between the feeding slots and the radiating layer, structural parameters of the feeding cavity such as

the height as well as the width and the length of the ridges ($w_a \times l_a, w_b \times l_b$) are optimized to control the bandwidth characteristics of the antenna. The proposed antenna is analyzed and optimized using the commercial High Frequency Simulator (HFSS). To demonstrate the effects of these parameters, we analyzed the reflection coefficient of the antenna array with different values of l_b and w_a . The results are shown in Figure 3.5. It can be seen in Figure 3.5 (a) that by decreasing and increasing l_b , the impedance matching of the antenna is degraded in the desired frequency band. In Figure 3.5 (b), when the w_a varies from 1.6 to 2.5 mm, the impedance matching of the antenna for lower resonances change significantly.

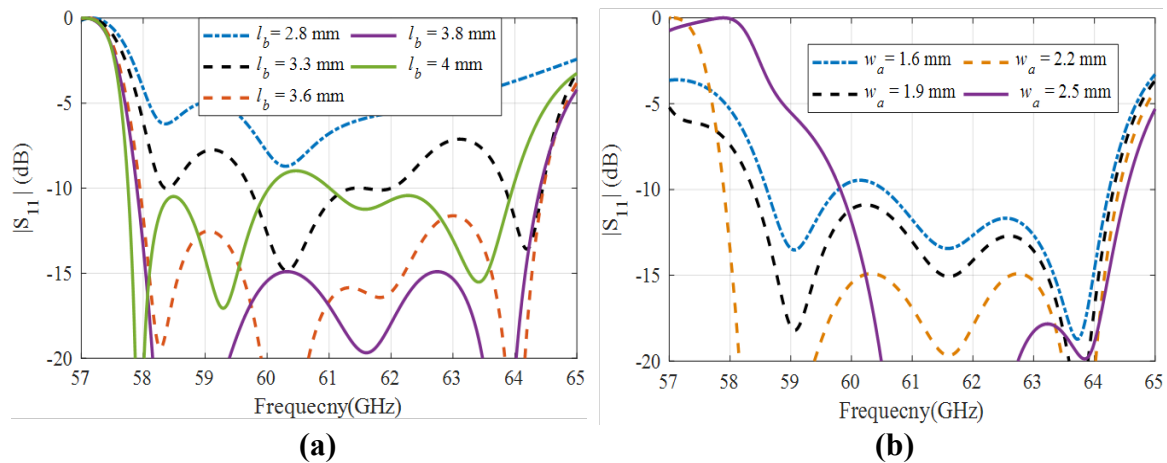


Figure 3.5. (a) Simulated reflection coefficient for different values of l_b with fixed value of $w_b = 1$ mm. (b). Simulated reflection coefficient for different values of w_a with fixed value of $w_b = 1$ mm, $l_b = 3.8$ mm, and $l_a = 4$ mm.

3.5 Dielectric Loading

To improve the radiation characteristics of the antenna, we implement a dielectric layer, with a thickness of t , in a certain distance of d over the aperture of the antenna. The dielectric material used in this work is a low-cost and high efficiency polymer material (Rexolite with relative permittivity $\epsilon_r = 2.54$ and loss tangent $\tan\delta = 0.00066$ at 10 GHz).

In this part, our purpose is to explain that how employing the dielectric layer in front of the radiating aperture of the antenna improves the sidelobe performance of the antenna. For more clarification of the antenna performance, it is important to mention that in the proposed design; first, without using the dielectric layer, the antenna is designed and its performance is optimized to achieve the best characteristics in terms of broad bandwidth, maximum gain and low sidelobe levels. Taking into account these features, we accomplished multiple optimization for geometrical parameters of the antenna. Then, considering the sidelobe results of the antenna over the bandwidth from 58 GHz to 64 GHz, in order to decrease the sidelobes in both radiation planes to less than -15 dB, we covered the radiating aperture of the antenna with an external dielectric layer. Without the dielectric layer, the sidelobes vary from -11.7 to -14.9 dB in the E-plane and -12.16 to -13.9 dB in the H-plane. It should be noted that the antenna, without the use of the dielectric layer, still has good performance in terms of sidelobe results. These results are comparable with the previous array antennas reported for 60 GHz applications[67][68][69][70]. For example, in [70], the authors rotated the radiating slots of the antenna by 10 degree to improve the sidelobe levels in the array. Authors in [69] used corrugated plates in associated with the radiating slots to decrease the grating lobe effect in higher frequencies.

In this approach, the parameters of the dielectric plate, d and t , are optimized to minimize the mutual coupling affects for best performance. Moreover, these parameters provide additional degrees of freedom to minimize the reflection coefficient of the antenna. Using a dielectric layer on the top of the radiating aperture of the antenna changes the field distribution across the aperture of the antenna and provides more uniform field distribution. To obtain low sidelobes patterns, it is necessary to change the field distribution across the

aperture of antenna. Therefore, using the idea in paper [a] we implemented a dielectric layer to achieve the desired field distribution. However, the proper design of geometrical parameters of the dielectric layer, e.g., d and t has significant effect on antenna performance. Actually, the dielectric layer as an external element on the top of the antenna

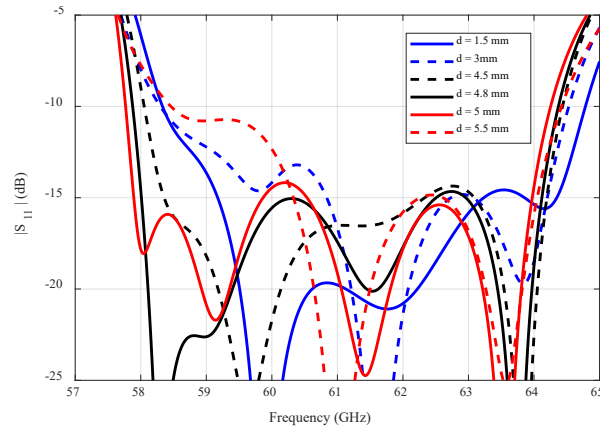


Figure 3.6. Reflection coefficient of the antenna for different values of the d parameter (dielectric plate separation from the aperture)

can positively/negatively affect the antenna performance in terms of impedance matching and radiation pattern. The signal reflections at the air-dielectric interface alter the

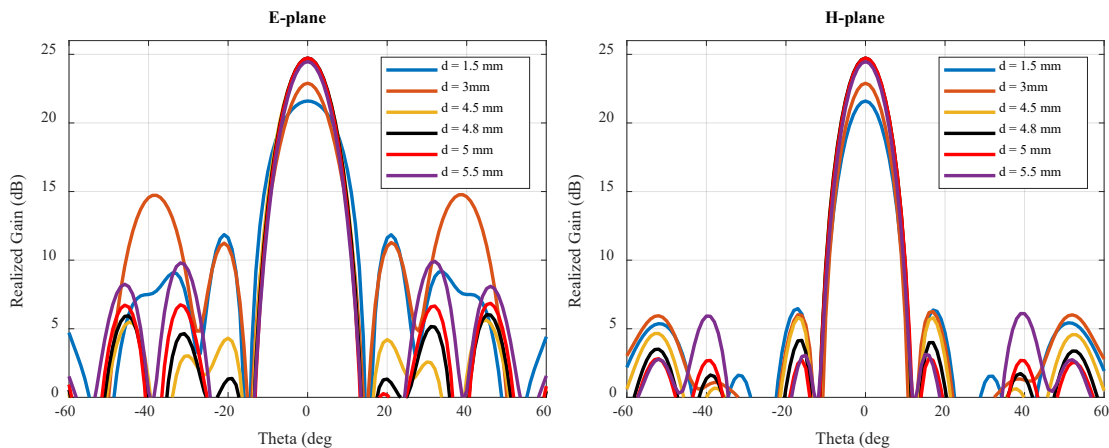


Figure 3.7. Radiation pattern of the antenna for different values of the d parameter (dielectric plate separation from the aperture) in E- and H- planes.

impedance matching of the antenna and can adversely deteriorate the radiation characteristics of the antenna. Therefore, it is very important to choose proper values for its parameters. Using dielectric layer should not degrade antenna performance in terms of bandwidth and radiation patterns, because the antenna still has acceptable results without the dielectric layer at 60 GHz band. In this case, some optimizations have been conducted in HFSS to determine the effect of a dielectric layer on the impedance matching and the radiation pattern of the antenna. We have presented a parametric study of the layer separation (d) from the antenna aperture to show its effect on antenna performance. Figure 3.6, shows a parametric study of the layer separation (d) from the antenna aperture. As can be seen the antenna bandwidth has been affected by this parameter and the reflection coefficient characteristics of the antenna is changed at lower frequencies. Moreover, for further clarification, the E- and H-planes gain radiation pattern at 60 GHz for different values of d is presented in Figure 3.7. It can be observed that the antenna sidelobes performance has reached an acceptable level by properly choosing the placement of the

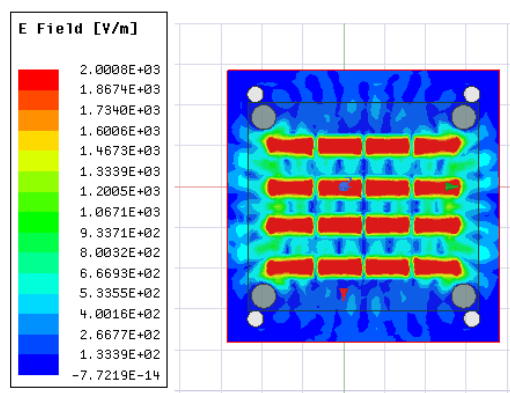
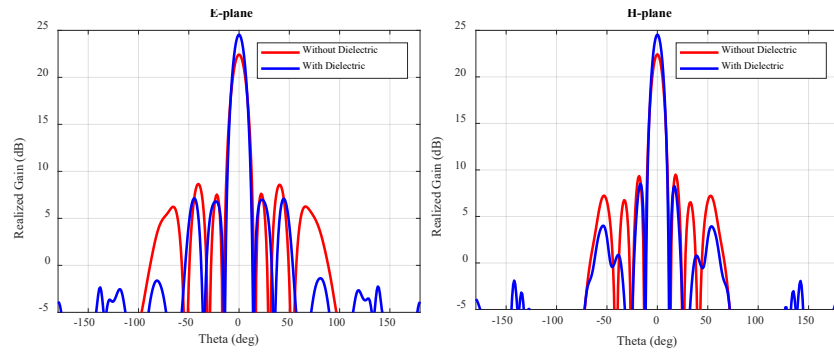


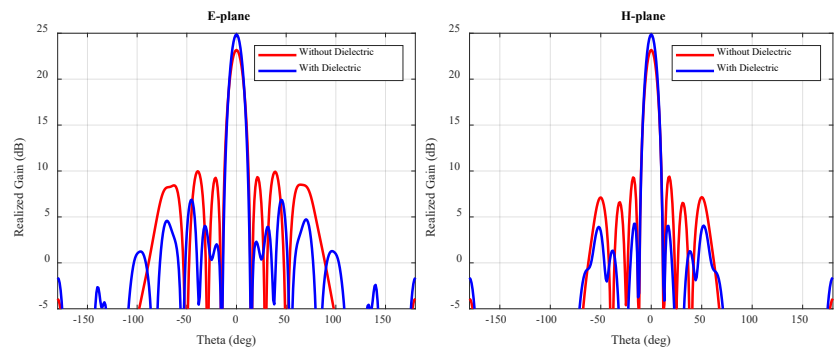
Figure 3.8. Electrical field distribution over the aperture of the antenna

dielectric layer. The results show that the sidelobe levels at 60 GHz is reduced to -18.79 dB and -20.58 dB in E-plane and H-plane respectively. Moreover, due to the uniform

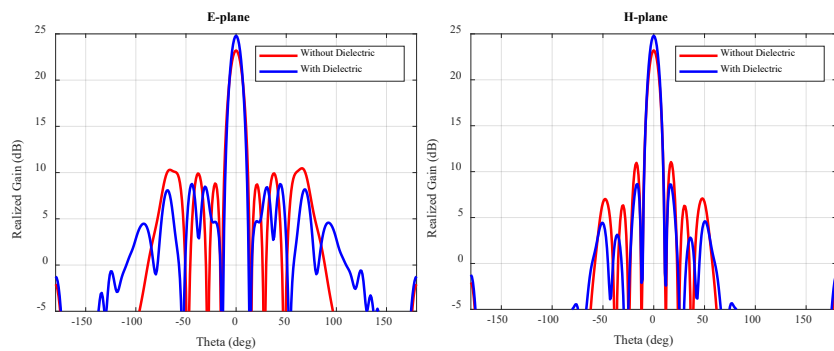
electrical field distribution over the aperture of the antenna and the ability of the dielectric layer in focusing the electromagnetic waves we have a gain enhancement of about 2 dB across the bandwidth at operating frequency. Figure 3.8 shows field distribution on the aperture of the antenna with a dielectric layer. Furthermore, considering the results of the realized gain of the antenna over the bandwidth, it is shown in Figure 3.9 that the gain of the antenna is improved by approximately 2 dB over the entire bandwidth. As a result, it should be noted that the idea of loading the aperture of the slot array antenna with a proper dielectric layer can be more beneficial in larger scale arrays, because it leads to a decrease in the number of radiating elements and reduces the complexity of the feed network for a larger array. The effects of the dielectric layer were investigated in HFSS and the optimum values of d and t , which yields to the best antenna efficiency in the broad bandwidth is determined as $d = 0.9\lambda_0$ and $t = 0.98\lambda_0$ (λ_0 is free-space wavelength at the 60 GHz). The array is extended for a larger 8×8 array in Figure 3.11. Considering the simulated gain and radiation



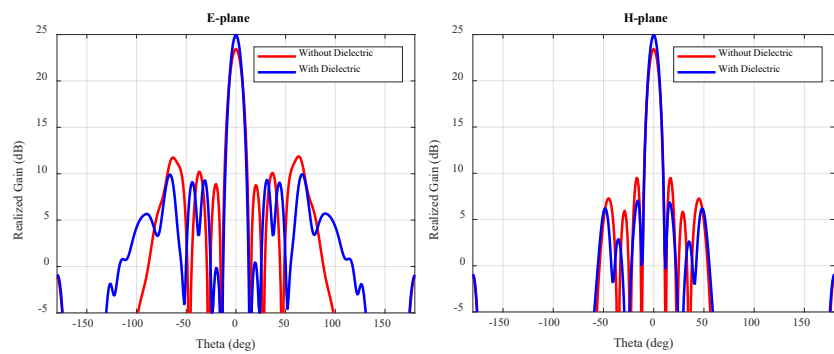
(a)



(b)



(c)



(d)

Figure 3.9. Simulated radiation pattern in E- and H-planes at (a) 58, (b) 60, (c) 62, (d) 64 GHz

pattern results in Figure 3.10 , Figure 3.12 and Figure 3.13 in comparison to the previous 8×8 array antennas, our design for a larger scale array depicts more gain over the frequency band from 58 GHz to 65 GHz. Actually, loading the stepped-aperture of the proposed antenna with a dielectric layer as an external element improves the radiation characteristics of the antenna, without increasing the number of radiating elements. This is more beneficial in fabrication at high frequency application.

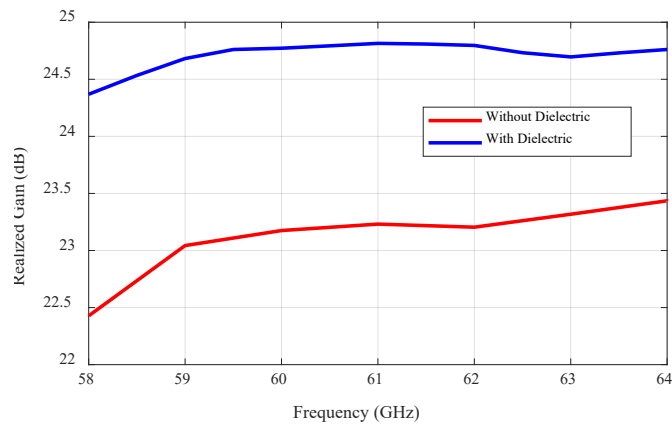


Figure. 3.10. Simulated realized gain of proposed antenna with and without dielectric layer

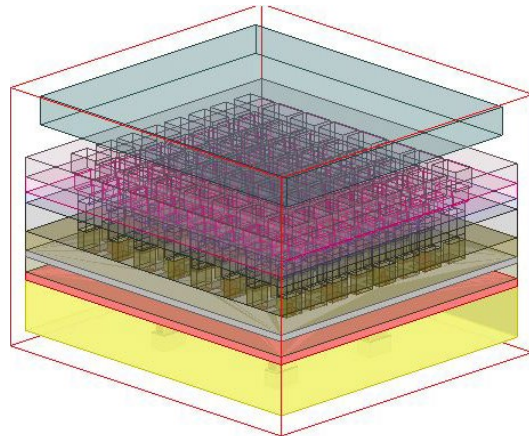


Figure 3.11. Configuration of the 8×8 -element array antenna

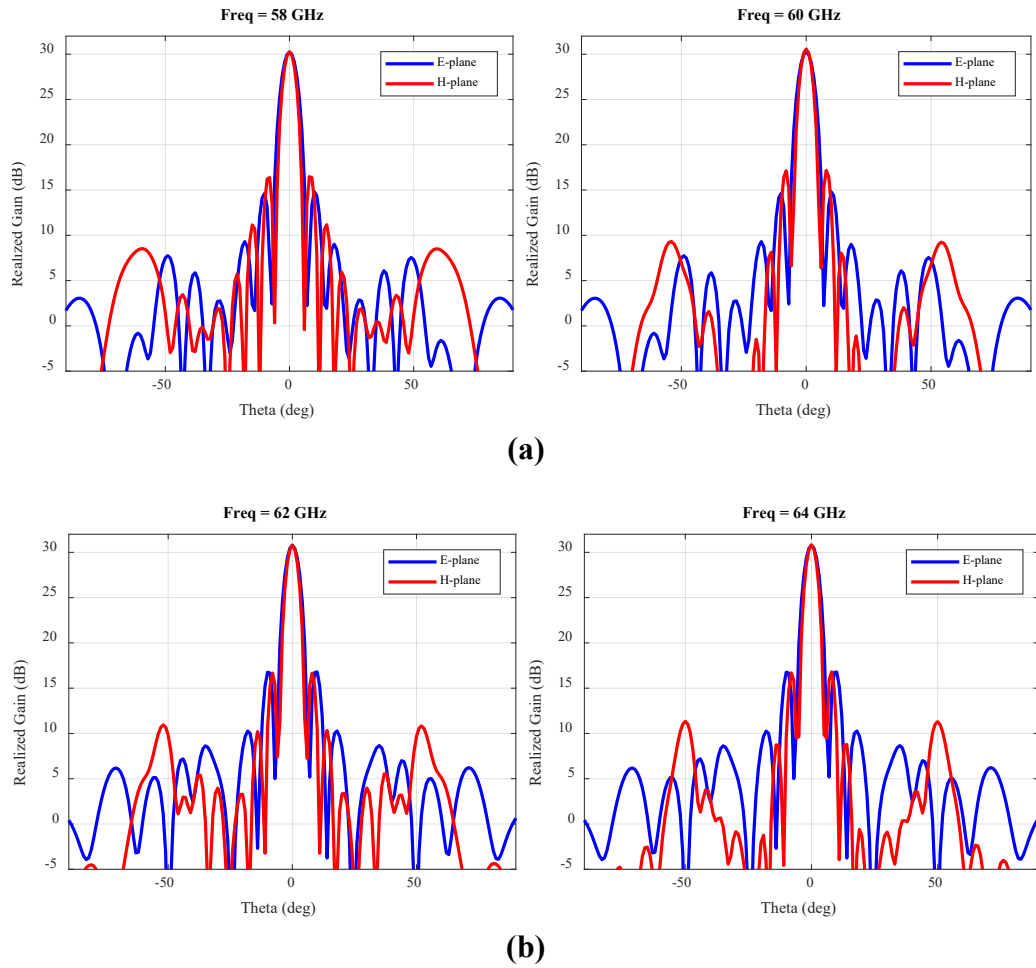


Figure 3.12. Simulated radiation pattern in E- and H-planes at (a) 58, 60 GHz, (b) 62, 64 GHz

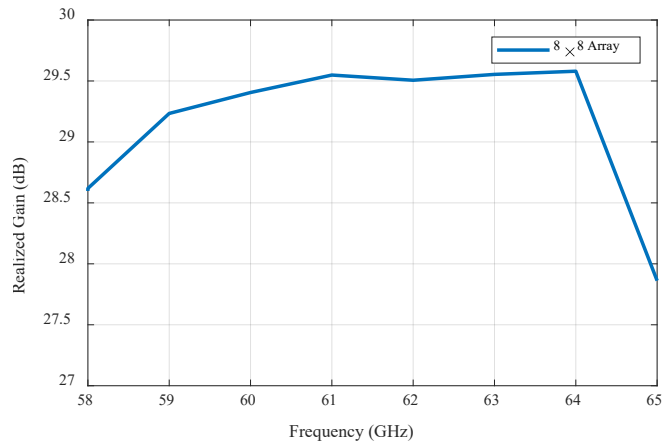


Figure 3.13. Simulated realized gain performance of the 8×8 -element array antenna

Table 3.1 lists the optimized values of antenna parameters that were obtained through extensive simulations.

Table 3.1. Design Parameters For 4×4-Element Array

Parameter (mm)	
$w_1 = 1.8, w_2 = 2.4, w_3 = 3.6, w_4 = 5, l_{=1}$	Width and length of the radiating slots
$w_s \times l_s = 3.3 \times 2$	Width and length of the coupling slots
$w_f \times l_f = 2.1 \times 3$	Width and length of the feeding slots
$w_{p1} \times l_{p1} = 1 \times 2, w_{p2} \times l_{p2} = 3 \times 2$	Width and length of the ridges in the coupling cavity
$w_a \times l_a = 2.2 \times 4, w_b \times l_b = 1 \times 3.8$	Width and length of the ridges in the feeding cavity

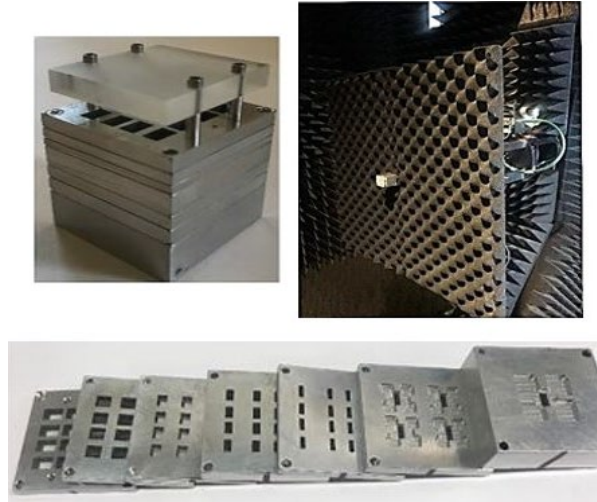


Figure 3.14. Prototype of the proposed array antenna.

3.6 Experimental Results

To verify the proposed design, a 4 × 4-element antenna array was fabricated by using a wire Electrical Discharge Machining (EDM) technique. To obtain the desired geometry of the multi-stepped radiating layer, using this manufacturing process, the antenna block is made in seven individual pieces. We should mention that in comparison

to Figure 3.4 in which we have eight layers, we put two layers of the feeding layer together during fabrication and reduced the numbers of layers to seven. Seven layers of Aluminum plates with specified thicknesses are machined on the wire-EDM with 0.25 mm brass wires. To consider the effect of the wire all the corners in our design are converted to round edges with a radius of 0.125 mm. The layers are aligned by two registered pins and assembled by four screws. The dielectric plate is separated with four standoffs from the antenna aperture. The array prototype is shown in Figure 3.14. The total size of this array is 30 mm × 30 mm × 36 mm. The overall height of the array is 27 mm. However, we have added an extra 9 mm to the thickness of the feeding cavity in the manufactured prototype for connecting the antenna to the standard WR-15 flange. Figure 3.15 exhibits the simulated and measured frequency characteristics of the manufactured antenna. The measured reflection coefficient is in a good agreement with the simulation results. The -10 dB reflection coefficient is achieved within the operating band from 57.7 GHz to 64.7 GHz.

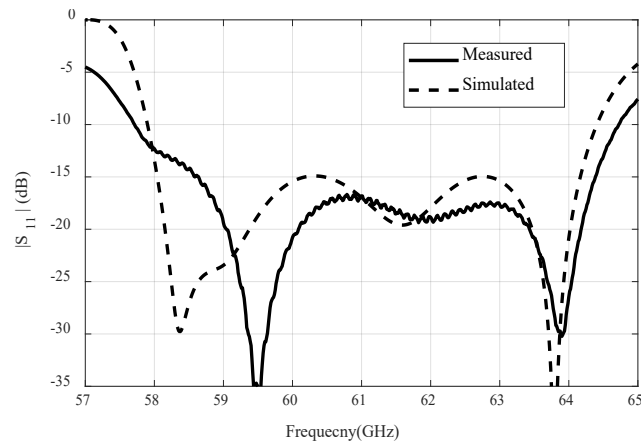
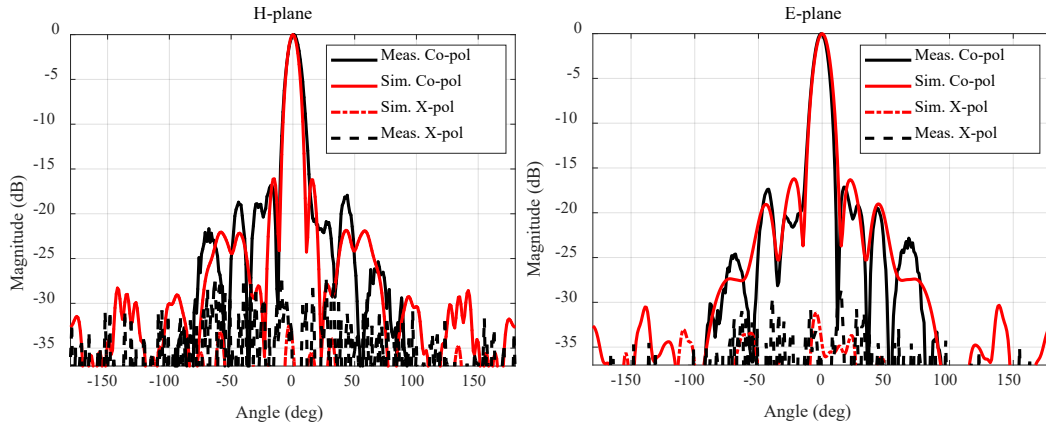
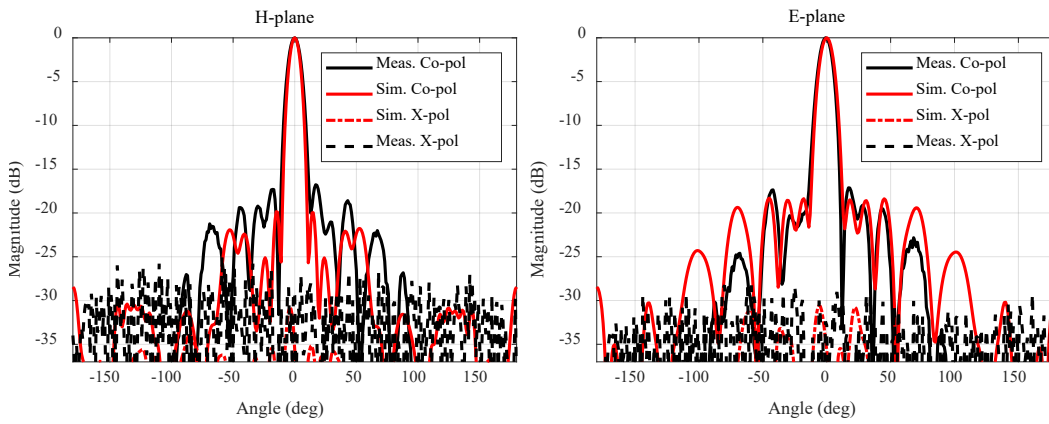


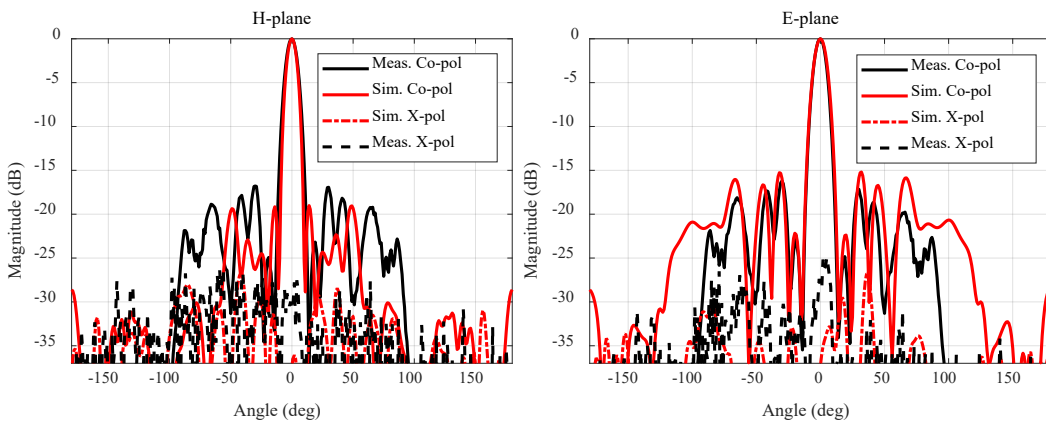
Figure 3.15. Comparison of simulated and measured input reflection coefficient of the fabricated prototype



(a)



(b)



(c)

Figure 3.16. Simulated and measured radiation patterns in E- and H-planes at (a) 58, (b) 61, and (c) 64 GHz.

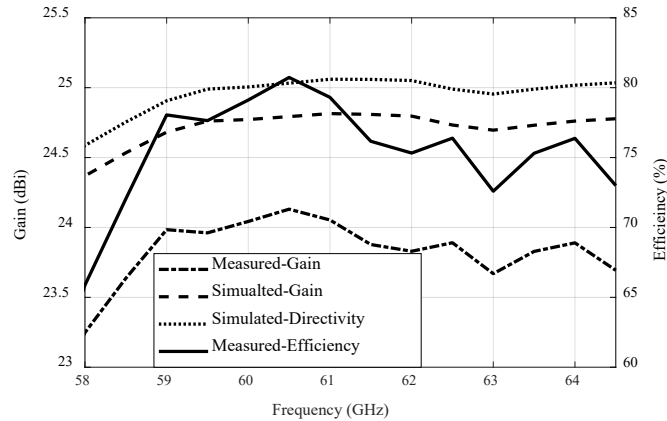


Figure 3.17. Frequency behavior of directivity, gain, and efficiency.

There is a slight difference between the measured and simulated values at frequencies between 58.4 to 59.5 GHz, which might be attributed to the fabrication process variation and the measurement set up. The antenna radiation characteristics are measured in an anechoic chamber at the University of Colorado Boulder, as shown in Figure 3.14. The measured and simulated results of the co-and cross-polarization components of the radiation patterns at 58, 61, and 64 GHz in E-and H-planes are illustrated in Figure 3.16. The results show good agreement between measured and simulated values over different frequencies. The measured E- and H-plane cross-polarization values are both less than -25 dB. All of the measured sidelobe levels over 58–64 GHz are better than -15.4dB. The half-power bandwidths of E- and H-planes vary from 11.8° to 11.1° , and 10.5° to 9.6° over the operating band, respectively. The gain of the antenna at broadside direction is illustrated in Figure 3.17. The measured gain of up to 24.13 dBi with a variation of less than 1 dB is achieved from 58 GHz to 64.4 GHz. Moreover, the measured gain of the antenna is slightly lower than the simulated one, which is mainly, can be caused by the tolerance of the fabrication process and possible variation in the dielectric constant *and* loss tangent of the dielectric material. It can be seen in Figure 3.17 the measured antenna efficiency is above 72% over the operation bandwidth from 58.5 to 64.5 GHz.

3.7 Assembly Consideration

Waveguide slot/ Gap waveguide array antennas in the literature such as in [9]- [8], require the use of multi-layer blocks which can consists of sometimes up to 7 Layers. Further, although the antennas designed based on the gap waveguide technology with periodic textured plates, e.g., [f, have a lower number of layer counts, similar to the works in [8]- [9], require high precision and expensive fabrication techniques when considering frequencies in mmWave band. Therefore, the slot/gap waveguide array antennas might have assembly difficulties. Therefore, it is important to reduce the complexity of each layer to decrease fabrication tolerances. For example, the manufacturing process for the metallic pins in [f] may be a challenging task. In this work the width of metallic pins is only 0.3 mm, which is difficult to vertically fabricate them. Moreover, manufacturing tolerances for the tilted pins can affect the reflection characteristics of the array. However, the proposed antenna has a very simple design in which the smallest dimension in the feed network of the array is $w_b = 1\text{mm}$. To showcase the robustness of our design, we analyzed our design under a 10% error in manufacturing process when considering the parameter w_b . As can be seen in Figure 3.18 the frequency response of the antenna does not change significantly. We also considered a 10% tolerance for the height of the layers. Figure 3.19 presents the simulation results of the changes. These results support our claim that the proposed design results in an antenna that can be manufactured by using less accurate and expensive manufacturing methods.

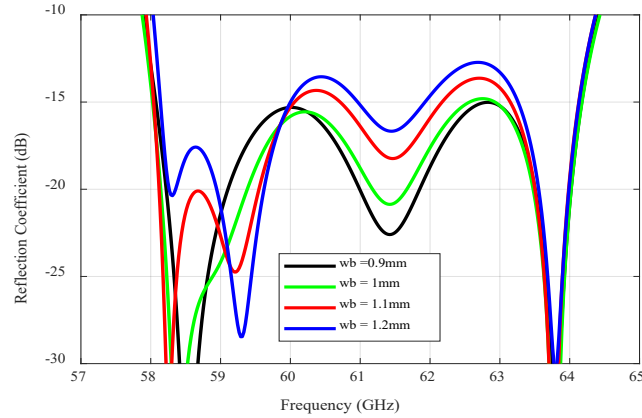


Figure 3.18. Frequency response of the antenna with parametric study of w_b parameter

Misalignment due to the assembly process of the layers is always critical and can degrade the impedance matching of the antenna. The proposed antenna is assembled by four screws in the four corners around the radiating aperture. This assembly method may cause

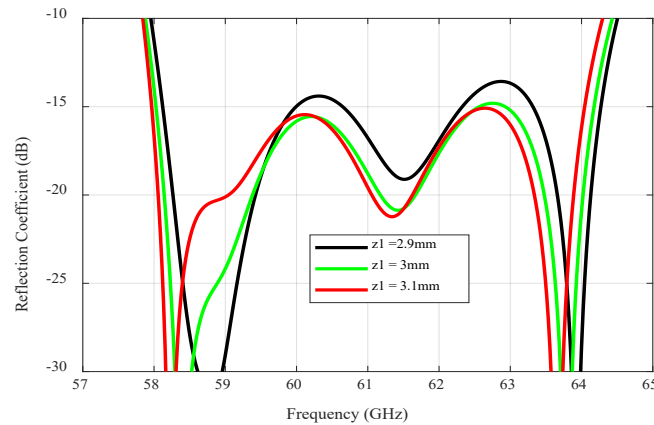


Figure 3.19. The effects of the height of layer composed of coupling slots

misalignment between the layers, which has been depicted in both the x- and y-directions in Figure 3.20. We have analyzed the results of this misalignment in Figure 3.21, where simulation results of the proposed array antenna with 25, 50, 75, and 150 μm misalignment in both the x- and y-directions are shown. All the results mentioned above show that our design is robust to manufacturing errors. The results show that the proposed design still

performs well when there are errors in the manufacturing process. Furthermore, in order to reduce the layers of the proposed antenna, it is possible to manufacture the radiating part of the antenna in just one block with Metal 3D printing methods. Finally, it is important to note that the planar array antennas in the literature such as [6], also suffer from assembly and manufacturing issues. For example, the antenna design in [6] is fabricated with 20 layers of thin metal plates, which need high precision fabrication techniques.

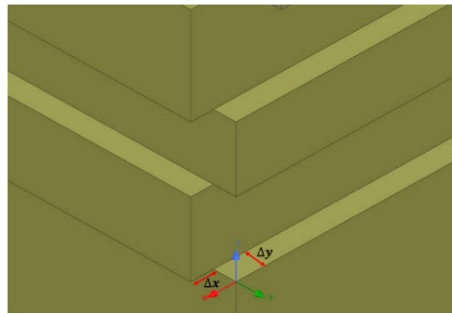


Figure 3.20. Illustration for analysis of misalignment of the proposed array antenna

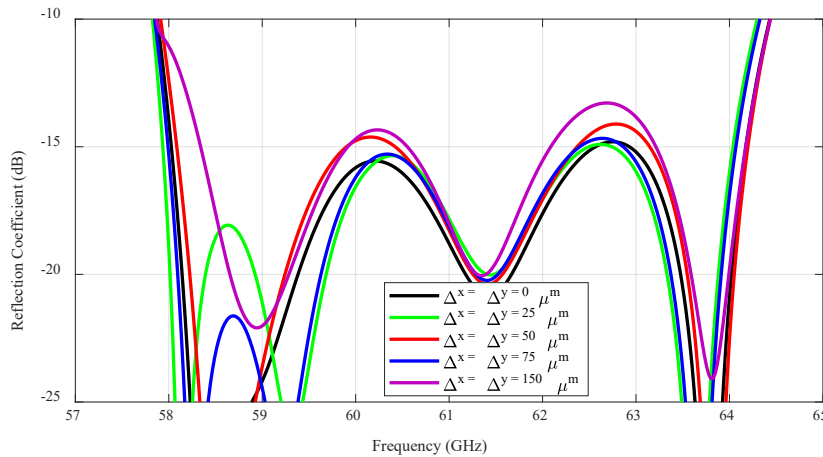


Figure 3.21. Simulated reflection coefficient characteristics of the structure considering misalignment.

3.8 Conclusion

In this work we propose a new and high gain 4×4 element slot array antenna for applications at 60 GHz. The proposed antenna demonstrates the merits of stable

performance, high efficiency, low cost, and flexible mechanical assembly. The multi-stepped radiating elements together with the single quad-ridge feeding cavity form a wide band array antenna. The dielectric plate also enables the antenna to maintain low sidelobes level over the frequency range of 58 to 64.4 GHz, corresponding to the gain of higher than 23 dBi with larger than 66 % antenna efficiency.

CHAPTER FOUR: MULTIBEAM LENS ANTENNA ARRAY

4.1 Background

It is widely known that at high frequencies, the electromagnetic wave suffers from more severe free-space loss and blockage, which substantially degrades the signal-to-interference-noise ratio. To cope with this shortcoming, as mentioned in previous chapters, high-gain antennas with a directional beam can be deployed (possibly at both transmitting and receiving ends), which greatly enhances the SNR, and improves the data security, thus they have been widely used in long-range mmWave point-to-point communications with a LOS link [12], [22]. However, the narrow fixed single beam of a high gain antenna provides only limited spatial coverage, making it not amenable to multiuser mobile streaming. In addition, for non-LOS communications, another requirement for 5G backhaul antennas is their compatibility for beamsteering. The beam steering feature is required, because it helps to focus signals in a concentrated beam that is very directive, and reducing signal blockage, thus decreasing interference among different users. The single fixed directional beam needs to be steered either electronically or mechanically in order to find a reliable substitute link (see Fig. 1). Beam steering is about changing the direction of the main lobe of a radiation pattern. Therefore, the goal of this chapter is to design a multibeam cylindrical Luneburg lens antenna that could cover a large angular range and provide wide bandwidth. Actually, multibeam antennas serve as the key hardware for enabling mmWave backhaul links [25]–[27]. In radio and radar systems, beam steering may be accomplished by switching the antenna elements or by changing the relative phases of the RF signals driving the elements.

Many techniques have been used to steer an antenna's radiation pattern, the most practical techniques are mechanical steering and phased array antennas [71]. These antennas have primarily been used in radar and satellite communication systems over the years [72].

Mechanical steering involves manually turning the antenna to face the direction of interest, and is highly effective since it maintains the gain of the antenna and offers flexibility in the steering range of the antenna [73]. However, its use is limited to static due to the limitation in steering speed. Also, rotating mechanisms are prone to mechanical failure due to fatigue and wearing of moving parts [74]. Recently, MEMS devices have been used to implement mechanical steering [75], they offer improved speed of scanning compared to manually steered arrays as well as low losses to the system. Nevertheless, mechanical beamsteering becomes undesirable and difficult when we consider factors such as antenna size, weight, and weather conditions. The solutions for this problem led to electronic ways of steering beams, phase array antennas[71].

Phased array is an array of antenna elements whose excitation phase is controlled in order to get a desired beam steering angle. Phases of antenna elements can be controlled with phase shifters or delay circuits. Phased array is a conventional way of electronic beam steering with high scanning rate compared to mechanical beam steering [76]. However, an electronically steered phased array antenna system is very sophisticated and expensive. Because this technology requires all the antenna elements to be active simultaneously and utilizes phase shifters at every antenna element for electronic beam steering in which each element and phase shifter, consumes significant amount of DC electrical power, making the phased array technology very expensive [77]. An alternative to both the mechanically scanning antennas and electronically scanning phased array antenna system is the use of

the gradient-index (GRIN) lens-based antenna such as the Luneburg lens antenna[78] [79]. The Luneburg lens is a spherical shaped graded dielectric structure in which electromagnetic energy from a feed source placed on one surface of the lens radiates as a plane wave from the opposite surface of the sphere. This focusing nature of the Luneburg lens allows it to be used as a wide-angle beam scanning antenna element for multifunctional wideband antenna applications in which beam scanning is simply achieved by switching between an array of antenna feeds placed along the lens surface [79]. The benefits include high antenna gain, broad bandwidth, multiple simultaneous beams and reduced electrical power consumption. Taking advantage of the much smaller wavelength at mmWave frequencies as compared to that in the sub-6-GHz spectrum, compact multibeam antenna with higher gain can be implemented at mmWave base stations and user terminals of a 5G system to enable dynamic and reliable wireless links for high-speed data transferring (in particular, the ability to form multiple simultaneous beams without any mechanical moving parts and the presence of the feed source at the back of the antenna make the Luneburg lens an attractive choice to use as wide-angle, multi-beam, multiband antenna applications such as wireless communications and direction finding [80][81][82].

4.2 Lens Antenna

Lenses have been used in the fields of optics and electromagnetics for many years. A lens is typically composed of a dielectric material, in which the shape and the type of the dielectric material are the key parameters of the lens performance [72]. A lens has the ability to refract light or electromagnetic radiation as it is transmitted through the lens. The lens can be used to either converge or diverge the transmitted beam depending on the application. Lenses have been used with antennas to shape electromagnetic radiation into

the desired pattern. In this case, one side of the lens is illuminated by the input waves emitted from the feeding antennas, while the other side of the lens serves as the radiating aperture. Lenses control the incident radiation to prevent it from spreading in undesired directions. Depending on the type of lens and application, the radiation can be focused to a certain point or spread out to cover a wider area.

The principle operation of the lens is based on the refraction of electromagnetic waves at the lens surfaces [83]. The index of refraction is based upon the material of the lens and is given by:

$$n = \sqrt{\epsilon_r \mu_r} \quad (4.1)$$

Lenses and reflectors are used as collimating elements in microwave antennas. Compared to reflectors, lenses have more degrees of freedom [inner surface, outer surface, index of refraction, n], and have no aperture blockage by the feed. Lenses are more commonly utilized at higher frequency. At lower frequencies, the lens tends to be very large and heavy. Fig. 3 shows basic configurations of a lens and reflector antenna. One main advantage of lenses over reflectors is that the feed and its supporting structure do not block the antenna aperture. This back feeding feature is key for the development of the millimeter and sub-millimeter wave integrated lens antenna concept where the lens base is positioned directly in contact with the feed, such as an integrated circuit front-end, to produce a directive radiation pattern, either single-beam or multiple-beam.

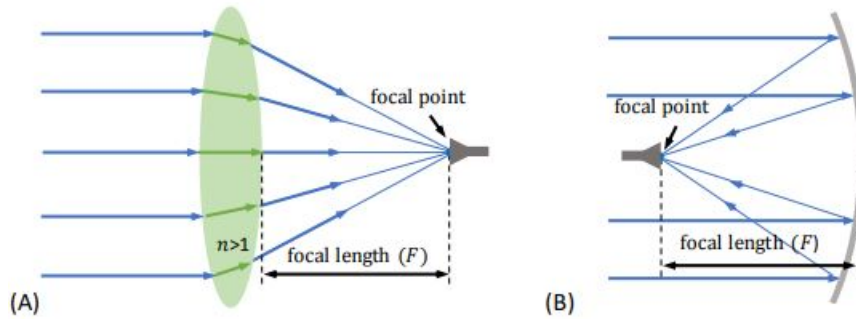


Figure 4.1. Focusing antennas: (A) lens; (B) reflector

The lens classification is based on three different physical characteristics: the feed position relative to the lens body (far from the lens or in direct contact), refractive index profile (constant/stepped or non-uniform) and number of refraction surfaces, see Table 4-1. For each of these categories the lenses can be further classified according to the type of output radiation pattern: fixed-beam (collimated or shaped) or scanning beam (usually collimated). In early lenses and in a few current designs the focal point is located well away from the lens, at a distance comparable with its diameter as in Figure 4.1 (A). These lenses are named the off-body fed lenses and all examples found in the literature are axial symmetric. Lens with feed antenna at a distance of multiple wavelengths from the lens

Table 4.1. Lens Classification Based On Physical Characteristics.

Off-body fed	Homogeneous	A. Single refraction
		B. Multiple refraction
Integrated	Homogenous	C. Single refraction
		D. Multiple refraction
	Non-uniform index	E. Continuous refraction
		F. Multiple refraction

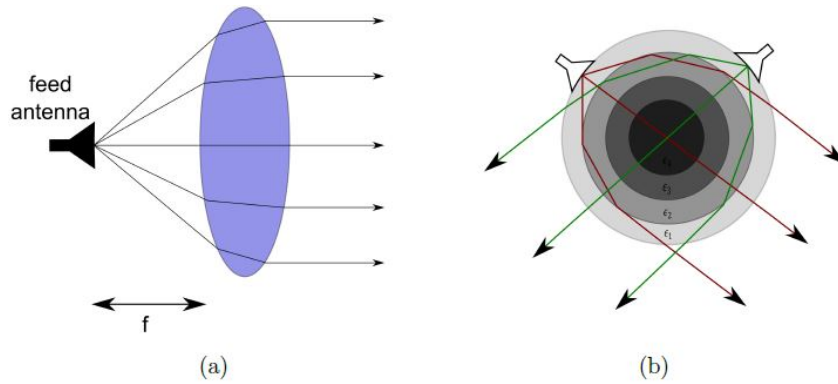


Figure 4.2. (a) Off-body feed homogenous lens and (b) an integrated feed Luneburg lens.

body is termed as an off -body feed lens as shown in Figure 4.2 (a). Lenses with feed antenna in direct contact or less than a wavelength away from the lens body is known as an integrated feed lens or integrated lens antenna [84].

Based on the number of refracting surfaces, lens antenna can be further categorized as:

- Uniform/Homogenous Lens: Lens made from a single dielectric material, which have a single refraction surface.
- Non-Uniform Index Lens: Lens made from two or more materials with different dielectric properties that have multiple refraction surfaces is known as a non-uniform index lens [84]. As shown in Figure 4.2 (b), lens made of layers of various dielectric materials is a good example of non-uniform index lens.

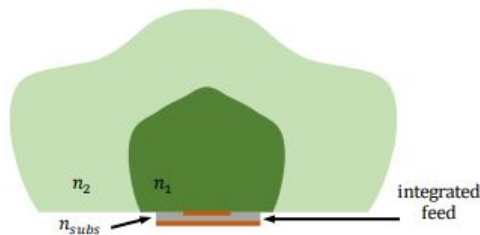


Figure 4.3. Shaped integrated dielectric lens antenna.

With the fast advances on the millimeter and sub-millimeter waves circuit technology for the past two decades, there has been an interest in lens antennas, which present a more acceptable size at these frequencies. In most cases the target radiation pattern continues to be the collimated beam type (plane wave output), either fixed or scanning [79]. For instance, in one of its most basic configurations, Figure 4.1 (a), parallel rays of an incident plane wave are refracted at the lens surfaces in such a way that all output rays intersect at a point, the lens focal point. All these rays have the same electrical path length, that is, they arrive in phase at the focal point, despite their different physical lengths which are compensated by a slower phase velocity ($v=c/n$) in different portions of the lens.

4.3 Luneburg Lens

Dielectric lenses come in many different shapes, which effect the diffraction of the radiated beam. The Luneburg lens is one of the oldest types of dielectric lens. R.K Luneburg first developed the Luneburg lens in 1944 [78]. Generally, it is composed of a spherical shape dielectric lens excited with a feed antenna, which typically is a horn antenna. The Luneburg lens is a special case of integrated lenses, with non-uniform refractive index (gradient-index lens), where ideally an incident plane wave is focused on the antipodal point on the lens surface, see Figure 4.2 (b).

A Luneburg lens can be used as the basis of a high-gain radio antenna, and it is comparable to reflector antennas at high frequency applications. A Luneburg lens antenna offers a number of advantages over a parabolic reflector antenna.

- Because the lens is spherically symmetric, the feed antenna can be steered by moving the feed around the lens, without having to bodily rotate the whole antenna.

- Again, because the lens is spherically symmetric, a single lens can be used with several feeds looking in widely different directions. In contrast, if multiple feeds are used with a parabolic reflector, all must be within a small angle of the optical axis to avoid comatic aberration (a form of de-focusing).
- Apart from offset systems, reflector antennas suffer from the feed and its supporting structure partially obscuring the main element (aperture blockage); as with the reflector antenna, a feed to the receiver or from the transmitter is placed at the focus point in front of the reflector aperture. However, the Luneburg lens antenna avoids this problem [85].
- The Luneburg lens is composed of a feed element and a spherical dielectric lens, in which the feed element is positioned at the focal point of the lens, the phase center of the feed horn must coincide with the point of focus. The lens focuses an incoming wave into a point on the boundary of the sphere, which is in the opposite side of the entry point. Each point on the surface of an ideal Luneburg lens is the focal point for parallel radiation incident on the opposite side (see Figure 4.4). Therefore, the lens is also able to form multiple beams in arbitrary directions by moving the feed location around the lens [86].

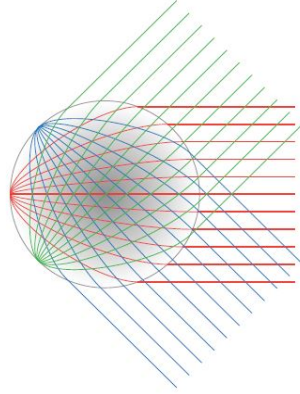


Figure 4.4. Luneburg lens ray tracing paths for three different points on the sphere/cylinder perimeter, each shown in a separate colour

4.3.1 Basic operation of Luneburg lens

The main characteristic of the Luneburg lens is that the index of refraction varies with the radius of the sphere [83]. The index of refraction in terms of radius determines the path of the beam through the lens. The index of refraction relates to the radius according to:

$$\varepsilon_r = 2 - (r/R)^2 \quad (4.2)$$

Where R is the radius of the lens. The lens has a radially graded refractive index with a maximum value at the center and a value of unity at the surface. In the case described by Luneburg, the refractive index is “1” at the surface and “ $\sqrt{2}$ ” at the center (see Figure 4.5). There are many variations of the Luneburg since the index of refraction inside the lens can be varied to change the ray path. Some variations of the Luneburg lens include the Maxwell fisheye, Eaton lens, and isotropic lens [83]. Perfect Luneburg lenses are difficult to make in practice, then approximate versions have been reported to realize the ideal permittivity law

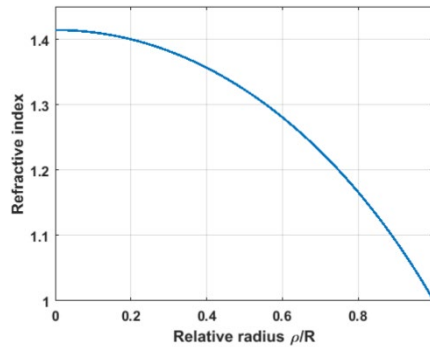


Figure 4.5. Refractive index variation of a standard Luneburg lens [6]

of equation 4.2. Nowadays, a discrete number of concentric dielectric layers that approximate the ideal permittivity law forms Luneburg lenses. It is expected that as the number of discrete layers increases the performance of the lens improves; however, the manufacturing complexity increases as well as the influence of possible air gaps between the layers [87]. It has been demonstrated that a quite small number of shells is enough to obtain a directivity and side lobe level close to the ideal case [88]. Nevertheless, the recommended number of discrete layers increases with the lens diameter compared to the wavelength. For example, just 6 layers were required to achieve adequate performance with an $0.8\lambda_0$ diameter Luneburg lens. Even lesser number of layers is possible by optimizing both the permittivity and thickness of the layers [89]-[90]. There are also examples of Luneburg lenses fabricated from a single material with a controllable dielectric constant. For instance in [91] a 3D rapid prototyping machine was used to achieve the desired permittivity value by controlling the filling ratio of a polymer/air-based unit cell. Alternatively, it is possible to use foam material and press it to obtain the desired dielectric constant. In fact, when the pressure increases and the foam is compacted, the quantity of air in the material decreases increasing the permittivity. This technique has been tested for the fabrication of a Luneburg lens in [92]. It is also possible to control the dielectric

constant in the Luneburg lens by drilling holes into the material and varying either the diameter of the holes or their density [80]- [93].

One of the major disadvantages of the spherical Luneburg lens is its high profile. A commonly used solution to reduce the profile of the Luneburg lens by a factor of 2, is to combine half of the lens with a flat ground plane, (Figure 4.6). The ground plane creates an image of the upper hemisphere and simulates the complete Luneburg lens. The size of the ground plane must be adequate to produce the required image, and the necessary dimensions are a function of the elevation angle of the beam in relation to the ground plane. An insufficient ground plane size will reduce the directivity of the beam and cause scanning loss. This hemispheric lens solution also suffers from feed blockage for high elevation angles. One advantage of this configuration is that it is easier to mechanically stabilize than the complete spherical lens. Furthermore, for more simplification, a quarter Luneburg lens with a 90° degree corner ground plane has been demonstrated [94].

Transportation optics [95] can be used to change the shape of the lens into a much lower profile. A reasonable performance has been achieved with a compacted Luneburg lens with cylindrical geometry (Figure 4.7) [96]. As the spherical lens enables beam-steering in both vertical and azimuth planes, in some applications beam-scanning can be confined to one plane. To make a compact antenna with a cylinder, based on Luneburg lens operation, the variation of the dielectric constant occurs only in the radial direction. In this solution the beam collimation is obtained only in one plane, leading to fan shaped beams instead of pencil like beams in a spherical Luneburg lens [97].

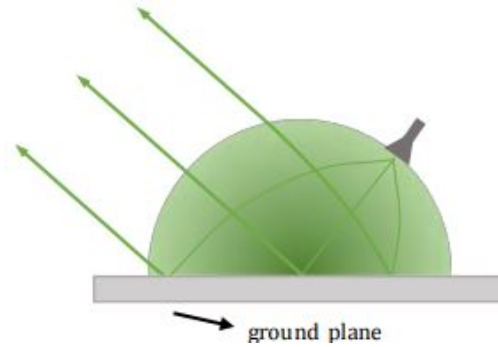


Figure 4.6. Half hemisphere Luneburg lens.



Figure 4.7. Cylindrical Luneburg lens.

4.4 Cylindrical Luneburg Lens Antenna

Although the Luneburg lens offers significant potential benefits over phased array systems and reflector antennas to use as a high gain, multibeam antenna element, the lens in its spherical shape is incompatible for practical antenna applications. The spherical geometry of the Luneburg lens structure poses a significant implementation challenge as it complicates the integration of the standard planar feed sources (e.g. waveguides, antenna arrays, detectors) to the lens's spherical surface. To eliminate this feed mismatch problem between the spherical Luneburg lens and planar feed elements, a more convenient approach is to use a modified three-dimensional Luneburg lens antenna in which the lens's spherical profile is reduced into a two dimensional cylindrical shape to successfully simplify the integration of antenna. To design such a modified Luneburg lens antenna while maintaining the Luneburg lens original electromagnetic performances, various designs of cylindrical lens antenna developed and has drawn great interest among antenna and electromagnetic

research. Based on recent studies, in two-dimensional lenses, the variation of refractive index n_{eff} depends on the mode propagation, the thickness of the lenses (t) and the relative permittivity constant of the dielectric (ϵ_r). The following sections reviews various implementation techniques of two-dimensional gradient index lenses.

4.4.1 Geodesic lens

Geodesic lenses are one class of two-dimensional Luneburg lenses composed of a pair of non-planar metal plates [98]-[99]. According to [99] in KTH University, the authors describe a new design procedure of a geodesic lens enabling a time-efficient evaluation of the focusing properties of modulated geodesic lenses using ray tracing on the equivalent gradient-index planar lens. This lens is based on parallel plate waveguide (PPW) technology in which the refractive index variation is based on varying contoured inner and outer PPW surfaces spaced a constant distance apart with a spacing small enough so that only a TEM mode can propagate. Figure 4.7 shows the geometry of this type of lens. This approach is of interest to optimize modulated geodesic lenses having polynomial profiles, reducing their height while preserving their wideband behavior and wide angular focusing properties. The approach is validated with a specific lens design. The profile is optimized at 30 GHz, while the focusing properties are monitored over the complete Ka up-link frequency band allocated to satellite communications (i.e., 27.5–31 GHz). The manufactured prototype produces 21 beams equally spaced every 7.5° over the extended angular range of $\pm 75^\circ$ (Figure 4.8 (b)). The manufactured design has return loss better than 15 dB over a fractional frequency bandwidth larger than 30%, in line with the predictions.

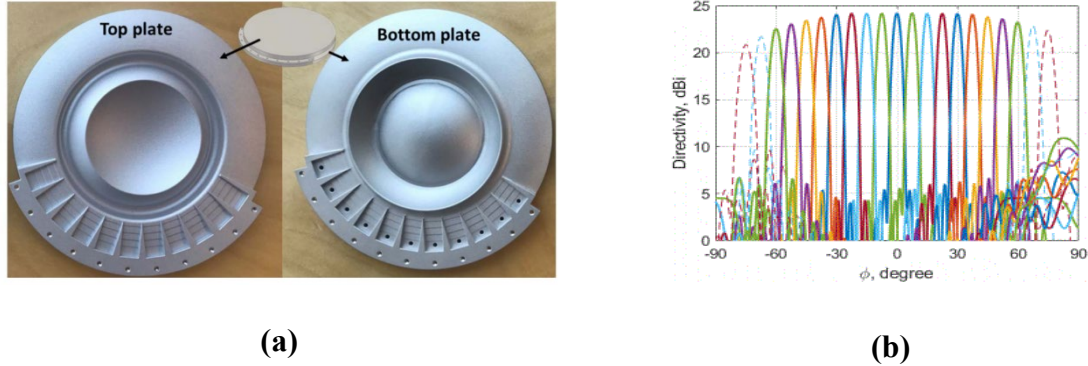


Figure 4.8. (a) Antenna configuration, (b) Multi-beam radiation pattern

4.4.2 Cylindrical LL based on partially filled - air filled Parallel Plate Waveguide

An excellent design and prototype of a two-dimensional cylindrical Luneburg lens are introduced in [100]. It is based on TE_{10} mode propagation between the two parallel plates. As shown in Figure 4.9, the parallel plates are partially filled with low cost Rexolite polymer material ($\epsilon_r = 2.54$). The refractive index is modulated by the filling factor of the dielectric between the plates, i.e. the thickness. With a diameter of 100 mm, HPBW of 6.6° and 54° are obtained in E- and H-plane, respectively. Side-lobe levels in E-plane is -17.7 dB, the radiation efficiency between 43% and 72%. This implementation is broadband, in Ka-band, and easy to manufacture. Further, the authors discussed different structures of this type of cylindrical lens in [100]. Several designs based on the parallel plate and dielectric profile are presented for single and multibeam applications (see Figure 4.10). In another work [101] in order to avoid dielectric losses for millimeter wave applications an air-filled symmetric and almost parallel-plate waveguide modified Luneburg lens is designed at 30 GHz and fabricated. The antenna is fed by planar antipodal linearly-tapered slot antenna (AL TSA) in which the PPW spacing should be chosen such that $\lambda_0/2 < h < \lambda_0$ (see Figure 4.11).

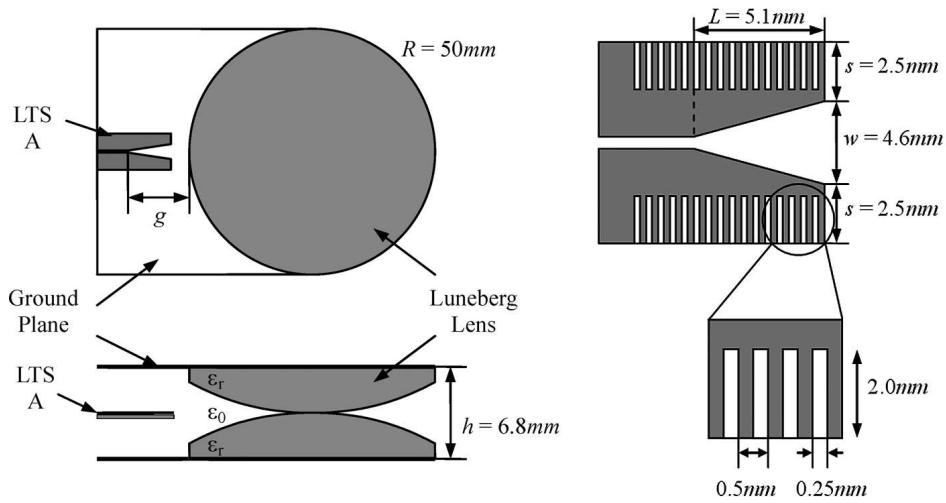


Figure 4.9. LTS A-fed cylindrical Luneburg lens antenna

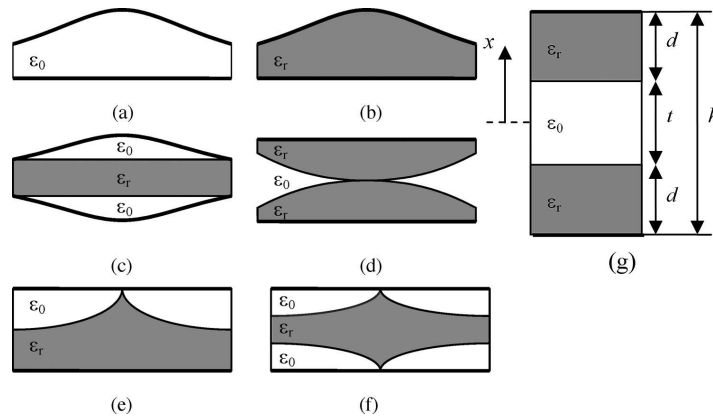


Figure 4.10. (a)-(f) Cross-section view of possible profiles of cylindrical Luneburg lens.

4.4.3 Metal-posts as an Artificial Dielectric Material

In [102], it is theoretically demonstrated and experimentally validated that a periodic and regular metal posts array on a ground plane, as shown in Figure 4.12 (a) and Figure 4.12 (b), can act as an artificial dielectric material, and therefore can be operated as a lens. The posts size, spacing, and height controls the refractive index. It is important

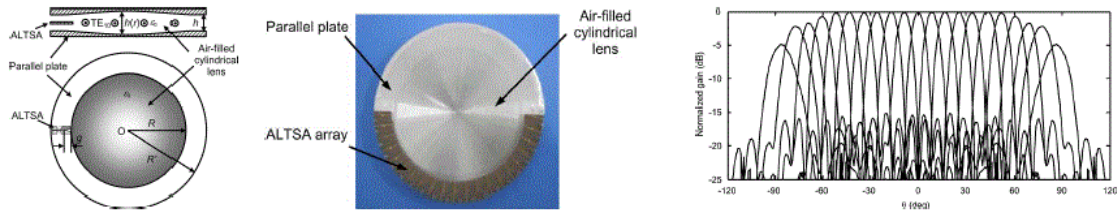


Figure 4.11. Air-filled symmetric parallel-plate waveguide modified Luneburg lens

to note that there is no upper ground plane on the top of the metal posts. The authors proposed an approximate analysis of the index based on a transverse resonance solution which gives an analytical formula to derive n_{eff} from the physical parameters of the metal post structure.

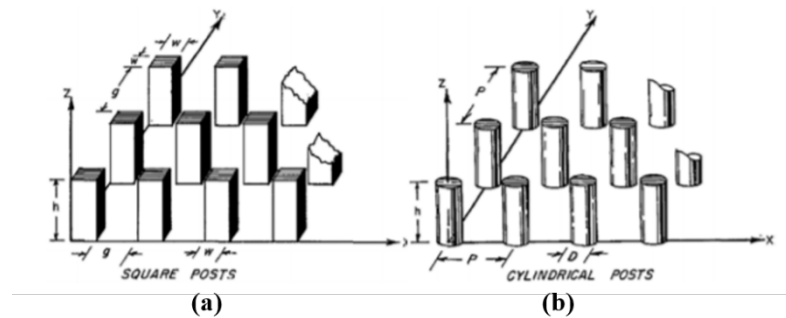


Figure 4.12. Surface-wave structure with (a) square metal posts and (b) cylindrical metal posts.

In another work as an all-metal Luneburg lens at 76.5 GHz [103], a photonic bandgap (PBG) structure, based on periodic and regular metal posts in a parallel plate waveguide, is proposed. The concept is applied to design and fabricate an asymmetric parallel-plate waveguide Luneburg lens at 76.5 GHz for adaptive-cruise-control radar application. Contrary to [104], in this work, there is an upper plate on the top of the metal posts, and it can be noted that the PPW spacing is constant. Figure 4.13 gives the geometry of the lens and the flare.

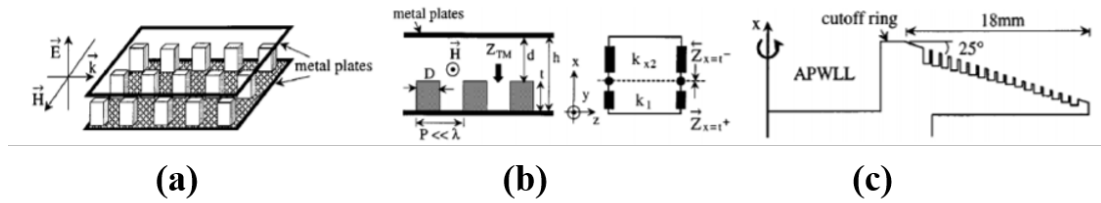


Figure 4.13. Geometry of the PBG structure with (a) a 3D view of the periodic and regular square metal posts in square lattice in a parallel-plate waveguide and (b) the cross-sectional view and transverse resonance equivalent circuit of the structure. (c) Cross-sectional view of the rotationally symmetric corrugated flare [103].

In [104], the influence of lattices and metal posts shapes on the performances of an asymmetric parallel-plate waveguide Luneburg lens (APWLL) is studied at millimeter-wave frequencies. Square, hexagonal and circular metal post shapes were considered, and also square and hexagonal lattices, as shown in Figure 4.14 (a) and Figure 4.14 (b), respectively. It was found that a hexagonal lattice with circular-shaped metal posts is best as an actual isotropic homogeneous artificial material with angular independency, which also leads to better performances, lower scanning losses and SLL.

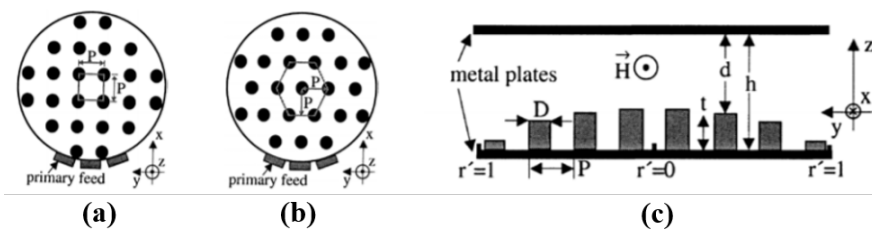


Figure 4.14. APWLLs with circular posts. (a) Top view with square lattice (b) Top view with hexagonal lattice. (c) Cross-sectional view: $D=0.38$ mm, $P=0.78$ mm, $h=1.9$ mm.

CHAPTER FIVE: BEAM-STEERING LENS ANTENNA FOR POINT TO MULTIPOINT COMMUNICATIONS AT 28 GHZ BAND

5.1 Introduction

Beam steering is an important technique in the high performance modern wireless telecommunication and automotive radar systems. Conventional beam steering, such as phased array, reflectarray, and mechanical beam steering are commonly implemented in a wide field of applications over the years [105]-[106]. Recently, considerable research interests have been dedicated to millimeter wave (mm-wave) communication systems in which a new generation of beam steering antennas based on Luneburg lens technology are dominating research areas in mm-wave frequencies [107]–[109]. As illustrated in Chapter 4, a Luneburg lens is a gradient index lens originally referring to a dielectric lens of a spherical or cylindrical shape, which possesses rotational symmetry and focusing properties, and enables beam-scanning capabilities amongst multiple feed elements [110]. As mentioned in Chapter 4, significant investigations utilizing diverse approaches have been implemented to develop cylindrical LL antennas [81], [111]–[113]. The cylindrical Luneburg lens-based antennas are transmitting devices that provide the targeted fan-beam radiation pattern. Various gradient-index lenses have been extensively studied, among which the most widely known ones are the parallel plate waveguide lenses. Since each point on the curved lens periphery is a focal point, 1-D scanning has been achieved when these types of gradient-index lenses are fed by an linear array of antennas. Among the reported designs, lenses developed based on the parallel plate waveguide (PPW) technique

have attracted much attention [101],[114]-[115]. These antennas exhibit excellent performance and provide a wide fan beam scanning coverage. For instance, a PPW lens with 21-element antipodal linearly tapered slot array feed is realized in [101] covering $\pm 90^\circ$ continuous beam scanning in the azimuth plane. Furthermore, a fully metallic geodesic lens demonstrated in [114] can scan over $\pm 62.5^\circ$ over a wide bandwidth from 25 to 36 GHz. Meanwhile, due to their low loss and fully metallic frameworks, they achieve dominance attention at a higher range of frequencies. However, in order to realize gradient index behavior of the lens, both the parallel plates and the dielectric lens require curved and irregular profiles in their structures leading to intensive time-consuming simulation and optimization processes. Besides, they bring limitation and complication to the fabrication of the antenna. Mechanically, the implementation of a complex electrically-sensitive curved shape configuration requires precise fabrication processes, which will be highly costly with the current standard manufacturing techniques. Moreover, despite the low and compact profile of the presented planar feed elements for the feed part of the antennas in [101], [113], their dielectric based structure might cause some difficulties and inconvenience to feed integration. Especially, for a large number of feed elements, it might be associated with some challenges requiring tight tolerances for proper fit in a curved focal area between the two metallic plates.

In this chapter, a low cost and flexible design of a PPW multi-beam lens antenna operating at 28 GHz is presented. A thin layer of a homogeneous cylindrical dielectric material flexibly adjusted between the two parallel plates wherein the plates with uniform surfaces are separated with a fixed separation. Here, against prior PPW lenses [110], the proposed configuration without any complex countered profile for both metallic plates and

dielectric material provides proper and effective focusing and beam switching properties. To illuminate the lens, waveguide feed elements are directly incorporated into the parallel plates to facilitate feed integration with the plates and provide easy integration, low loss performance and high power-handling capability. Details of the antenna design, simulation and measurement results are presented and discussed.

5.2 Analysis and Design of the Multi-Beam Lens

Figure 5.1 shows the structure of the proposed symmetric multi-beam PPW lens antenna. The antenna consists of two parallel metallic plates lying at $x = 0$ and $x = h$ planes. The narrow insulating gap of h between the two plates are partially filled by air and dielectric material making the feed placement and radiating aperture of the antenna, respectively. As shown in Figure 5.1, in the free space region between the plates, the feed part of the antenna is composed of an array of nine waveguide feed elements connected to the metallic plates, and distributed closely next to each other at a distance d from the edge of the dielectric material.

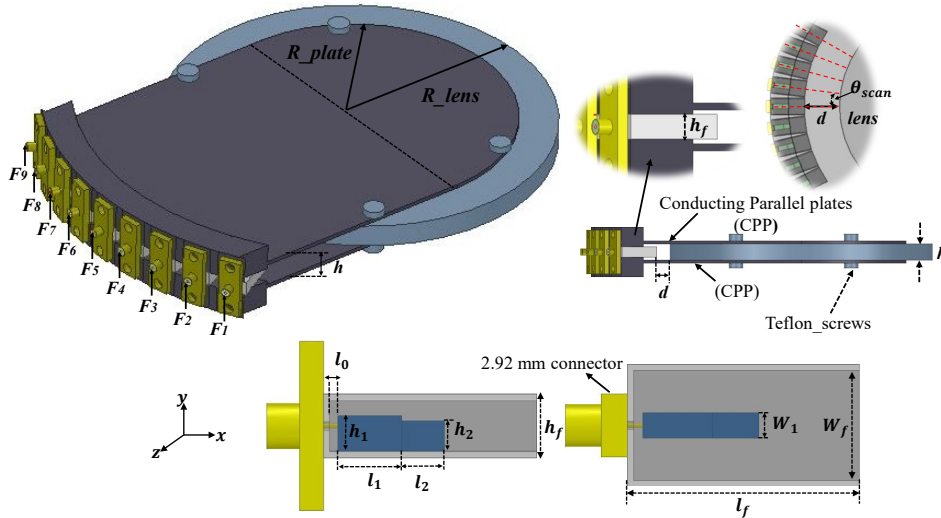


Figure 5. 1. View of the Antenna structure. The optimized parameters are: $h_1 = 1$ mm, $h_2 = 1.2$ mm, $w_1 = 2.2$ mm, $l_0 = 1$ mm, $l_1 = 4$ mm, $l_2 = 3$ mm, $w_f = 7$ mm, $h_f = 3$ mm, $R = 50$ mm, $h = 5.3$ mm

5.3 Feed Design

In order to achieve a low loss and low cost PPW lens antenna for millimeter wave applications, an open-ended rectangular waveguide is investigated in this work as the feed part of the antenna. Since the top plate and bottom plate of the PPW structure have metallic materials, it can be seen in Figure 5.1 that the metallic waveguide feed embedded between the two plates provides the advantage of simple and integrated feed structure. Planar feed elements such as linearly tapered slot antennas (LTSA) are widely used by prior works to assemble a compact low profile PPW lens antenna with a wide scan coverage [101],[110]. However, planar feeds often suffer from conducting and dielectric losses, which significantly decreases antenna efficiency at higher frequencies. Moreover, it presents serious problems in the manufacturing and assembly processes derived from the physical constraints imposed by the placement of the planar feeding elements between the two metallic parallel plates. Therefore, for the purpose of introducing a flexible design and fabrication solution to overcome these limitations, we proposed a new structure of PPW

lens antenna using a coaxial waveguide feed technique for the feed part of the antenna. Hence, a waveguide feed with rectangular cross section is designed operating at 28GHz. Figure 5.1 shows the geometry of the feed excited by a coaxial line probe. Coaxial-waveguide transition contains a section of a regular waveguide by a short-circuited end wall and a section of a coaxial line located perpendicular to the wide wall of the waveguide. In order to provide good impedance matching, a matching element is made of a two-stepped matching element located inside the waveguide. As shown in Figure 5.1, the inner conductor of the coaxial probe is designed to be in contact with the wall of the matching section. To match the impedance of the coaxial cable (50Ω), which in this case is a standard coaxial of a 2.92 connector, the dimension of the matching element has been analyzed. We used the *ANSYS High Frequency Simulation Software (HFSS)* to model the waveguide feed and analyze its parameters. The waveguide is implemented with the aperture of $7 \text{ mm} \times 3 \text{ mm}$. The optimal parameters of the waveguide feed are provided in caption of Figure 5.1.

5.4 Lens Design

In the configuration shown in Figure 5.1, considering the propagation of waves in the region between the two parallel plates, a cylindrical lens antenna with switched beams capabilities is realized between the two plates. For the lens presented in this work, the PPW is supposed to be in z-direction in which the transmission of electromagnetic waves between the two plates is affected by a thin and uniform layer of a solid and homogenous cylindrical dielectric lens. Actually, in view of ray tracing analysis, the dielectric material changes the shape of input wavefronts and focuses them as a plane wave in free space. Here, the cylindrical dielectric is designed between the two plates utilizing the

polytetrafluoroethylene (PTFE) material with $\epsilon_r = 2.05$ and a loss tangent $\tan \delta = 0.001$ at 10 GHz. The lens is designed at 28 GHz. The lens has a radius of $R_{lens} = 5\lambda$ (50 mm), λ is the wavelength in free-space at the operating frequency, while the length and height of the PPW are $L = 110$ mm and $h = 5.3$ mm, respectively. To propagate only the TEM mode (mode TM₀ in the parallel plate), the plates separation (h) with a constant separation along the mode propagation in z -direction is selected to be 5.3 mm, which is below $\lambda/2$ at 28 GHz [110].

In the presence of the feed, the adjustment of the feed position with respect to the surface of the lens is a key issue in designing any types of lens antenna. In fact, the feed should be placed within the focal surface of the lens to obtain the best system illumination. In this way, in order to determine the optimal ratio of d/R , that the diffraction-limited pattern occurs the proposed lens is studied under the full-wave electromagnetic simulations. By means of genetic algorithm (GA) optimization processes in HFSS, by comparing the simulated results in terms of maximum gain, low sidelobe level, and optimal reflection coefficient at 28 GHz, it is found that a ratio of $d/R = 0.3$ showed the best antenna performance. Furthermore, we noticed that a proper adjustment of the ratio of R_{lens}/R_{plate} . (see Figure 5.1) enables to control the antenna radiation characteristics. Here, R_{plate} is tuned to modify the antenna structure and minimize the mainlobe radiation ripples in the H-plane pattern. As can be observed in Figure 5.2, by the proper adjustment of R_{plate} , the antenna achieves a peak gain of 18.7 dBi and a 1.9 dB gain enhancement compared with the antenna profile of $R_{lens}/R_{plate} = 1$. The simulated Co-Pol and Cross-Pol radiation patterns for H- and E-planes are shown in Figure 5.3. As can be observed good main beam shapes and reasonable sidelobes level are obtained for the center

feed element (feed number 5 in Figure 5.1). The simulated 3- dB beamwidths are 6.2° and 41° in the H- and E-planes, respectively, and the first sidelobe level in the H-plane is -20.7 dB. Subsequently, after finding the optimal value of the focal length and validating the focusing property of the lens through an optimization process, based on axial symmetry feature of the proposed cylindrical lens, more feed elements are implemented over the circular focal area of the lens to enable multi switched beams for different desired scan angles. To avoid the inter- element mutual couplings between individual feed antennas over the focal surface of the lens, the elements are spaced with an angular spacing of θ_{scan} . Hence, nine feed elements with the angular spacing of $\theta_{scan} = 7.2^\circ$ are symmetrically arranged next to each other on the circumference of the lens, permitting steerable radiation patterns by switching between the feed elements. Each feed element is represented with F1, F2, ... F9 as shown in Figure 5.1. Figure 5.4 (a) shows the simulated reflection coefficients and mutual couplings of the feed antennas, when the elements excited individually. As shown in Figure 5.4 (b) the beams can be easily scanned at different angles whereby the maximum directivity is obtained for all feed elements in the desired scan directions. The beam directions are designed to be in -28.8° , -21.6° , -14.4° , -7.2° , 0° , 7.2° , 14.4° , 21.6° , and 28.8° . The overlap between the adjacent antenna elements beams is -3.6 dB. Based on simulations in Figure 5.4 (b), due to coupling between neighboring feeds, in comparison to Fig.4, the side lobes level is increased to around -15 dB, which still features acceptable low values. Besides, we observed around 0.3 dB gain drop over the scan range.

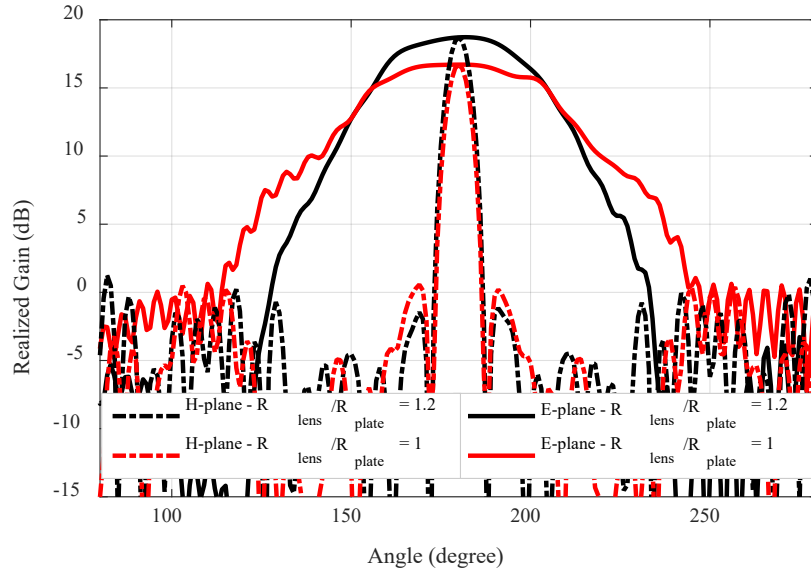


Figure 5.2. Simulated antenna radiation patterns in H- and E-planes for optimized value of R_{plate}/R_{lens} .

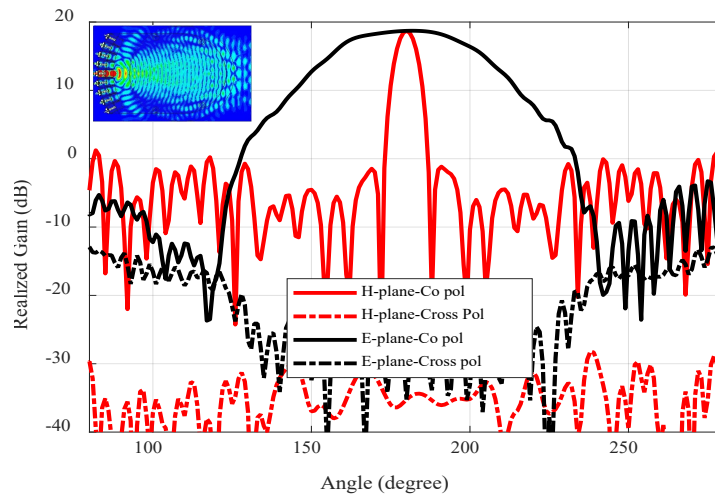


Figure 5.3. The simulated radiation patterns at 28 GHz of the single feed element.

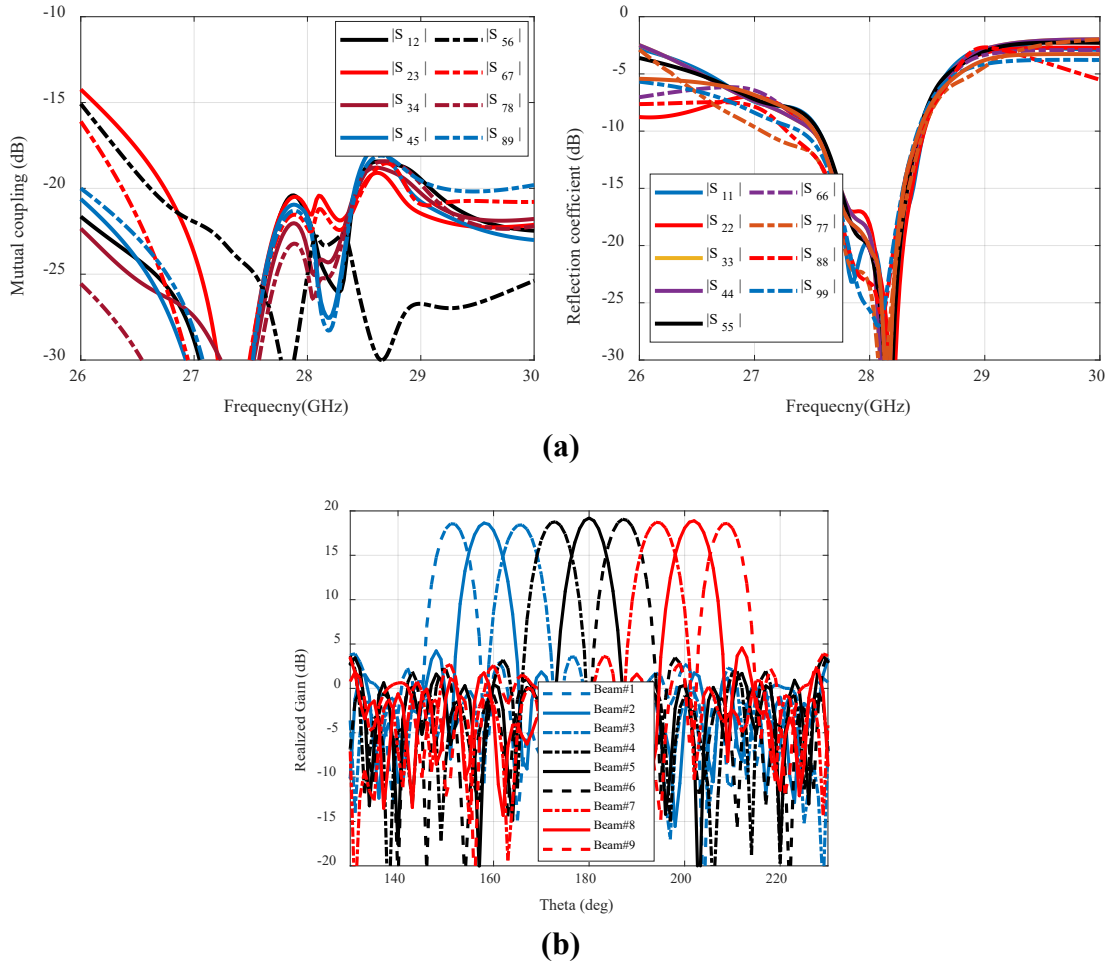


Figure 5.4. (a) Simulated reflection coefficients and mutual couplings of the proposed PPW lens, (b) Simulated H-plane Co-Pol broadside radiation patterns of the proposed PPW lens antenna at representative scan angles.

5.5 Experimental Results

To verify the proposed design, a prototype of the antenna is fabricated by using computer numerical control (CNC) milling machine technique. The prototype of the whole antenna is manufactured in four individual pieces including the metallic bottom and top plates, feed elements, and the cylindrical lens. Here, the plates spacing in the air region of PPW flexibly adjusted to the height of the waveguide feeds, i.e., $h_f = 3.8\text{mm}$ to fit feed elements between the plates. Then, tapped holes are formed in the top plate to assemble the feed array between the two plates. This directly attaches the feed part to the plates and

ensures that there is no air gap or separation between feed elements and the plates. The antenna prototype is shown in Figure 5.5. The total size of the antenna is $132 \text{ mm} \times 100 \text{ mm} \times 7 \text{ mm}$. Figure 5.6 exhibits the measured frequency characteristics of the manufactured antenna for all ports. The feed elements are assembled according to Figure 5.6, which is composed of a nine 2.92 mm coaxial connectors. The reflection coefficients are measured in which the testing feed element is set active and all other ports terminated by matched loads (50Ω). As shown in Figure 5.6 (a), reflection coefficients of better than -15 dB are achieved for all ports at 28GHz, and the coupling coefficients lower than -18 dB are obtained between adjacent ports (Figure 5.6 (b)). The antenna radiation pattern is measured in an anechoic chamber at the University of Colorado Boulder, USA, as shown in Figure 5.5. Figure 5.7 shows the measured E- and H-planes radiation patterns for the nine-feed elements. By simply switching between the feed elements, a scan angle of 57.8 degree is achieved over the azimuth plane.

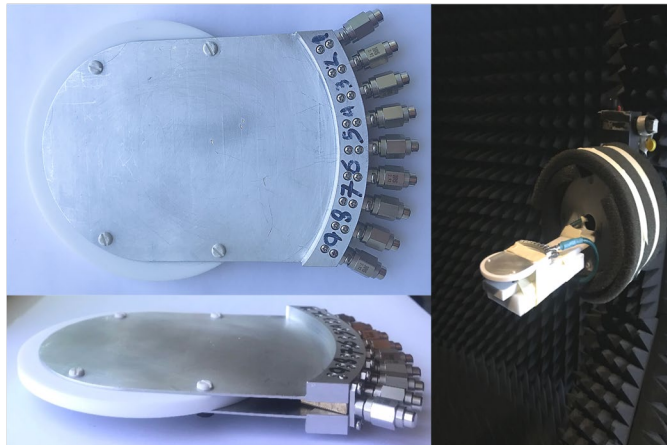


Figure 5.5. Prototype of the proposed array antenna

As observed, the measured scanning radiation patterns match reasonably well with the simulated ones in Figure 5.4 (b).

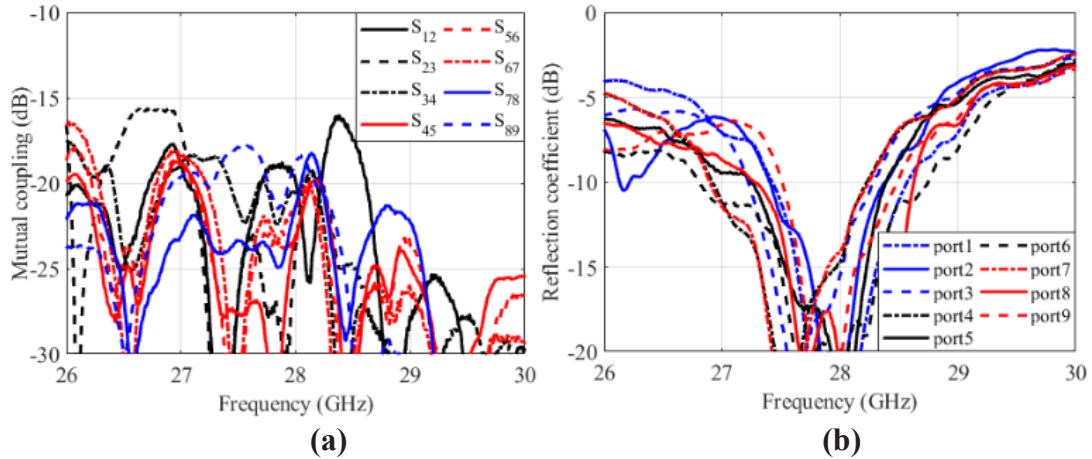


Figure 5.6. The measured, (a) input reflection coefficient for all ports and, (b). port coupling coefficients of the fabricated prototype.

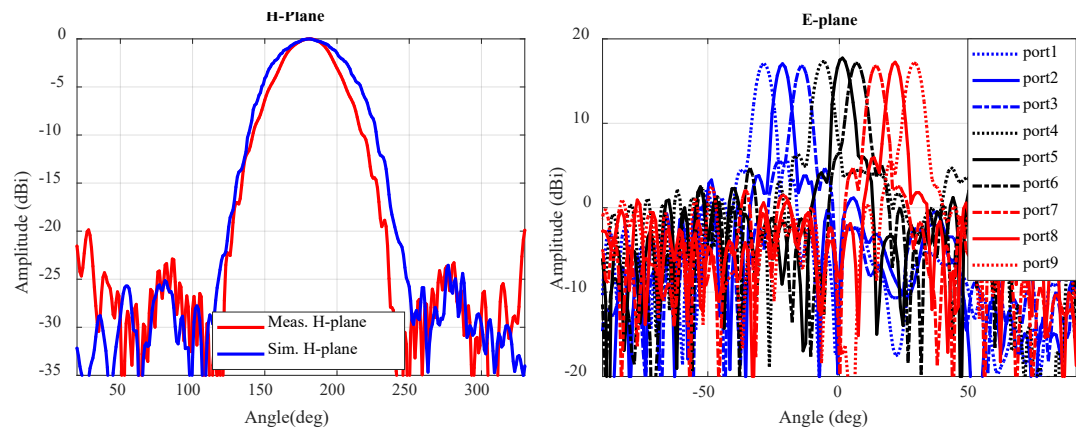


Figure 5.7. The measured plane radiation patterns of the fabricated PPW LL antenna at 28 GHz.

Table 5.1. Radiation characteristics of the nine individual ports of the proposed antenna

Port number	1	2	3	4	5	6	7	8	9
Beam width (deg)	6.37	6.2	6.3	6.1	6.2	6.2	6.4	6.3	6.1
Peak gain (dB)	17.08	17.05	17	17.29	17.73	17.12	16.8	17.24	17.17
First sidelobe level (dB)	-12.68	-13.25	-12.4	-12.2	-13.64	-12.17	-12.12	-12.9	-12.2
Sim-Scan of direction (deg)	28.8	21.6	14.4	7.2	0	-7.2	-14.4	-21.6	-28.8
Meas-Scan of direction (deg)	28.2	21.2	14.2	6.1	-1.1	-5.9	-14.6	-21.6	-28.2

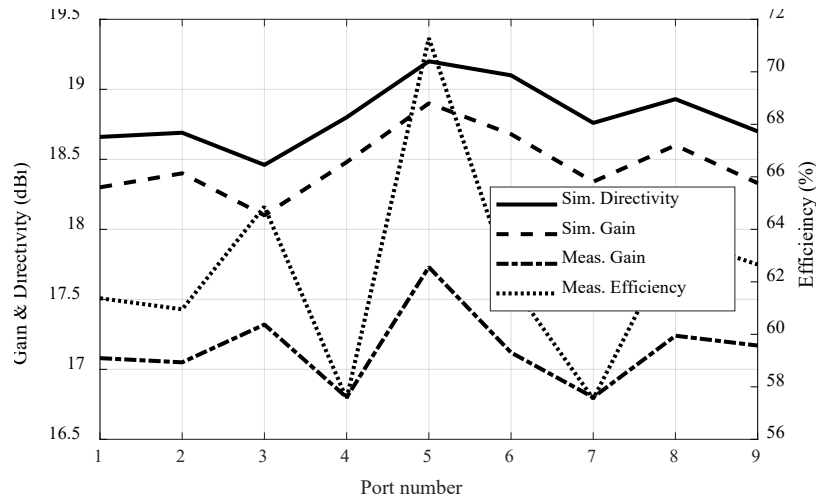


Figure 5.8. Simulated and Measured antenna directivity and gain for all ports of the fabricated PPW LL antenna.

The 3-dB beamwidths are about 6.6 ~ 6.3 degrees over the entire scan range. Detailed experimental measurements of the radiation characteristics of the antenna is summarized in Table 5.1. However, the measured patterns are slightly different from the simulated ones in Figure 5.4 (b). It is noticed that the peak of the radiation patterns has a slight difference from the expected directions. For example, port 6 has a beamsquint of 1.3 degrees from the desired direction. As a result, in comparison to simulation results, overlapping between the adjacent beams is varied as well. The measured results show that the beams overlap level varies from -4.2 dB to -3.1 dB between adjacent patterns. These results may be due to the tolerance of the fabrication process including improper plates spacing due to warpage in the metal plates after machining process and feeds angular positions with respect to the center of the lens. Figure. 5.8 presents the measured gains, as well as radiation efficiency variation for each individual port. The result demonstrates a gain variation of 0.93 dB in the entire scan range. The measured radiation efficiency of the antenna is between 57% and 72% for different ports. The variation in gain results can be attributed partly to the loss of dielectric material and 2.92 connectors.

5.6 Conclusion

In this chapter, a PPW lens antenna with beam steering capabilities is designed and manufactured operating at 28 GHz band. The proposed antenna offers the advantages of flexible design, low cost and easy integration can be implemented for 5G point-to-multipoint communication applications. Due to the metallic structure of the feed antennas between metallic parallel plates, the entire antenna is mechanically stable providing design flexibility with desired beam-steering capabilities. In the proposed design against the previous PPW LL designs, there is no need to use complex contoured profiles for the dielectric lens or change the plates' separation with special curvature to control the focusing property of the lens.

CHAPTER SIX: WIDEBAND BEAM-STEERABLE CYLINDRICAL LENS
ANTENNA WITH COMPACT INTEGRATED FEED ELEMENT

6.1 Introduction

In this chapter, a wideband and compact high gain Lunenburg -based lens antenna for the Ka-band is proposed. The main potential applications are for 5G wireless communication systems and automotive radar applications. The antenna provides about 46.7% of bandwidth ($|S_{11}| \leq -10$ dB) covering a frequency band ranging from 23.6 - 38 GHz. It also exhibits excellent propagation characteristics with only a 2.7 dB maximum gain variation with sidelobe levels lower than -18 dB over the entire bandwidth. In addition, with a multi-feed system, the antenna presents a beam switching capability of $\pm 32^\circ$ in the azimuth plane with a gain fluctuation of less than 0.4 dB and sidelobes levels of less than -14 dB over the entire scan range. The simulated results show that the proposed antenna features a simple structure while supporting wider bandwidth and lower sidelobes levels when compared to that of Parallel Plate Waveguide (PPW) Luneburg-based lens antennas.

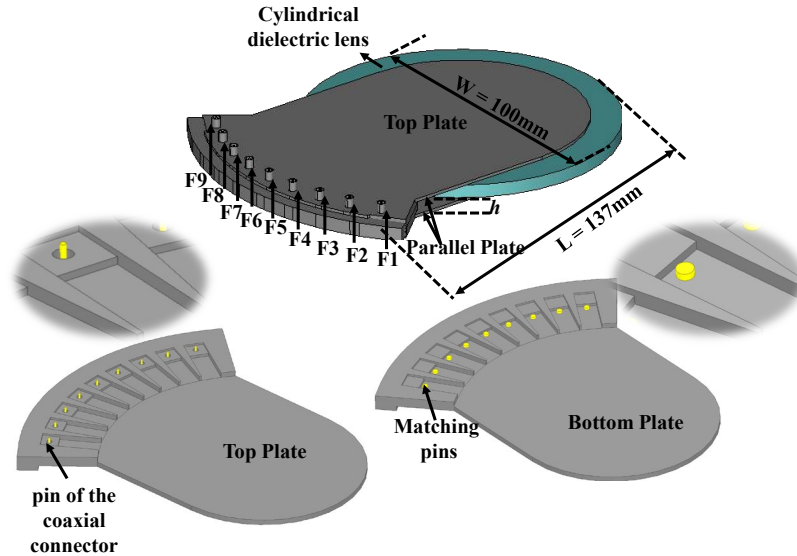


Figure 6.1. Antenna configuration.

6.2 Analysis and Design of the Multi-Beam Lens

Figure 6.1 shows the antenna configuration consisting of two parallel conducting plates spaced with a narrow spacing of h , and partially filled by air and a dielectric material making the feed placement and radiating aperture of the antenna, respectively. As shown in Figure 6.1, an array of 9-element coaxial connectors on the top plate is distributed closely next to each other at a distance from the edge of the dielectric material. Moreover, for the purpose of bandwidth improvement, nine elements of metallic matching pins are embedded inside the PPW at the inner surface of the bottom plate.

6.2.1 Feed Design

In order to achieve a low-loss and easy implementation of PPW Luneburg-based lens antenna for mm-wave applications, a simple integrated feed element is investigated in this section. Planar microstrip feed antennas due to their lightweight, compact and ease of fabrication, are widely used as a feed element in PPW antennas [101]. However, it is important to notice that they suffer from significant drawbacks. First, the placement of an

arrangement of substrate-based feed elements on a curved shape structure between two parallel plates, which have metallic material, is a challenging task and requires very tight assembly tolerances [4]. Second, the power loss due to the conducting and dielectric losses are unavoidable decreasing antenna efficiency at higher frequencies. Third, microstrip antennas typically suffer from narrow impedance bandwidth. Hence, to address these difficulties, here, we introduce a new wideband flexible design of a feed element directly integrated into the two parallel conducting plates. As can be observed in Figure 6.1, the feed element is created with a stepped discontinuity in the inner surfaces of the bottom and top plates. This actually corresponds to an axially symmetrical junction of two rectangular waveguides of equal widths and unequal height. Here, considering the desired frequency range at 24 GHz, the width of the waveguide sections is set to be 7.4 mm. Moreover, to excite the waveguide, as shown in Figure 6.1, it is interfaced with a standard 2.92 mm coaxial connector, where the inner pin of the connector for impedance consideration at a distance from the back wall of the waveguide is intruded into the waveguide. Further, a cylindrical matching pin with a height of h_p and a radius of r_p is implemented at a distance l_p from the back wall of the waveguide to control frequency characteristics of the antenna. In order to perform a comparison and demonstrate the importance of the introduced matching pin in the design, Figure 6.2 compares the simulated reflection coefficient of the feed element with and without the proposed matching pin over a wide frequency range. The simulations are performed with ANSYS High Frequency Structure Simulator (HFSS). Here, the parameters of the proposed pin are optimized to provide wideband performance. Actually, by comparison against the previous wideband feeds with multi-stepped configuration in [115] the proposed pin without adding extra complexity to the antenna

structure enhances the bandwidth of the feed element, which in practice, can be simply and cost-effectively implemented.

6.2.2 Lens Design

The schematic of the proposed homogenous lens antenna is presented in Figure 6.1, which is a cylindrical Luneburg-based lens antenna designed based on PPW technology. A conventional PPW structure is a transmission line composed of two identical parallel-conducting plates guiding electromagnetic (EM) waves between the two plates.

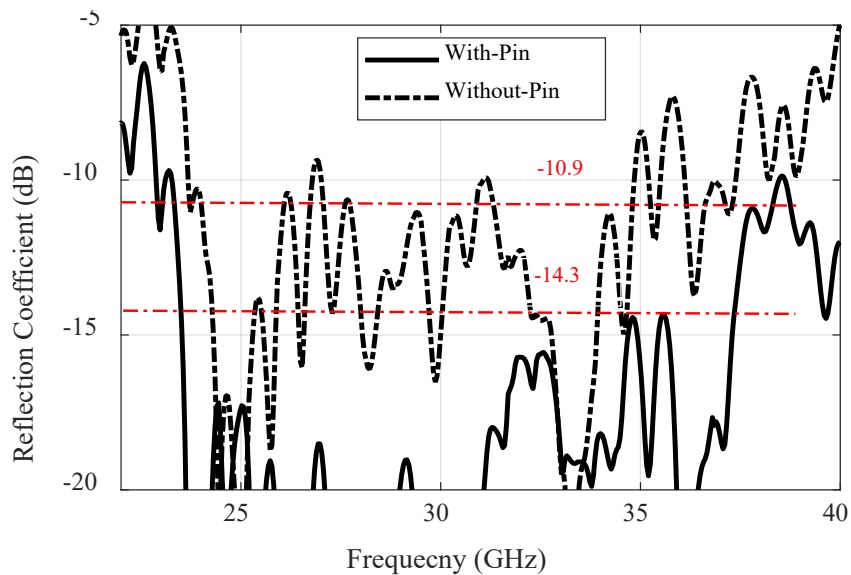
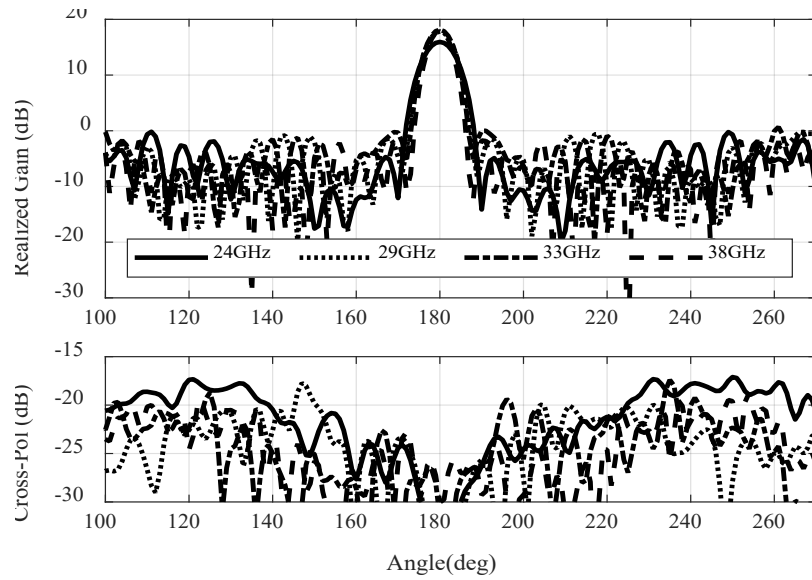


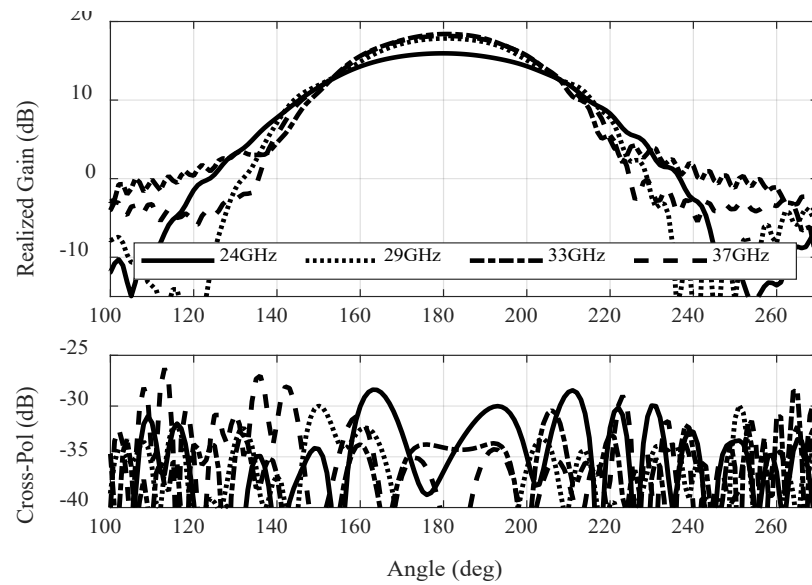
Figure 6.2. Simulated reflection coefficients of the antenna when the matching pin is loaded in the waveguide.

On the other hand, this structure can be implemented as a quasi-optical antenna to realize the features of a cylindrical LL antenna wherein the space between the plates is partially filled with a dielectric layer to approximate wave front transformation operation between two plates. Therefore, in the proposed antenna (see Figure 6.1), based on the conventional theory of LL with gradient index and focusing properties, wave front transformation of the lens is adjusted simultaneously by utilizing a single dielectric material with a cylindrical

cross section and a fixed and continuous PPW- spacing. Essentially, the shape, the thickness, and relative permittivity of the dielectric material play an important role on the antenna design to guarantee the desired wave-fronts transformation and beam- focusing property. Here, against previous PPW Luneburg-based lens antennas [101], [113] instead of having a complex curved structure for both the dielectric layer and parallel plates, we propose a very thin uniform and flexible structure operating over a wide frequency band covering Ka band.



(a)



(b)

Figure 6.3. Co- and Cross-polarizations radiation patterns of the single-fed PPW Luneburg-based lens for different frequencies in, (a) H-plane, (b) E-plane.

6.3 Single feed element integration with the lens

To illustrate the performance of the proposed PPW Luneburg based lens, we conducted full-wave simulations using an Ansys HFSS solver. Primarily, as the initial values, a lens of radius 50 mm and a focal distance $0.5 \times R_{lens}$ is defined for our design. Furthermore, to propagate only in the TEM mode (mode TM₀ in the parallel plate), a

constant plate spacing of 4 mm, which is below $\lambda/2$ at 24 GHz is used [110]. To start the simulations, the proposed waveguide feed element is placed at a distance from the surface of the lens. In the process of integrating the feed element within the structure of the lens, the position of the feed element with respect to the surface of the lens is a critical design parameter. This, in fact, determines the point at which a feed element performs with best efficiency developing the antenna's radiation characteristics to achieve maximum gain and low - sidelobes levels over a wide frequency range. The simulated E- and H-plane patterns for the optimum value of feed position are shown in Figure 6.3. It can be observed that integrated waveguide feed results in excellent E- and H-plane patterns over the wide bandwidth from 24 GHz to 38 GHz. The half-power bandwidths (-3 dB) of H- and E-planes vary from 8.04° to 6.23° , and 52.1° to 41.4° over the operating band, respectively. This corresponds to sidelobes levels below -18 dB in the H-plane and less than -20 dB in the E-plane. Furthermore, the cross-polarization levels are at least 17 dB, and 25 dB below peak in the H-, and E-planes, respectively.

6.4 Multi-beam

In this section, due to the inherent rotational symmetry and focusing property of the proposed structure in the H-plane, we studied multibeam capabilities of the antenna to achieve high gain switchable radiation patterns in different directions in the azimuth plane. Here, the beam switching is developed by utilizing multiple feed elements in which 9-identical elements of integrated waveguide feeds are placed on the focal surface of the lens. Considering the waveguide width, the feed elements are spaced with a center-to-center angular spacing of 7.6° . As shown in Figure 6.1, 9-element integrated waveguide feeds are excited by nine 2.92 mm coaxial connectors identified by F1, F2,..., F9. This enables

launching beams in different desired directions. Figure 6.4 indicates the simulated reflection coefficients for the five feed elements (i.e., F1, F2, F3, F4, F5). As can be seen in Fig. 4 (a) the simulated impedance bandwidths ($|S_{11}| \leq -10$ dB) of 46% is achieved for the antenna covering frequency range of 23.5 GHz to 38 GHz.

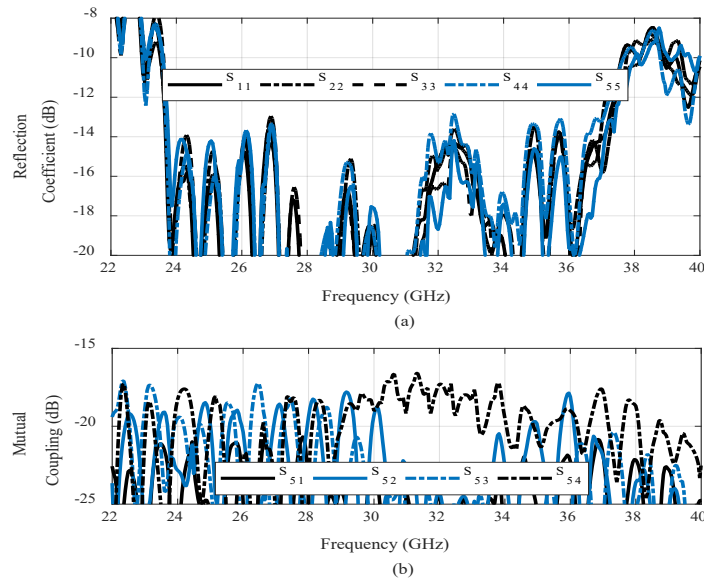


Figure 6.4. Simulated, (a) reflection coefficients of multiple feed elements, (b) mutual coupling between adjacent feeds

Furthermore, the coupling of less than -17 dB is obtained between adjacent feed elements around the center feed (F5). As shown clearly in Figure 6.4 (b), the coupling decreases by distancing from the center feed. Figure 6.5 presents the electrical field distribution in XZ plane, for the two center (F5) and edge (F1) feed elements at 24 GHz and 38 GHz. To demonstrate the performance of the lens, it can be seen that reasonable wave front transformation is obtained through the proposed structure. As shown in Figure 6.5, a cylindrical wave excited at the feed points is transformed into a plane wave on the other side of the lens, which can be realized as directive beams in radiation pattern. Figure 6.6 exhibits simulated beam-switching radiation patterns of the

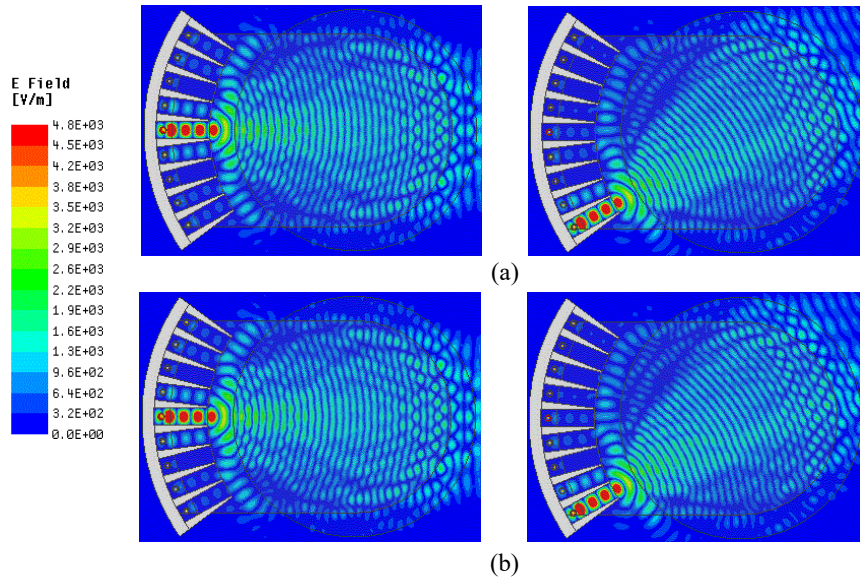


Figure 6.5. Simulated E-field distribution by activating center and edge feeds at (a). 24 GHz, (b). 38 GHz

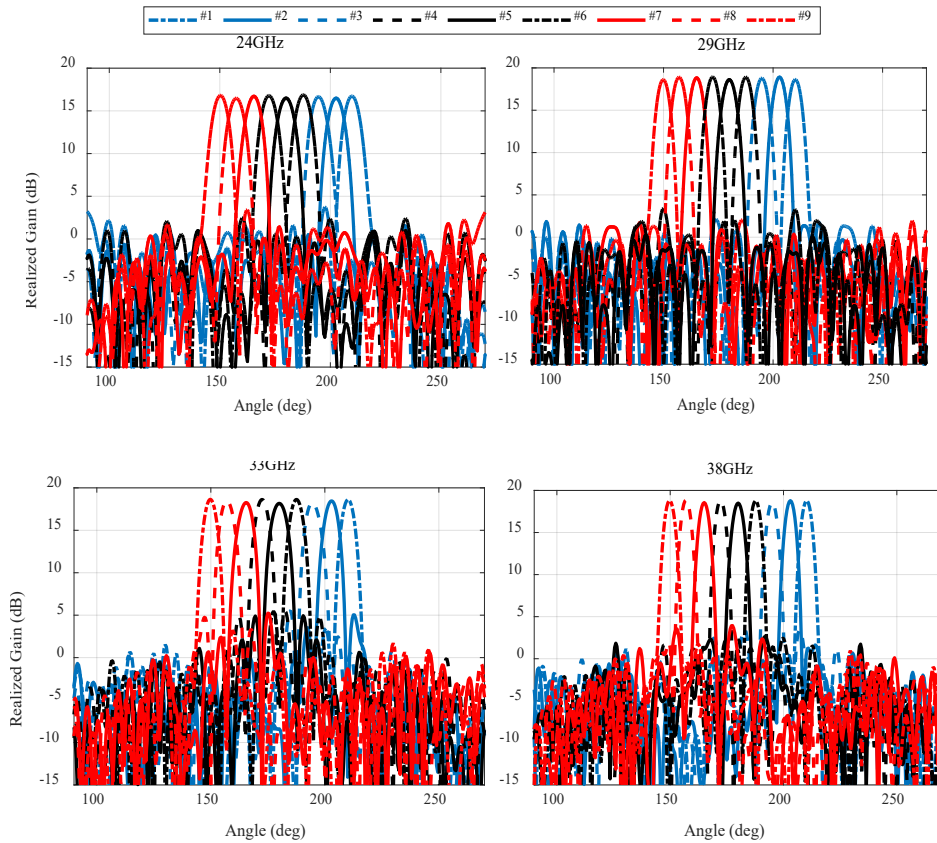


Figure 6.6. Simulated Co-Pol radiation patterns of the antenna at different frequencies for feed elements in the H-plane

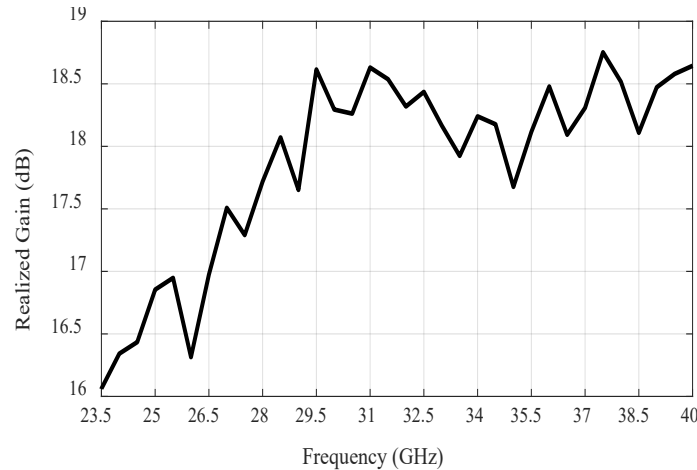


Figure 6.7. Simulated antenna realized gain for center feed.

antenna at different frequencies in the H-plane. As shown, reasonable main beam pattern and sidelobes level are achieved over the entire scanning range in a wide frequency range. The beam directions are designed to be in -30.4° , -22.8° , -15.2° , -7.6° , 0° , 7.6° , 15.2° , 22.8° , and 30.4° in which beam to beam crossover between any two feed elements occur at -3.05 dB level in 24 GHz and -7 dB level in 38 GHz. The sidelobe level remains below -14 dB up to 60.8 scan angle. Comparing the simulated patterns, a gain loss of ± 0.27 dB is achieved as the beam is switched from broadside to 32° . Figure 6.7 shows simulated results of realized gain variation of the antenna for the center feed (F5) over the the entire bandwidth. The Simulated gain of up to 18.7 dBi with a variation of less than 2.7dB is achieved from 23.5 to 38 GHz.

6.5 Experimental Results

To verify the proposed design, a prototype of the antenna is fabricated by using computer numerical control (CNC) milling machine techniques. The prototype of the whole antenna is manufactured in three individual pieces including the metallic bottom and top plates, , and the cylindrical lens. Here, the plates are assembled together with some

screws. The antenna prototype is shown in Figure 6.8. The total size of the antenna is 130 mm \times 119 mm \times 8 mm. Figure 6.9 exhibits the measured frequency characteristics of the manufactured antenna for all ports. The feed elements are assembled according to Figure 6.9, which is composed of a nine 2.92 mm coaxial connectors. The reflection coefficients are measured in which the testing feed element is set active and all other ports terminated by matched loads (50 Ω). As shown in Figure 6.9 (b), reflection coefficients of better than

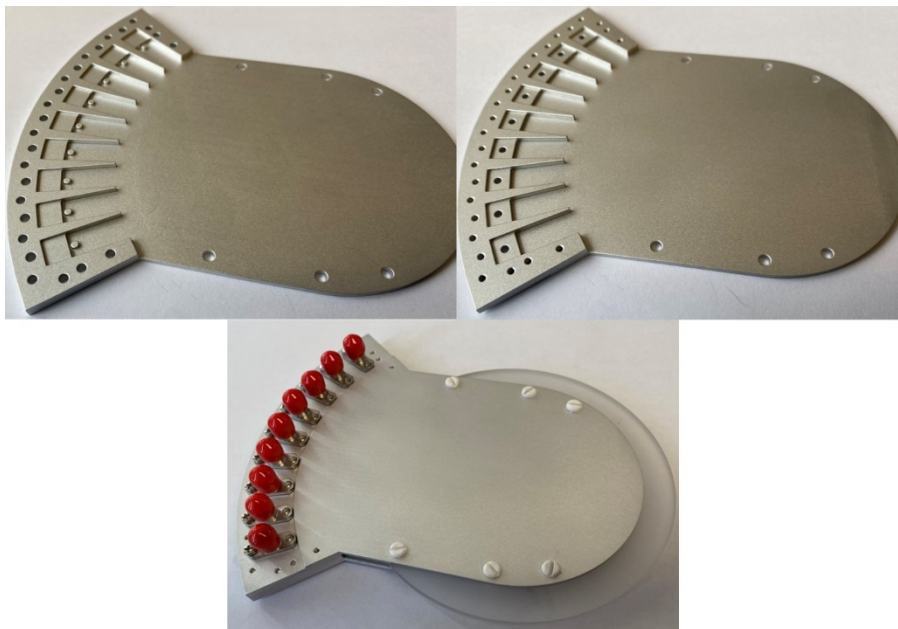


Figure 6.8. Prototype of the proposed multibeam lens antenna

-10 dB are achieved for all ports over a wide bandwidth from 24 GHz to 40 GHz, and the coupling coefficients lower than -18 dB are obtained between adjacent ports (Figure 6.9 (c)). The antenna radiation pattern is measured in an anechoic chamber at the University of Colorado Boulder, USA (see Figure 6.10). Figure 6.11 shows the measured normalized H-plane radiation patterns for the nine-feed elements. To measure multiple radiation pattern from each port, the measurement is done by simply switching between the feed elements, and loading other ports with a 50-ohm terminator. As a result, reasonable main

beam pattern and sidelobes level are achieved over a wide frequency range. The beam directions are measured in -33° , -24° , -16° , -8° , 0° , 8° , 16° , 24° , and 33° . The sidelobe level remains below -14 dB as the beam is switched from broadside to 33° . The measured results show that the beams overlap level varies from -4 dB to -4.8 dB between adjacent patterns

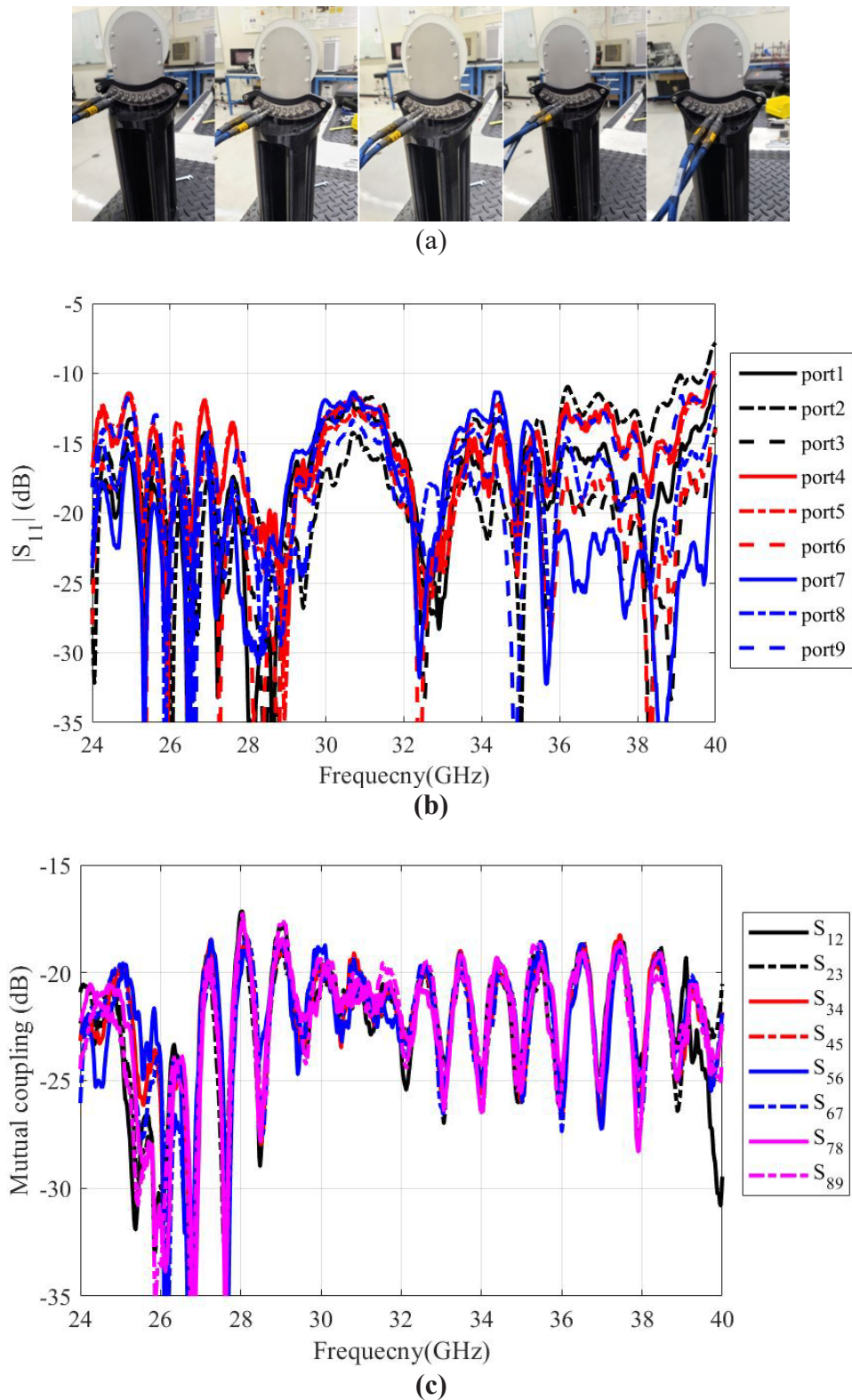


Figure 6.9. The measured frequency response of the antenna, (a), measurement setup (b) input reflection coefficient for all ports and, (c). port coupling coefficients between adjacent ports of the fabricated prototype.



Figure 6.10. Fabricated antenna setup in an anechoic chamber

6.6 Conclusion

In this paper, a wideband high gain PPW Luneburg-based lens antenna with beam switching capabilities is designed, simulated and fabricated operating over a wide frequency range at Ka-band. By switching among different integrated feed elements in the two parallel plates, the antenna achieves a scan coverage of $\pm 33^\circ$. The proposed antenna offers the advantages of flexible design, low cost and easy integration, which can be implemented for 5G point-to-multipoint communication applications, and automotive radar systems.

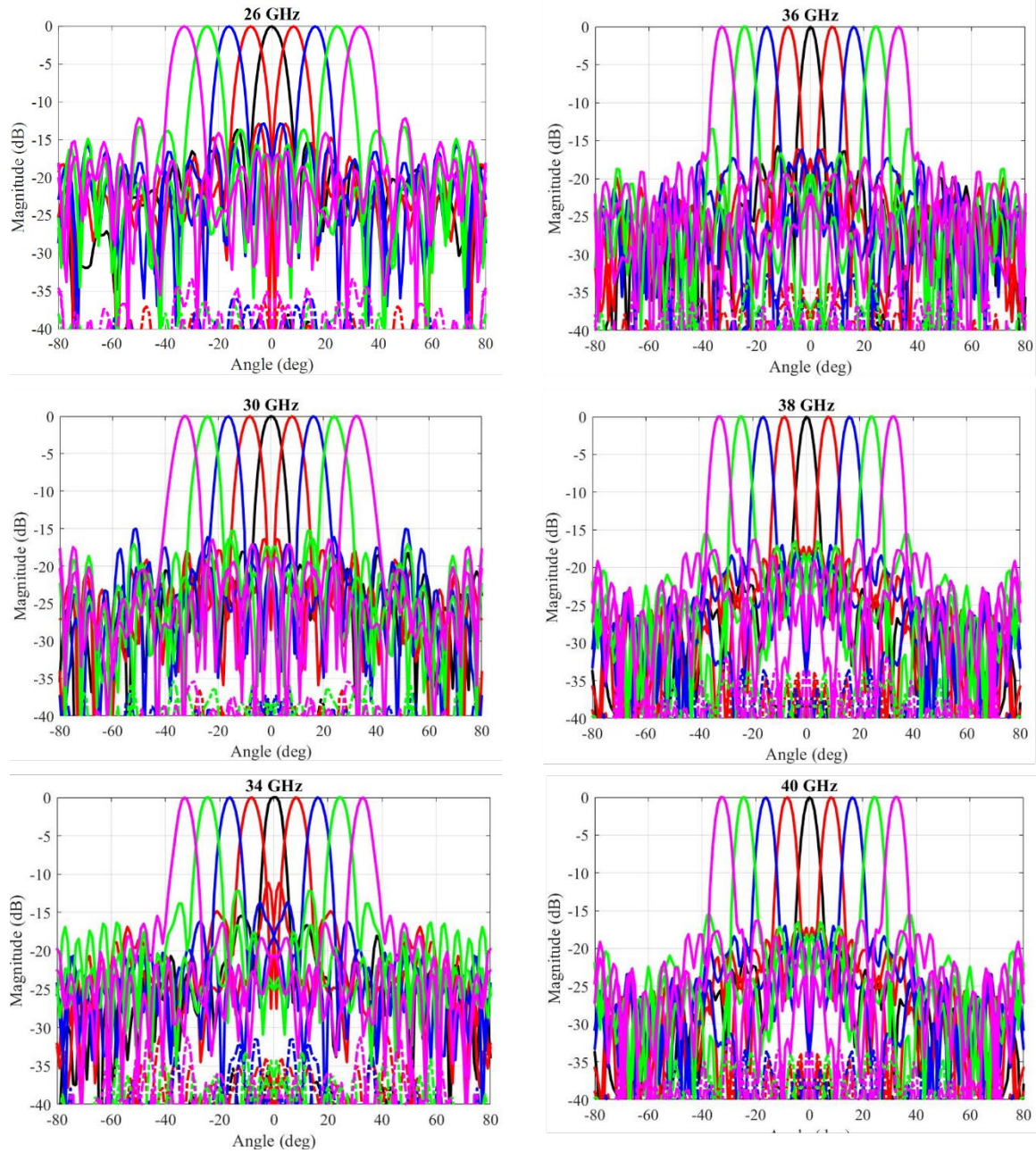


Figure 6.11. The measured H-plane radiation patterns of the fabricated PPW LL antenna at Ka-band.

CHAPTER SEVEN: WIDEBAND METALLIC CYLINDRICAL LENS ANTENNA

7.1 Introduction

The Luneburg lens, as a rotationally symmetric GRIN lens, has an advantage in supporting high gain wide-angle beamsteering. The ideal Luneburg lens should be composed of a dielectric material with a continuously graded refractive index. As presented in previous chapters, the GRIN property of the lens can be approximately obtained by PPW partially filled with dielectric material [70], [113], [116], drilled and pressed foam material [116], or PPW with gradual height [101]. Besides, with the development of transformation-optics theory, using the artificial electromagnetic materials based on metasurface technology has been frequently used in the design of Luneburg lens antennas [114], [117]–[119]. In this technology, the artificial electromagnetic materials are developed based on periodic structures [117], [120]–[124]. The diversity of the artificial electromagnetic materials brought more flexibility to the design and realization of Luneburg lens antennas. The artificial materials were often constructed with unit cells smaller than the wavelength and arranged in a periodic structure. In this periodic structure, for Luneburg lens applications, a grade index feature is achievable by modifying the dimensions of unit cells. For example, the periodic structures can be realized by drilling holes in the dielectric substrates [117], [120], printing patches in the dielectric substrates [121]–[123], and printing three dimensional (3-D) structure using the polymer jetting technique [124]. In [122], a planar Luneburg lens is proposed with an array of circular patches on a substrate. Changing the patch size can modify the effective refractive index of the antenna. The lens

is assumed to support transverse magnetic (TM) modes that will produce reflections at the air interface. However, these type of antennas have some drawbacks. First, dense dielectrics, which are generally lossy, are required to realize the profile of lens antennas. In addition, the dense dielectric profiles result in multiple reflections in the lens, degrading their radiation properties.

In order to overcome the problem associated with the loss of dielectric in lens antennas, fully metallic lens antennas can be employed. In 1946 fully metallic lenses were constructed with artificial materials [125]. In recent years [99] a wideband geodesic Luneburg lens with full metallic profile was proposed for the first time. In this lens, the refractive-index variation is realized with geodesic surfaces. In the implementation of these lenses, there is no requirement for dielectric materials or metamaterials; therefore, these lenses are generally broadband and have low-losses. However, their profile can be much thicker than the metasurface based Luneburg lenses. In another work, using a bed of metallic posts or holes to realize the permittivity profile of a Luneburg lens was proposed for the first time in 1960 [102]. The method proposed in that work adheres to the class of metasurfaces; as mentioned above, employing metasurfaces facilitated the fabrication process, enabling the realization of the lenses in a cheap and compact way. The losses mainly depend on the medium in which the wave propagates. Since then, several works were accomplished to realize the GRIN profile of Luneburg lens based on a fully metallic structure. In [126] a Luneburg lens created with two glide-symmetric metasurfaces was proposed with an operating frequency between 4-18 GHz. A similar design is presented in [114] that was experimentally tested in the PPW technology. The top and bottom plates of PPW are loaded with metallic posts of different heights and holes of different depths to

realize the required GRIN property of the LL. In these works, the operating bandwidth of the lens depends on the dispersion nature of the selected unit cell. In [104], the required refractive indices are obtained by changing the height of metallic post while they suffer the serious dispersion and narrow bandwidth.

In this chapter, an air-filled PPW lens antenna has been analyzed to introduce a new design of a fully metallic lens antenna. The theoretical basis for the analysis is presented, and design data are provided by means of parametric studies in which a periodic structure of metallic posts with equal heights provided wide bandwidth performance at Ka-band.

7.2 Electromagnetic waves in Periodic structures

Periodic structures consist of an infinite number of repeated elements in one, two or three dimensions. This repeated element is known as the unit cell. It is the building block of the periodic structures. Similar to crystal structures, we define the unit cell in terms of the lattice (set of identical points). In three dimensions the unit cell is any parallelepiped whose vertices are lattice points, in two dimensions it is any parallelogram whose vertices are lattice points. In general, the unit cell is chosen such that it is the smallest unit cell that reflects the symmetry of the structure. There are two distinct types of unit cell: **primitive** and **non-primitive** (see Figure 7.1). Primitive unit cells contain only one lattice point, which is made up from the lattice points at each of the corners. Non-primitive unit cells contain additional lattice points, either on a face of the unit cell or within the unit cell, and so have more than one lattice point per unit cell. In our case, we will have a square lattice depicted in Figure 7.2, where the distance from one lattice point to another, which is the length of one side of the unit cell is p .

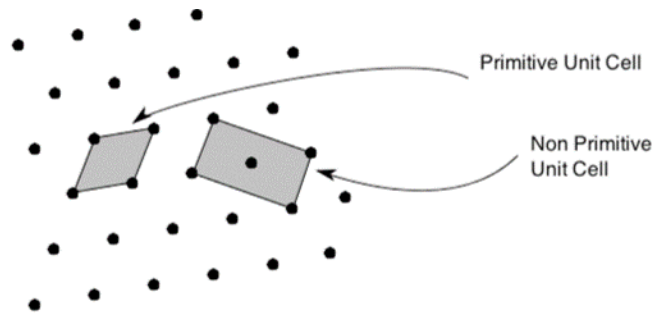


Figure 7.1. Primitive unit cell

In order to investigate electromagnetic waves inside a periodic structure, its dispersion relation should be studied. The dispersion relation is a relation between the frequency and propagation constants of different modes, and it is plotted in the dispersion diagram. Since the dispersion diagram of periodic structures is periodic, it is sufficient to study the dispersion in the smallest repeatable region, which is called the Brillouin zone. The Brillouin zone is the most fundamental region for defining the propagation vector for a unit-cell; basically if one can define all the propagation vectors in the Brillouin zone, one obtains the entire characteristic of the entire periodic structure.

To have a better understanding of the Brillouin zone we have to first understand the direct lattice vectors and reciprocal lattice vectors, because periodic structures are often analyzed on the reciprocal lattice instead of the direct lattice. Figure 7.2 and Figure 7.3 represent the physical and real (direct lattice vectors) and reciprocal or k-space vectors for a two dimensional periodic structure. As can be seen in Figure 7.2, for the presented square lattice, the primitive translation vectors just point along the edge of the unit cell, we have direct lattice vectors t_1 and t_2 in terms of lattice spacing. In order to define Brillouin zone in the reciprocal space, as shown in Figure 7.4, we consider a highlighted region. This highlighted area is called the Brillouin zone. The Brillouin zone is simply the primitive unit cell in reciprocal space. As shown in Figure 7.3, typically the unit cell is centered

around zero. For the given Brillouin zone there is usually additional symmetry that can be exploited to reduce the Brillouin zone down to even a smaller region from which we can analyze the lattice. The first thing is up and down symmetry. If the lattice has an additional symmetry, there will be irreducible Brillouin zone. Actually because of the up-down symmetry we can restrict it to either the top or the bottom (see Figure 7.3 (a)). The second symmetry is left-right symmetry that means the left and the right halves of Brillouin zone will be mirror images of each other then we can restrict our calculation to just one quadrant (see Figure 7.3 (b)). There can be even more symmetry which is 90 degree rotational symmetry. If we rotate the unit cell 90 degree, it has 90 degree rotational symmetry so that means irreducible Brillouin zone reduces down to a half triangle (see Figure 7.3 (c)). This irreducible Brillouin zone greatly reduces numerical analysis for lattices. For numerical analysis, the smallest possible volume is desired because this minimizes the volume of space that is analyzed.

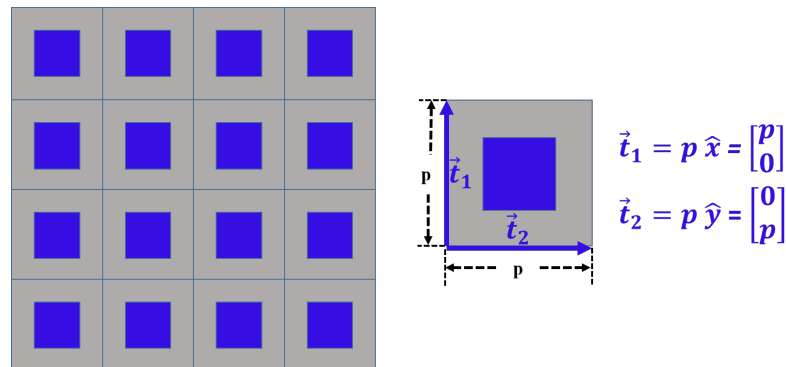


Figure 7.2. Periodic array of unit cell and direct lattice vectors in x and y direction

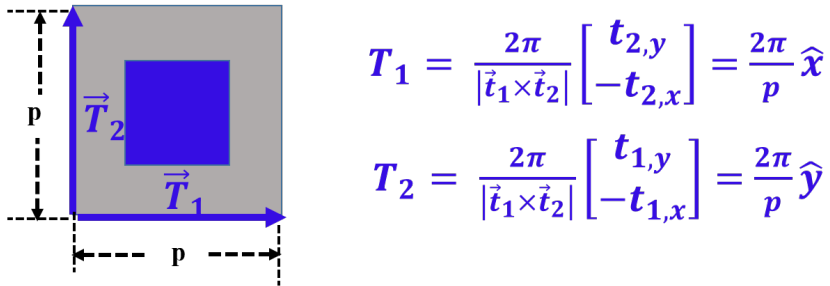


Figure 7.3. Reciprocal lattice vectors

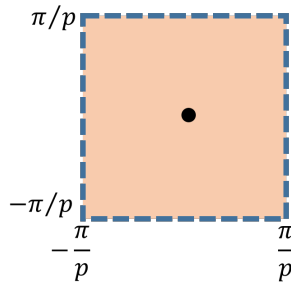


Figure 7.4. Brillouin zone; the primitive unit cell in reciprocal space

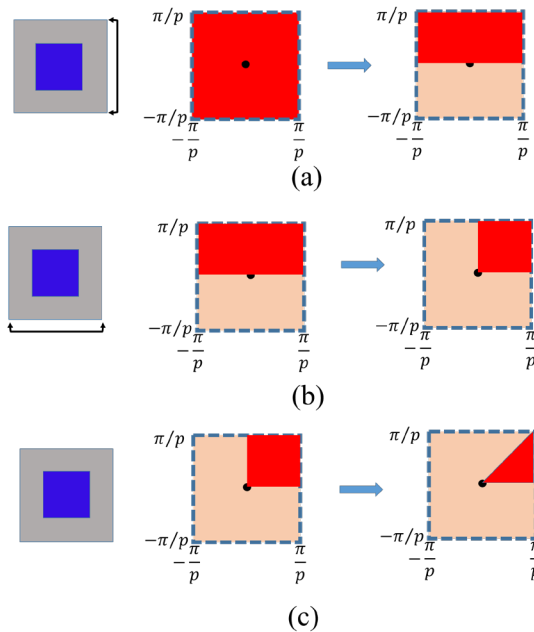


Figure 7.5. Irreducible Brillouin Zone; Brillouin zone symmetry in (a). up/down, (b). left/right, (c). 90-degree rotational symmetry.

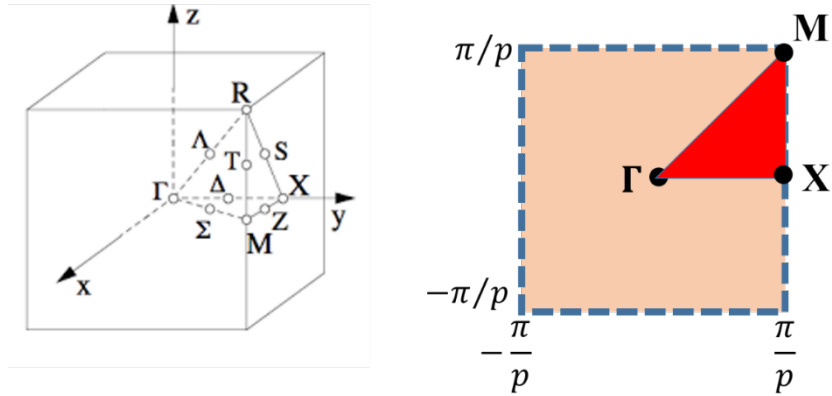


Figure 7.6. Key points of symmetry on Brillouin zone

The field inside a periodic structure takes on the same symmetry and periodicity of that structure according to the Bloch theorem.

$$\vec{E}(\vec{r}) = \vec{A}(\vec{r})e^{j\vec{\beta}\cdot\vec{r}} \quad (7.1)$$

Given the lattice translation vectors, we can mathematically define the periodicity:

$$\vec{A}(\vec{r} + \vec{t}) = \vec{A}(\vec{r}) \quad \vec{t} \equiv \text{lattice vector.}$$

Starting from Maxwell curl equations for non-magnetic materials:

$$\nabla \times \vec{E} = -j\omega\mu_0\vec{H} \quad (7.2)$$

$$\nabla \times \vec{H} = j\omega\varepsilon_0\varepsilon_r\vec{E} \quad (7.3)$$

We can derive the wave equation for the magnetic field \vec{H} by taking the curl of the Equation 7.3 above and substituting in the Equation 7.2.

$$\Delta \times \frac{1}{\varepsilon_r} \nabla \times \vec{H} = k_0^2\vec{H} \quad (7.4)$$

According to Bloch theorem in Equation 7.1, the magnetic field is periodic as follows:

$$\vec{H}(\vec{r}) = \vec{H}_{\vec{\beta}}(\vec{r}).e^{j\vec{\beta}\cdot\vec{r}} \quad (7.5)$$

Substituting this into the wave equation lead to:

$$(\Delta + j\vec{\beta}) \times \frac{1}{\epsilon_r} (\Delta + j\vec{\beta}) \times \vec{H}_{\vec{\beta}} = \left(\frac{\omega_{\vec{\beta}}}{c_0}\right)^2 \vec{H}_{\vec{\beta}} \quad (7.6)$$

The wave equation derived in Equation 7.6 is an eigenvalue problem that in general can be presented in the form of Equation 7.7 in which L is a linear operation of cross product operating on the magnetic field, and in the right-hand of Equation 7.7 we have a scalar constant times that magnetic field.

$$L \{ \vec{H}_{\vec{\beta}} \} = \nu \vec{H}_{\vec{\beta}} \quad (7.7)$$

Eigen-value problems have discrete solutions (like modes in a waveguide) that are all orthogonal (very different from each other). This means that electromagnetic waves in periodic structure only exists as discrete modes. Fields can only exist as integer combinations of the eigen-modes, or Bloch modes, of the lattice.

$$\vec{H} = \sum_{\vec{\beta}} a_{\vec{\beta}} \vec{H}_{\vec{\beta}} \quad (7.8)$$

Based on equation (7.8), any magnetic field is any field combination of those eigen modes

7.3 Unit Cell of Periodic Structures

A metasurface structure of a Luneburg lens is composed of periodic unit cells that can be studied based on the electromagnetic performance of the unit cell. To start off we need to study the Brillouin dispersion diagram of the unit cell. A dispersion diagram is a plot of propagation constant versus frequency; a dispersion diagram basically tells how much phase shift a material has at a given frequency.

The dispersion diagram is one of the most interesting properties for metasurface structures which can be obtained in ANSYS HFSS or CST Microwave Studio Suite with the Eigenmode solver. The boundary conditions in the metasurface plane are periodic,

where we can set the phase shift in both x - and y - directions between adjacent unit cells, and the boundary condition on top and bottom is a perfect electrical conductor (PEC) in the z -direction, which creates an infinite array of the unit cells. With the eigenmode solver, all eigenvalues in the structure can be found, and each eigenvalue corresponds to a mode. Each mode has its own phase velocity, group velocity and field distribution. The field distribution along the unit cells is periodic with a phase delay between the unit cells, and the phase delay can be obtained with the phase constant β and the unit cell's periodicity p . When solving the eigenvalue equation in a periodic structure only a finite area in the Fourier space called the irreducible Brillouin zone has to be considered and all eigenvalues can be found along the contour of the irreducible Brillouin zone [127].

7.4 Effective Refractive Index

For a free space wave with frequency ω_0 , the wave number k_0 is:

$$k_0 = \frac{2\pi}{\lambda_0} = \frac{\omega_0}{c} \quad (7.6)$$

For surface waves impinging on a periodic structure, wave propagation cannot be investigated with plane wave response, but with dispersion relation of this surface. For a 2D-periodic structure, in a full period of $d_x = d_y = p$, the phase shift is 2π . Hence inside one period, from Γ to X , the x - direction phase variation (*phaseX*) is from 0 to π , while y -direction phase (*phaseY*) stays 0. Thus, wave number k (also the propagation constant β) follows a frequency dispersion relation in Equation 7.7. In HFSS, the phase shift is changed along the irreducible Brillouin zone boundary and frequencies of eigenmodes are obtained accordingly.

$$k(\omega).p = 0 \text{ to } \pi \quad (7.7)$$

At different frequencies, the effective refractive indices n_{eff} are obtained by the ratio of k and k_0 .

$$n_{eff} = \frac{c}{v} = \frac{\omega/k_0}{\omega/k} = \frac{k}{k_0} \quad (7.8)$$

7.5 Unit Cell Design

There are three main considerations in designing a proper unit cell for Luneburg lens applications:

- Sufficient refractive index for a Luneburg lens law. That means the unit cell must provide required effective refractive index.
- Small frequency dispersion. We would like a wide band antenna, hence the n_{eff} versus frequency curve should be as flat as possible.
- Achieving the easiest manufacturing process with the designed unit cell.

To design the metallic Luneburg based lens antenna for the aiming goals, metallic square pin-unit cells are studied in this work (see Figure 7.3). It consists of two square metallic sheets of size $p \times p \text{ mm}^2$ loaded with a metallic square pin of size $a \times a \text{ mm}^2$ at their center. The top metallic sheet is placed with a space of g over the top of the square pin.

As mentioned above, in order to generate the dispersion diagram for the unit cell, first we must configure HFSS to use its Eigenmode solve, HFSS>Solution Type...>Eigenmode. Since the unit cell is a 2D-periodic structure in x and y directions, periodic boundary conditions (Master –Slave) are assigned in both directions. Then the phase delay of Phase_X and Phase_Y is applied to study the high-symmetry points of the irreducible Brillouin zone (ΓX , XM , $M\Gamma$). As shown in Figure 7.8, in ΓX region, in the x -

direction ($\beta_x p$), Phase_x variable is stepped from 0 to π while phase variation in y -direction (Phase_Y) is set to 0. For the XM region, Phase_Y is stepped from 0 to π while Phase_X is set to 0. For the $M\Gamma$, both Phase_X and Phase_Y are equal and are stepped from π to 0.

In our case, the unit cell is isotropic in the x - and y -direction and the dispersion behavior is assumed to be identical in these directions. The $M\Gamma$ region had a similar dispersion behavior as the ΓX and XM for the first mode. Therefore, the ΓX region is only considered for dispersion diagram analysis. Then, parametric sweep study is added for variable Phase_X from 0 deg to 180 deg with 15 deg steps going from Γ to X.

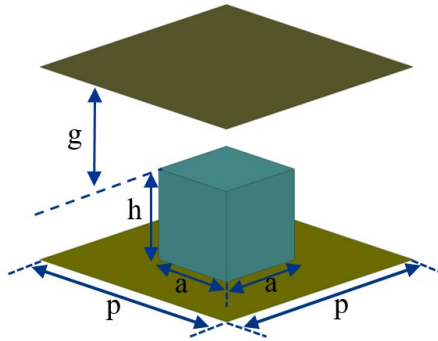


Figure 7.7. A typical unit cell in periodic metasurface.

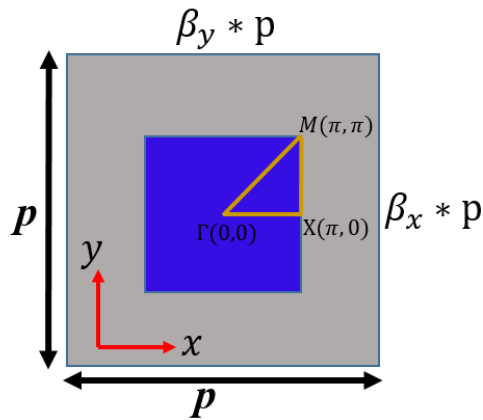


Figure 7.8. The irreducible Brillouin zone for the proposed unit cell in HFSS.

The effective refractive index n_{eff} is the parameter of interest when studying the unit cell. From the Eigenmode solver, the propagation constant (β) can be obtained from the phase variation in the irreducible Brillouin zone. In our case, phase variation from 0 to π is applied along the Γ to X region. In HFSS Eigenmode solver, the phase variation is applied and then frequencies of Eigenmodes are obtained accordingly, where the $\beta(\omega) \times p = \text{Phase_X}$ variation from 0 to π wherein p is the periodicity of the unit cell. Based on this dispersion at different frequencies, the effective refractive indices n_{eff} are

obtained by the ratio of k and k_0 , ($n_{eff} = \frac{c}{v} = \frac{\omega/k_0}{\omega/\beta} = \frac{\beta}{k_0}$).

After a parametric study of the dimensions of the unit cell, we have chosen the unit cell parameters with height of $h = 0.8 \text{ mm}$, periodicity of $p = 1.4 \text{ mm}$, dimension of $a = 0.8 \text{ mm}$ and air gap of $g = 0.3 \text{ mm}$. The unit cell size, periodicity, and height controls the refractive index. It can be seen that, the height (h) has the most significant impact on the refractive index. Figure 7.9 depicts n_{eff} as a function of frequency when h is varied from 0 to 2 mm. The refractive index increases with increasing h and n_{eff} varied between 1.3 to 1.4 when h is around 0.3 mm. Another important parameter is the gap of g . Figure 7.10 depicts the relation between g and n_{eff} and it shows that when g increase n_{eff} decrease.

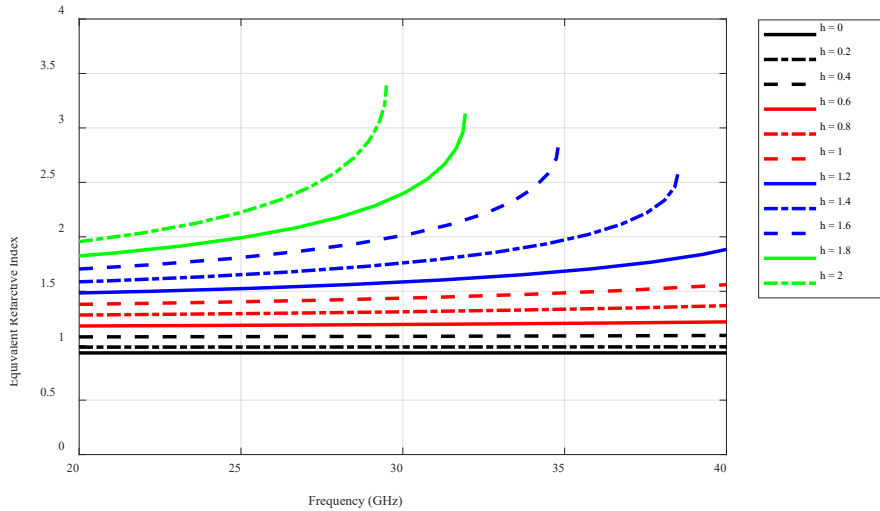


Figure 7.9. Effective refractive index for a square pin-unit cell when h is varied. The other parameters are $p = 1.4$ mm, $g = 0.3$ mm, $a = 0.8$ mm.

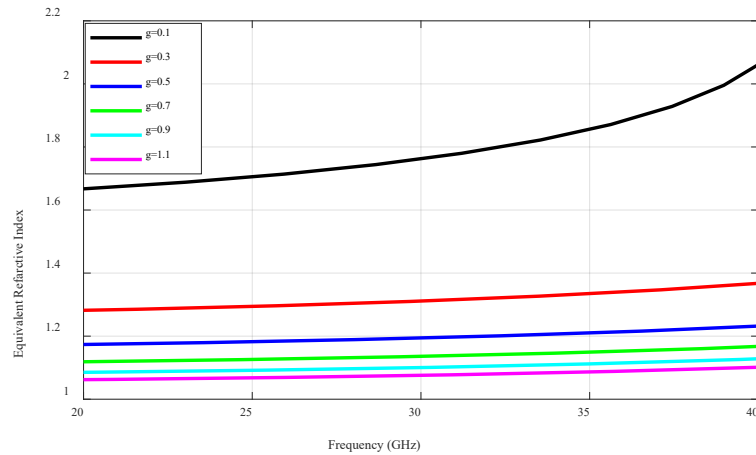


Figure 7.10. Effective refractive index for a square unit cell when g is varied and $p = 1.4$ mm, $a = 1.4$ mm, $h = 0.8$ mm.

Figure 7.11 presents the effective refractive index variation of the designed unit cell over the wide frequency range at Ka-band, where it has almost constant value.

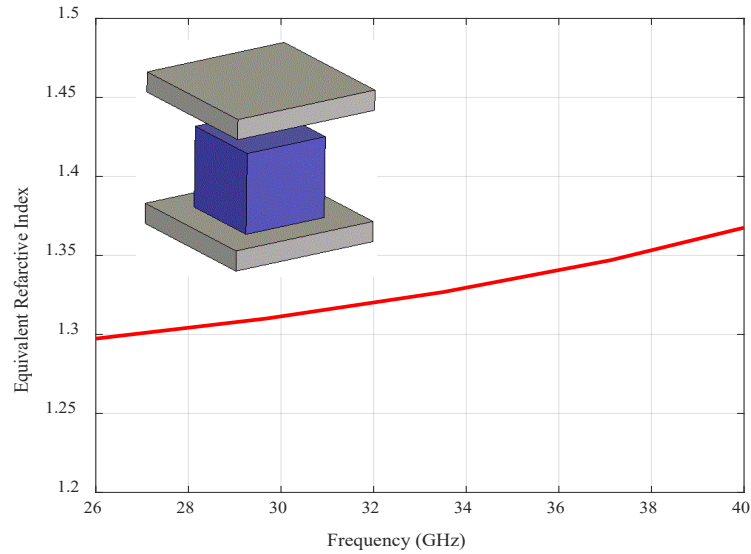


Figure 7.11. Effective refractive index for the proposed unit cell, where $a = 0.8$ mm, $h = 0.8$ mm, $p = 1.4$ mm, $g = 0.3$.

7.6 Lens Design

In this section, a full metal cylindrical Luneburg lens is designed which is based on an array of periodic square pins. We utilized the parallel plate technology to design a simple fully metallic lens antenna. In general, a cylindrical lens based on parallel plate technology is composed of two sheets of metal where there could be any kind of dielectric and material between those plates providing the GRIN property of the lens.

In this design, in order to realize the gradient index (GRIN) profile corresponding to the Luneburg lens, the bottom plate of the parallel plates is loaded with a periodic array of metallic pins. Here, a simple array of metallic square pins with the same heights emulate the continuous refractive index variation needed to design a cylindrical lens over a wide frequency range at Ka-band. The geometry of the antenna is shown in Figure 7.12. As can be seen in Figure 7.12 (a), the antenna composed of three main parts: the top plate, the bottom plate, and the feed element. As shown, the bottom plate of the PPW is designed based on an array of periodic structure of square pins.

As can be observed in Figure 7.12 (c) for the top plate, the top plate of the parallel plate is designed based on an exponential tapering instead of a flat plate. This exponential profile operates as the radiation aperture of the antenna. Moreover, it solves mismatch problems on the interface between the antenna aperture and free space. It provided better transition to free space. In this way, with the objective of efficient radiation and impedance matching geometrical parameters of the top plate is optimized in the frequency range of the Ka-band (26 – 40 GHz). As seen in Figure 7.13, half of the antenna is enclosed with side walls to additionally prevent field leakage on the sides of the antenna. This enclosure slightly disturbs the lens effect because the vertical electric field at the edges is forced to zero due to the metallic walls [122]. However, by enclosing only a part of the antenna and by leaving the second half with open sides, the performance of the antenna is only minimally disrupted. For this lens the overall width is 66 mm (W in Figure 7.13), and structure height is 8.7mm ($h_b + h_t + h_0 - g$ in Figure 7.13). Further, the maximum distance between the two plates is set to be $h_0 = 4.356 \text{ mm}$ which is less than $\frac{\lambda_0}{2}$ at 30 GHz at the end of the radiation aperture of the antenna.

In order to excite the lens, a simple rectangular waveguide is implemented between two plates excited with a 2.92 mm connector and placed at the edge of the lens. Based on the required frequency range the waveguide dimension is selected to be 3.556mm (height) \times 7mm (width) to operate at frequency range from 26 GHz to 40 GHz. This dimension corresponds to a standard WR28 rectangular waveguide. It is important to mention that here, considering the height of the waveguide $h_b = 3.556 \text{ mm}$, we do not need to use any cascaded or kind of tapering feature to transform the height of the waveguide to the height of the radiation part of the antenna. Because, as can see in Figure

7.13, in the radiation side, a top plate with an exponential shape starts from $h_b = 3.556 \text{ mm}$ on the left side, and again ended to the same height on the right side.

For impedance matching consideration, a small matching part is placed behind the edge of the lens which is integrated into the bottom plate. This back part is $\frac{\lambda}{4}$ (λ is wavelength at 30 GHz) away from the edge of the lens and is shown with l_m parameter in Figure 7.13. The dimension of this part significantly improves the frequency response of the antenna. In comparison to previous wideband cylindrical Luneburg lens antennas[114]-[115], this simple and compact feeding part make the antenna design and fabrication much easier. Actually, by comparison against the previous wideband feeds with multi-stepped configuration in [115] the proposed simple and integrated feed element without adding extra complexity to the antenna structure enhances the bandwidth of the feed element, which in practice, it can be simply and cost-effectively implemented.

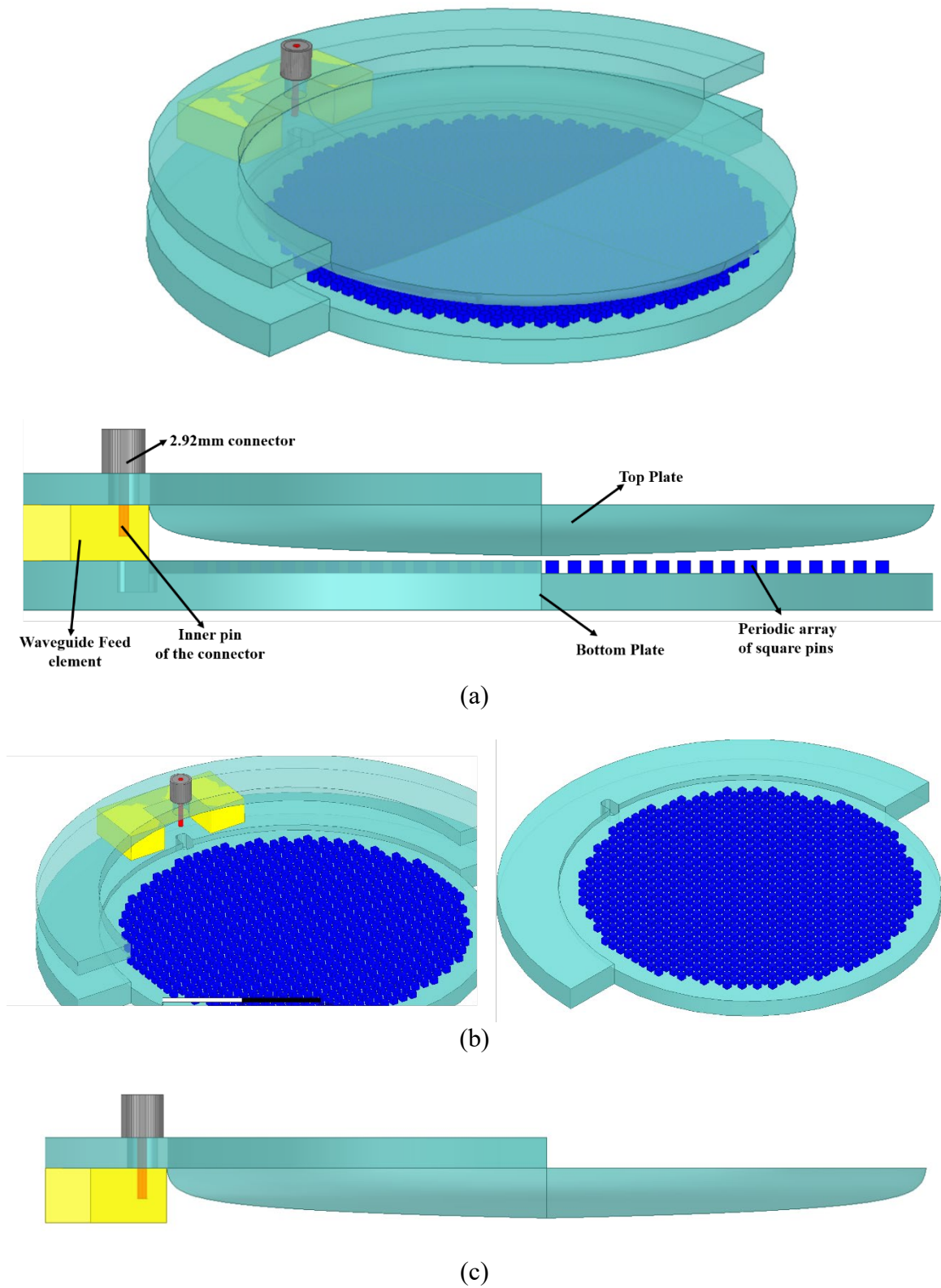


Figure 7.12. The full metal cylindrical Luneburg Lens Antenna configuration with top and bottom plates.

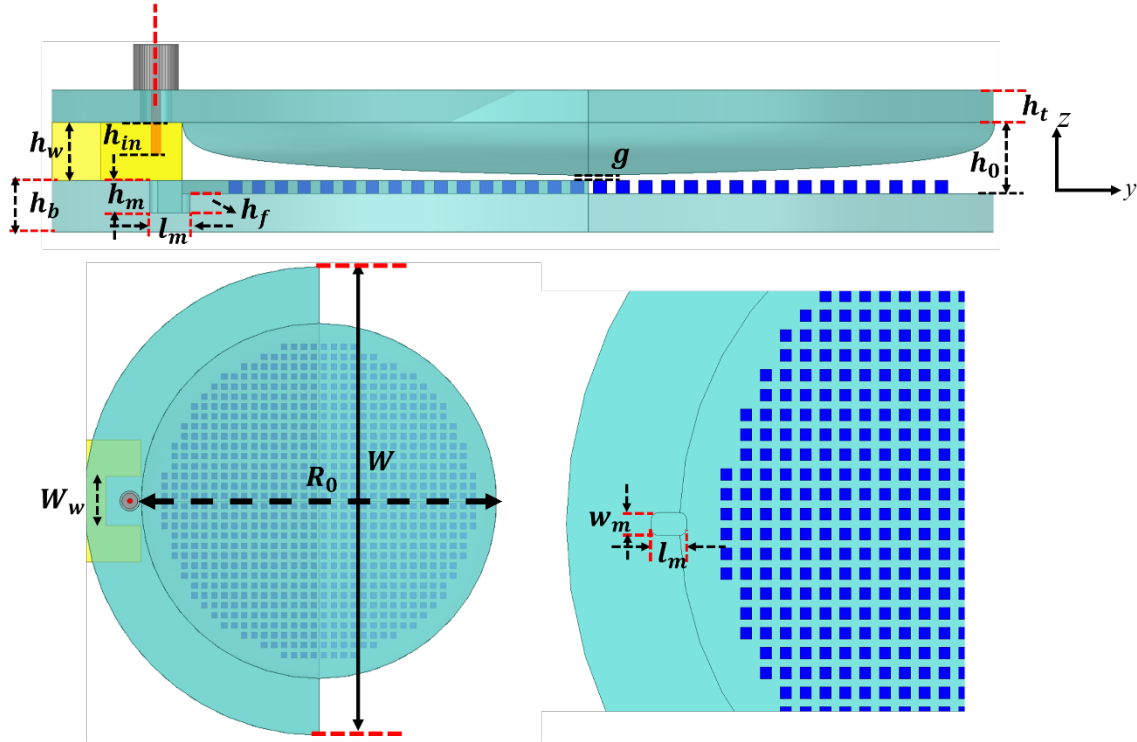


Figure 7.13. Description of antenna parameters. $W = 66\text{mm}$, $R_0 = 50\text{mm}$, $h_0 = 4.4\text{mm}$, $h_t = 2\text{mm}$, $h_b = 3.15\text{mm}$, $g = 0.3\text{mm}$, $W_w = 7\text{mm}$, $h_w = 3.55\text{mm}$, $h_{in} = 2\text{mm}$, $h_m = 2\text{mm}$, $h_f = 1.2\text{mm}$, $w_m = 1.6\text{mm}$, $l_m = 2.5\text{mm}$, h_0

The model of the antenna (see Figure 7.12 (a)) with a single feed integration is modeled in HFSS and antenna parameters are analyzed and optimized to control the bandwidth characteristics and radiation pattern of the antenna. Full wave simulations of the single feed are performed at frequency range from 26 to 40 GHz. The optimized values of antenna parameters are listed in the caption of Figure 7.13. Figure 7.14 presents the simulated reflection coefficient of the antenna over a wide frequency range. The -10 dB reflection coefficient is achieved within the operating band from 26.5 GHz to 39 GHz. As can be noticed, the antenna has a matching level lower than -15.0 dB in the targeted bandwidth from 27GHz to 38 GHz bandwidth.

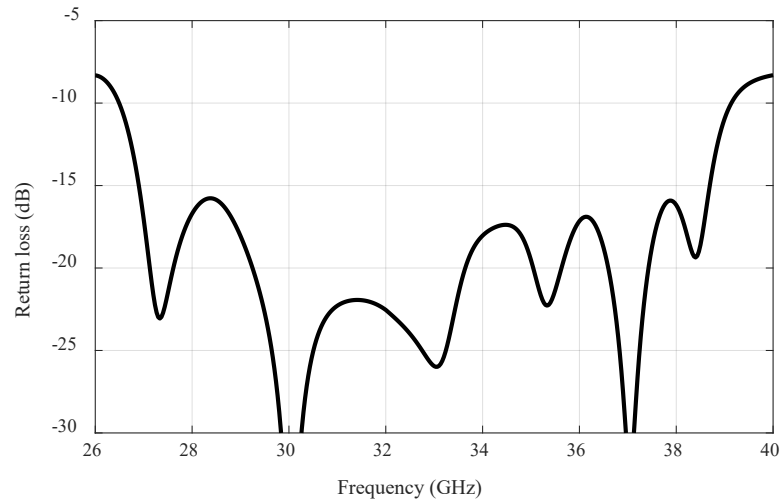
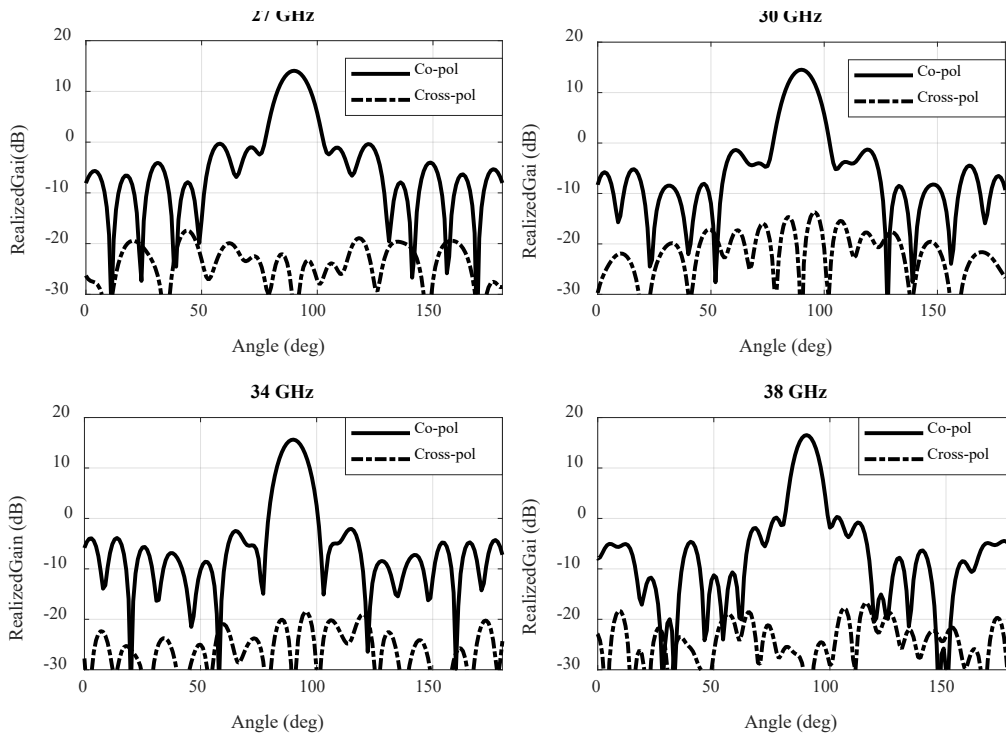
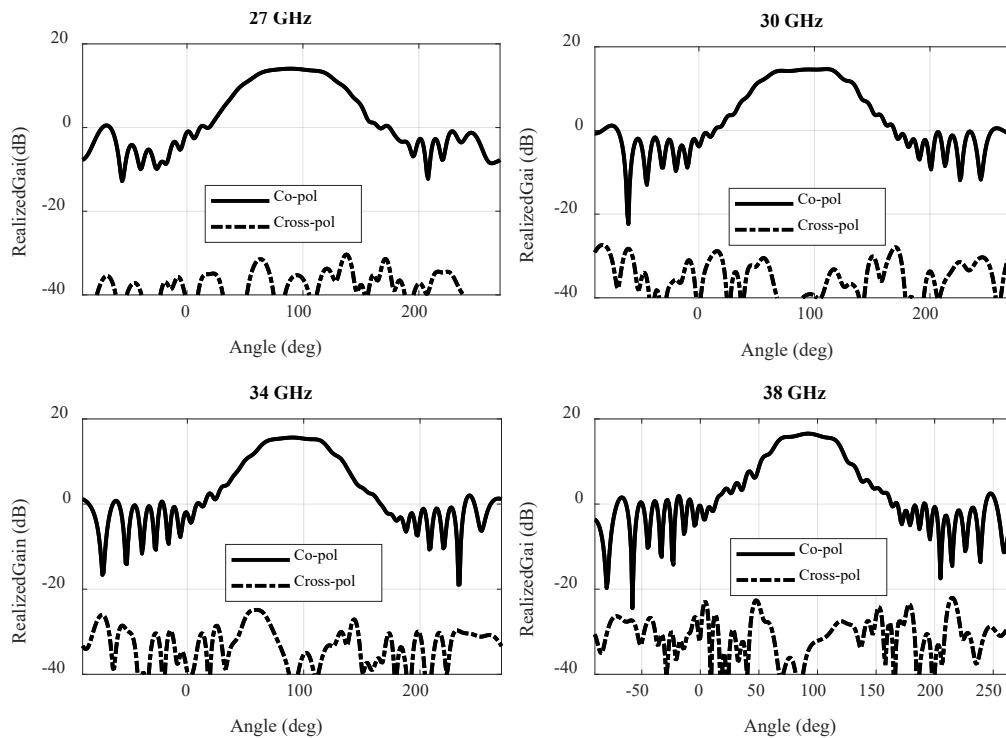


Figure 7.14. Simulated reflection coefficients of the antenna

The simulated E and H-plane patterns for the optimum value of feed parameters and the exponential profile of the top plate are shown in Figure 7.15. It can be observed that the proposed Exponential profile results in excellent E- and H-plane patterns over the wide bandwidth from 27 GHz to 38 GHz. The half-power bandwidths (-3 dB) of YZ-plane (E-plane) and XY-plane (H-plane) vary from 90° to 55.4° , and 14.97° to 9.17° , over the operating band from 26 GHz to 38 GHz, respectively. This corresponds to sidelobe levels below -19 dB in the H-plane and less than -20 dB in the E-plane. Furthermore, the cross polarization levels are at least 20 dB, and 30 dB below peak in the H-, and E-planes, respectively. Figure 7.15 present the three dimensional (3D) radiation pattern of the antenna at 30 GHz. Figure 7.1 (b), (c) depicts antenna pattern in the vertical and azimuth planes, respectively. The antenna has a fan-beam radiation pattern in which the half-power beam width (HPBW) of the pattern in the narrow plane (XY-plane, H-plane) is 12.6 degree at 30 GHz.



(a)



(b)

Figure 7.15. Antenna radiation pattern in different frequencies at : (a) H-plane, (b) E-plane

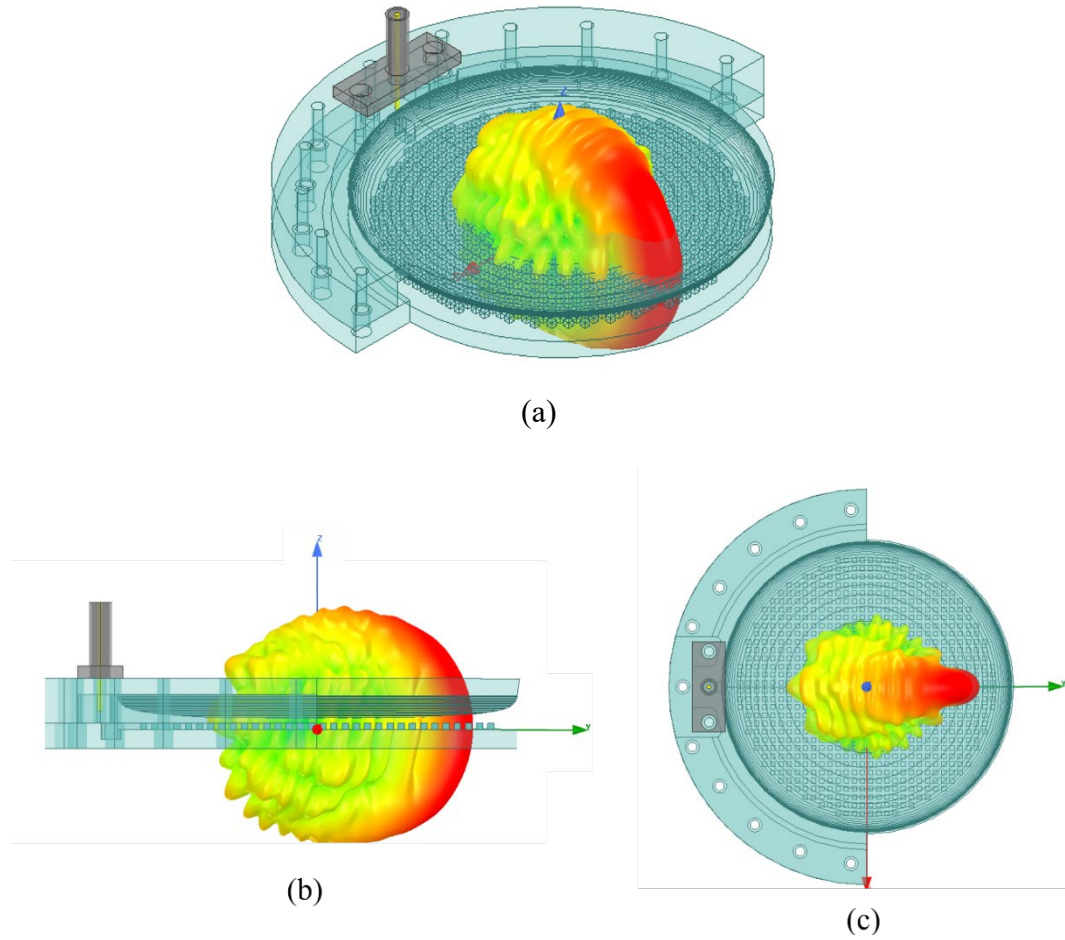


Figure 7.16. (a) 3D radiation pattern of antenna at 30GHz, (b). Pattern of E-plane (YZ plane), (c). Pattern of H-plane (XY Plane)

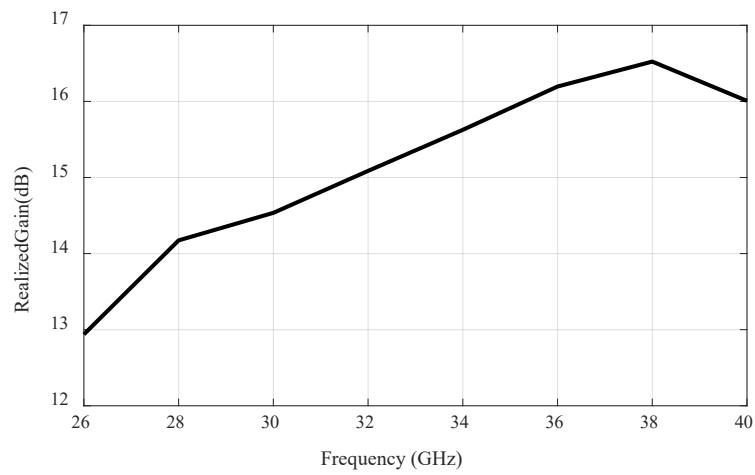


Figure 7.17. Realized Gain of the proposed antenna

7.7 Measurement results

To verify the proposed design, a prototype of the antenna was manufactured by using computer numerical 3-axis CNC control milling in aluminum. The fabrication Tolerances of +/- 0.005inch (0.13mm) is expected in this machining process. To consider the effect of the wire all the corners in our design are converted to round edges with a radius of 0.125 mm. The antenna is fabricated with two plates and then assembled by screws. The antenna prototype is shown in Figure 7.18. The total size of this antenna is 66 mm \times 50 mm \times 8.4 mm. Figure 7.20 exhibits the measured frequency characteristics of the manufactured antenna used Agilent VNA E8363B at the University of Colorado, Boulder, USA. As seen, the -10 dB reflection coefficient is achieved within the operating band from 24.75 GHz to 40 GHz.

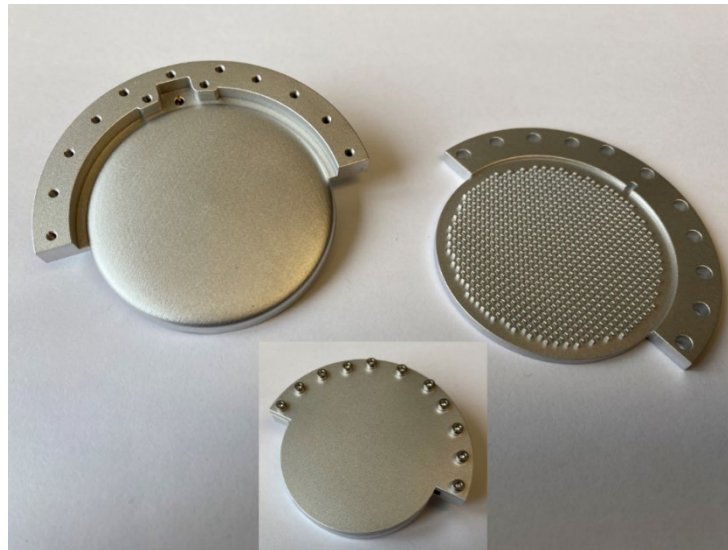


Figure 7.18. Fully metallic cylindrical Luneburg lens antenna prototype made of aluminum with CNC mill.

Figure 7.20 compares the simulated and measured frequency characteristics of the manufactured antenna. The measured reflection coefficient is in a good agreement with the simulation results. There is a slight frequency shift between the measured and simulated

values which might be attributed to the fabrication process variation and the measurement setup and calibration.

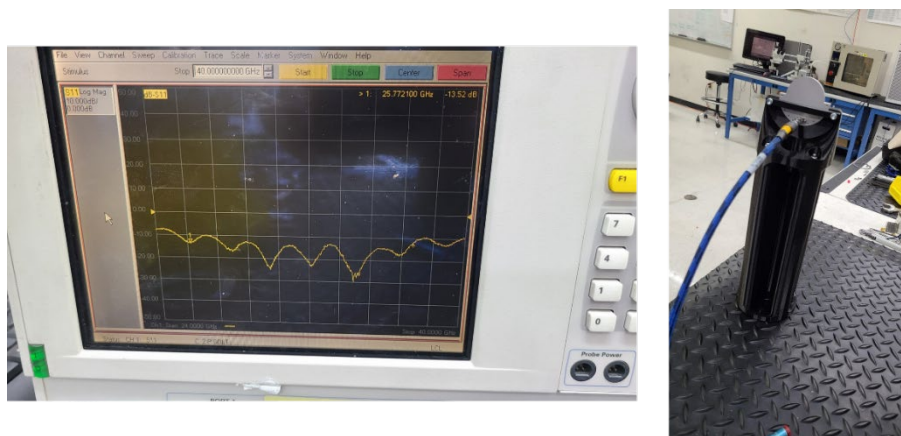


Figure 7.19. Measured input reflection coefficient of the fabricated prototype

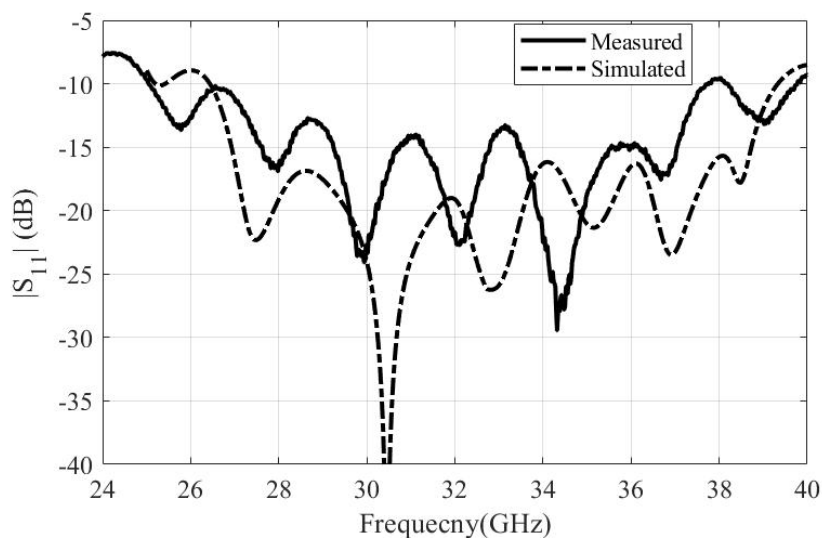


Figure 7.20. Comparison of simulated and measured input reflection coefficient of the fabricated prototype

Besides the reflection coefficient measurement, the antenna radiation pattern is measured in the anechoic chamber at the University of Colorado, Boulder (see Figure 7.21).



Figure 7.21. Radiation pattern setup in the anechoic chamber

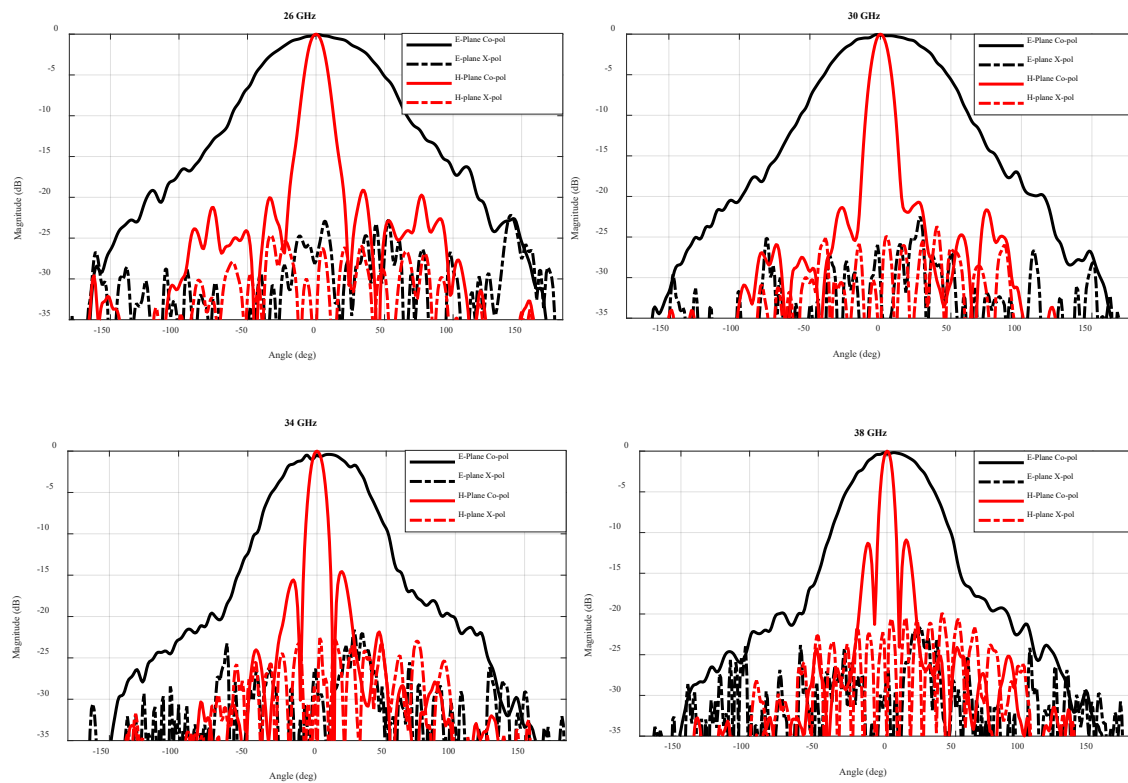


Figure 7.22 Measured radiation patterns in E- and H-planes at (a) 26, 30, 34, 38 GHz.

Figure 7.22 shows the measured radiation patterns in both E - and H-planes. There are four frequencies plotted: 26 GHz, 30 GHz, 34GHz, and 38 GHz. Each pattern is normalized with its own maximum level. As can be seen the side lobe level at all frequencies except 38 GHz is less than -15 dB, which is very good and match with the

simulation results. At 38 GHz as we expect from simulation results the side lobe level is about -12 dB in the H-plane. Moreover, the measured cross polarization level in both planes are less than -20 dB. Figure 7.24 illustrates both measurement of the peak total realized gain and directivity. The measured results show good agreement with the simulation results. The overall gain of the antenna over the frequency range from 26-40 GHz is more than 13 dB.

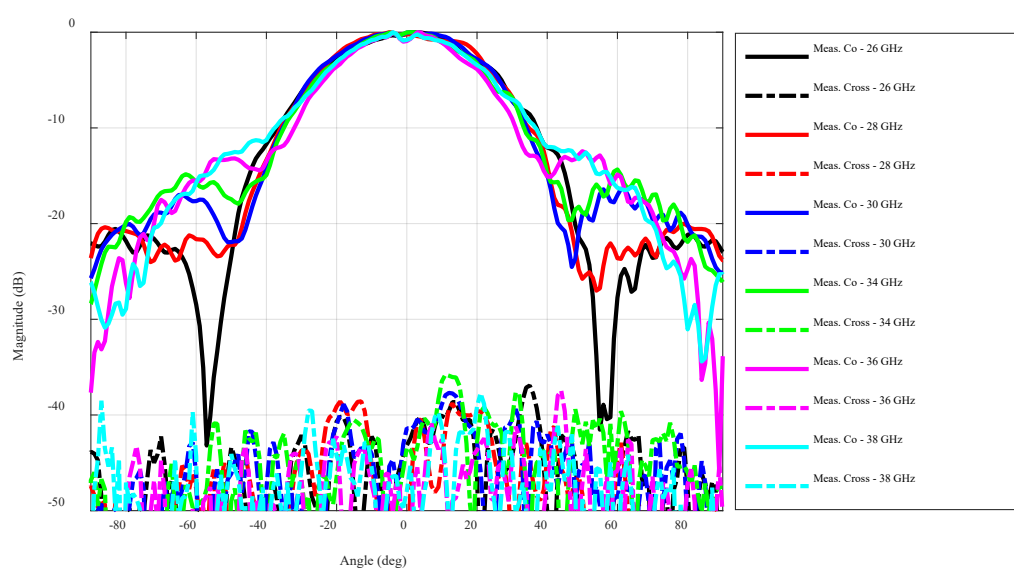


Figure 7.23. Measured radiation patterns in E-plane at (a) 26, 28, 30, 34, 38 GHz.

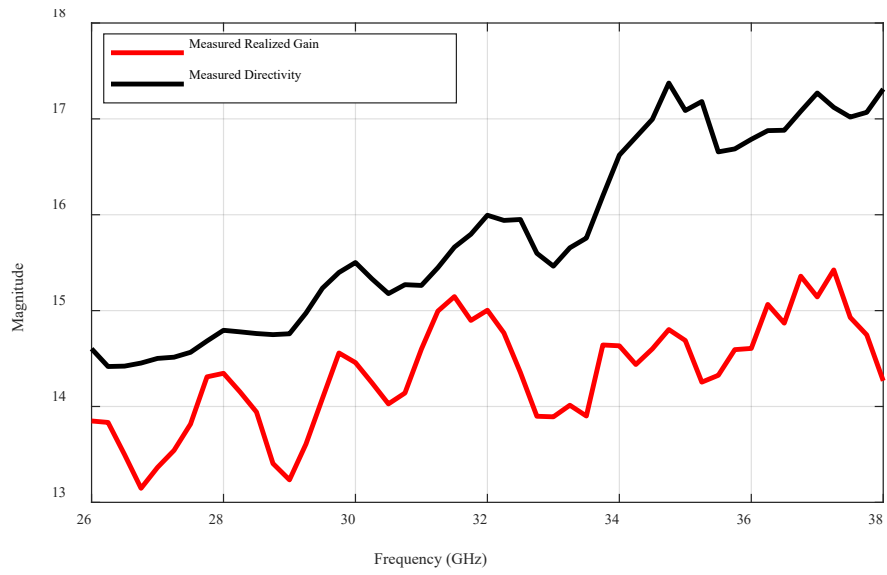


Figure 7.24. Measured peak realized gain and directivity

CHAPTER EIGHT: CONCLUSIONS

The presented dissertation is an effort to investigate, and develop, high gain and beam steerable antennas for new generations of wireless communication systems. Different cost-effective low profile designs of high gain and beam-steerable antennas have been designed and manufactured in this dissertation.

8.1 Summary

The proposed 4×4 high gain array antenna is designed based on the conventional horn antenna technology composed of a multi-stepped aperture structure, having a smooth transition from waveguide feed to free space. The feed part of the antenna is designed based on the standard WR-15 waveguide. Then, dielectric loading approach is applied in this design to improve antenna performance in terms of gain and sidelobe level. Further, the parameters of the dielectric disk also functioned to control frequency response of the antenna. The antenna is designed at 60 GHz band for short range indoor point to point wireless applications covering frequency range from 58 – 66 GHz. Considering the feeding network of the antenna, the antenna has a wideband performance. One of the goals in designing this antenna was to make the antenna more cost-effective, and this was accomplished by this design and manufactured by simply milling machine technique process, and the price of the antenna prototype was low. According to the fabricated results, experimental results show good agreement with simulated results. The -10 dB reflection coefficient is achieved within the operating band from 57.7 GHz to 64.7 GHz corresponding to the gain of higher than 23 dBi with larger than 66 % antenna efficiency.

Furthermore, from the tolerance analysis in HFSS software for the stepped profile of the antenna, the antenna has good performance due to manufacturing variations.

Millimeter wave backhaul links face challenges due to propagation loss and sensitivity to blockage. Therefore, another requirement for 5G backhaul antennas is their compatibility for multiple beam patterns. The beam steering feature is required, because it helps to focus signals in a concentrated beam that is very directive, and reducing signal blockage, thus decreasing interference among different users. Therefore, as another goal of this dissertation we presented some designs of multibeam cylindrical Luneburg lens antennas that could cover a large angular scanning range and provide wide bandwidth. Therefore, cost-effective low-profile cylindrical Luneburg lens antennas based on PPW technology for future communication networks has been designed and manufactured. The proposed lens designs are composed of two parallel metal plates in which a thin layer of a dielectric plate is sandwiched between the two metal plates. The GRIN property of the lens has been approximately obtained by PPW partially filled with dielectric material. These antennae designed based on rectangular waveguide feed element for narrow band (27.5-28.5 GHz) and wideband (Ka-band) applications. The antennas are fabricated and the simulation results are in good agreement with fabrication results. The antennas with nine feed elements provide a scan capability of $\pm 32^\circ$.

The proposed wideband lens antenna with a low profile and integrated feed elements provides about 46.7% of bandwidth ($|S_{11}| \leq -10$ dB) covering a frequency band ranging from 23.6 - 38 GHz. It also exhibits excellent propagation characteristics with only a 2.7 dB maximum gain variation with sidelobe levels lower than -18 dB over the entire bandwidth. In addition, with a multi-feed system, the antenna presents a beam switching

capability of $\pm 32^\circ$ in the azimuth plane with a gain fluctuation of less than 0.4 dB and sidelobes levels of less than -14 dB over the entire scan range. The results show that the proposed antenna features a simple structure while supporting wider bandwidth and lower sidelobes levels when compared to that of PPW Luneburg-based lens antennas. One of the main advantages of the proposed antenna is its compact and simple wideband feed element.

Finally, in order to reduce the dielectric losses of the lens part in the cylindrical lens antennas which become more prominent and affect the efficiencies of the antennas in mmWave band, we studied and introduced an air-filled fully metallic lens antenna. The antenna composed of PPW wherein the bottom plate of PPW is loaded with metallic posts in a periodic profile. Actually, the geometry and periodicity of the metallic post as the unit cell manipulate the properties of electromagnetic waves to achieve a sufficient effective refractive index. Further, the upper plate of the antenna is designed with a curved surface to improve the radiation and impedance matching. In this work, considering the equal-sized metallic posts and simplicity of the feeding part, a low loss wideband lens is presented.

8.2 Future Work

- The main possible improvement of the current full metal lens antenna is to increase antenna aperture for higher gain applications. The antenna can be implemented for both fixed beam and multiple beam applications. Considering the overall height and compact feature of the antenna, it can be integrated with any other passive RF components in wireless systems. As the feed part of the antenna is simplified, it can also be applied for higher frequency applications.
- Moreover, in order to improve antenna performance in terms of radiation pattern, the profile of the top plate of the PPW can be modified to lower sidelobe levels.

Optimizing the curvature of the top plate with an exponential profile instead of having a multi-stepped structure might simplify the complexity of fabrication.

- One issue in designing wideband LL antennas is the feed part of antenna, the proposed low profile feed part has the potential to be applied in any other designs of LL antennas for wideband applications. The wideband feed part of the antenna without any multi-stepped profile might ease antenna design and fabrication process.

REFERENCES

- [1] D. K. Cheng, “Field and Wave Electromagnetics,” *IEEE Antennas and Propagation Society Newsletter*, vol. 28, no. 2. Addison-Wesley, pp. 27–28, 1986.
- [2] Y. Miura, J. Hirokawa, M. Ando, Y. Shibuya, and G. Yoshida, “Double-layer full-corporate-feed hollow-waveguide slot array antenna in the 60-GHz band,” *IEEE Trans. Antennas Propag.*, vol. 59, no. 8, pp. 2844–2851, Aug. 2011.
- [3] A. Vosoogh, “Thesis for the Degree of Licentiate of Engineering Towards Gap Waveguide Array Antenna for Millimeter Wave Applications.”
- [4] A. Zaman, P. K. to appear in H. of Antenna, and U. 2016, “Gap waveguides for mmWave antenna systems and electronic packaging.”
- [5] D. Zarifi, A. Farahbakhsh, and A. U. Zaman, “A Gap Waveguide-Fed Wideband Patch Antenna Array for 60-GHz Applications,” *IEEE Trans. Antennas Propag.*, vol. 65, no. 9, pp. 4875–4879, 2017.
- [6] A. A. Brazalez, L. Manholm, M. Johansson, O. Quevedo-Teruel, and J. Miao, “Investigation of a Ka-band Luneburg lens made of a glide-symmetric holey structure,” in *2017 International Symposium on Antennas and Propagation, ISAP 2017*, 2017, vol. 2017-Janua, pp. 1–2.
- [7] G. A. Akpakwu, B. J. Silva, G. P. Hancke, and A. M. Abu-Mahfouz, “A Survey on 5G Networks for the Internet of Things: Communication Technologies and Challenges,” *IEEE Access*, vol. 6, pp. 3619–3647, 2018.
- [8] “Wireless communications: Principles and practice, solutions manual — NYU Scholars.” [Online]. Available: <https://nyuscholars.nyu.edu/en/publications/wireless-communications-principles-and-practice-solutions-manual>. [Accessed: 03-Jan-2021].

- [9] T. S. Rappaport *et al.*, “Millimeter wave mobile communications for 5G cellular: It will work!,” *IEEE Access*, vol. 1, pp. 335–349, 2013.
- [10] D. Lockie and D. Peck, “High-data-rate millimeter-wave radios,” *IEEE Microw. Mag.*, vol. 10, no. 5, pp. 75–83, Aug. 2009.
- [11] Xue Yang, Jie Liu, Feng Zhao, and N. H. Vaidya, “A vehicle-to-vehicle communication protocol for cooperative collision warning,” in *The First Annual International Conference on Mobile and Ubiquitous Systems: Networking and Services, 2004. MOBIQUITOUS 2004.*, pp. 114–123.
- [12] M. T. Ghasr, S. Kharkovsky, R. Bohnert, B. Hirst, and R. Zoughi, “30 GHz Linear High-Resolution and Rapid Millimeter Wave Imaging System for NDE,” *IEEE Trans. Antennas Propag.*, vol. 61, no. 9, pp. 4733–4740, Sep. 2013.
- [13] J. V. Evans, “Satellite systems for personal communications,” *Proc. IEEE*, vol. 86, no. 7, pp. 1325–1341, Jul. 1998.
- [14] R. C. Daniels and R. W. Heath, “60 GHz wireless communications: Emerging requirements and design recommendations,” *IEEE Veh. Technol. Mag.*, vol. 2, no. 3, pp. 41–50, Sep. 2007.
- [15] S. Rangan, T. S. Rappaport, and E. Erkip, “Millimeter-wave cellular wireless networks: Potentials and challenges,” *Proc. IEEE*, vol. 102, no. 3, pp. 366–385, 2014.
- [16] P. Smulders, “Exploiting the 60 GHz band for local wireless multimedia access: Prospects and future directions,” *IEEE Commun. Mag.*, vol. 40, no. 1, pp. 140–147, 2002.
- [17] S. Drabowitch, A. Papiernik, H. D. Griffiths, J. Encinas, and B. L. Smith, *Modern antennas*. 2005.
- [18] U. J. Lewark, J. Antes, J. Walheim, J. Timmermann, T. Zwick, and I. Kallfass, “Link budget analysis for future E-band gigabit satellite communication links (71-76 and 81-84 GHz),” *CEAS Sp. J.*, vol. 4, no. 1–4, pp. 41–46, Jun. 2013.

- [19] M. Marcus and B. Pattan, "Millimeter wave propagation: Spectrum management implications," *IEEE Microwave Magazine*, vol. 6, no. 2, pp. 54–62, Jun-2005.
- [20] M. A. Matin, "Review on millimeter wave Antennas-Potential candidate for 5G enabled applications," *Adv. Electromagn.*, vol. 5, no. 3, pp. 98–105, 2016.
- [21] J. Zhang, X. Ge, Q. Li, M. Guizani, and Y. Zhang, "5G Millimeter-Wave Antenna Array: Design and Challenges," *IEEE Wirel. Commun.*, vol. 24, no. 2, pp. 106–112, Apr. 2017.
- [22] S. M. Hashemi, V. Nayyeri, M. Soleimani, and A. R. Mallahzadeh, "Designing a compact-optimized planar dipole array antenna," *IEEE Antennas Wirel. Propag. Lett.*, vol. 10, pp. 243–246, 2011.
- [23] J. Huang and A. C. Densmore, "Microstrip yagi array antenna for mobile satellite vehicle application," *IEEE Trans. Antennas Propag.*, vol. 39, no. 7, pp. 1024–1030, 1991.
- [24] G. Leggett *et al.*, "Method and system for a smart antenna utilizing leaky wave antennas," Jun. 2004.
- [25] D. Pozar, "Considerations for millimeter wave printed antennas," *IEEE Trans. Antennas Propag.*, vol. 31, no. 5, pp. 740–747, Sep. 1983.
- [26] E. Levine, G. Malamud, S. Shtrikman, and D. Treves, "A Study of Microstrip Array Antennas with the Feed Network," *IEEE Trans. Antennas Propag.*, vol. 37, no. 4, pp. 426–434, 1989.
- [27] A. L. Vera López, S. K. Bhattacharya, C. A. Donado Morcillo, and J. Papapolymerou, "Novel low loss thin film materials for wireless 60 GHz application," in *Proceedings - Electronic Components and Technology Conference*, 2010, pp. 1990–1995.
- [28] G. Six, G. Prigent, E. Rius, G. Dambrine, and H. Happy, "Fabrication and characterization of low-loss TFMS on silicon substrate up to 220 GHz," in *IEEE Transactions on Microwave Theory and Techniques*, 2005, vol. 53, no. 1, pp. 301–304.

- [29] E. Levine, G. Malamud, S. Shtrikman, and D. Treves, "A Study of Microstrip Array Antennas with the Feed Network," *IEEE Trans. Antennas Propag.*, vol. 37, no. 4, pp. 426–434, 1989.
- [30] P. S. Hall and C. M. Hall, "COPLANAR CORPORATE FEED EFFECTS IN MICROSTRIP PATCH ARRAY DESIGN.," *IEE Proc. H Microwaves, Antennas Propag.*, vol. 135, no. 3, pp. 180–186, 1988.
- [31] T. Seki, N. Honma, K. Nishikawa, and K. Tsunekawa, "A 60-GHz multilayer parasitic microstrip array antenna on LTCC substrate for system-on-package," *IEEE Microw. Wirel. Components Lett.*, vol. 15, no. 5, pp. 339–341, 2005.
- [32] Z. Qi, X. Li, J. Chu, J. Xiao, and H. Z.-I. J. of M. and, "High-gain cavity backed patch antenna arrays at 140 GHz based on LTCC technology," *cambridge.org*.
- [33] J. Xu, Z. N. Chen, X. Qing, and W. Hong, "Bandwidth Enhancement for a 60 GHz Substrate Integrated Waveguide Fed Cavity Array Antenna on LTCC," *IEEE Trans. Antennas Propag.*, vol. 59, no. 3, pp. 826–832, Mar. 2011.
- [34] A. E. I. Lamminen, J. Säily, and A. R. Vimpari, "60-GHz patch antennas and arrays on LTCC with embedded-cavity substrates," *IEEE Trans. Antennas Propag.*, vol. 56, no. 9, pp. 2865–2874, 2008.
- [35] S. H. Wi *et al.*, "Package-level integrated antennas based on LTCC technology," *IEEE Trans. Antennas Propag.*, vol. 54, no. 8, pp. 2190–2197, Aug. 2006.
- [36] J. Xu, Z. Chen, X. Qing, W. H.-I. T. on, and undefined 2010, "Bandwidth enhancement for a 60 GHz substrate integrated waveguide fed cavity array antenna on LTCC," *ieeexplore.ieee.org*.
- [37] J. A. Harrington, "A Review of IR Transmitting, Hollow Waveguides," 2000.
- [38] F. Xu and K. Wu, "Guided-wave and leakage characteristics of substrate integrated waveguide," in *IEEE Transactions on Microwave Theory and Techniques*, 2005, vol. 53, no. 1, pp. 66–72.

- [39] B. Cao, H. Wang, Y. Huang, and J. Zheng, "High-Gain L-Probe Excited Substrate Integrated Cavity Antenna Array with LTCC-Based Gap Waveguide Feeding Network for W-Band Application," *IEEE Trans. Antennas Propag.*, vol. 63, no. 12, pp. 5465–5474, 2015.
- [40] J. Wu, Y. J. Cheng, and Y. Fan, "A wideband high-gain high-efficiency hybrid integrated plate array antenna for V-band inter-satellite links," *IEEE Trans. Antennas Propag.*, vol. 63, no. 4, pp. 1225–1233, 2015.
- [41] M. Bozzi, M. Pasian, L. Perregrini, and K. Wu, "On the losses in substrate integrated waveguides," in *Proceedings of the 37th European Microwave Conference, EUMC*, 2007, pp. 384–387.
- [42] Xiao-Ping Chen, Ke Wu, Liang Han, and Fanfan He, "Low-Cost High Gain Planar Antenna Array for 60-GHz Band Applications," *IEEE Trans. Antennas Propag.*, vol. 58, no. 6, pp. 2126–2129, 2010.
- [43] Q. Zhu, K. B. Ng, C. H. Chan, and K. M. Luk, "Substrate-Integrated-Waveguide-Fed Array Antenna Covering 57-71 GHz Band for 5G Applications," *IEEE Trans. Antennas Propag.*, vol. 65, no. 12, pp. 6298–6306, 2017.
- [44] M. Li and K. M. Luk, "A low-profile unidirectional printed antenna for millimeter-wave applications," *IEEE Trans. Antennas Propag.*, vol. 62, no. 3, pp. 1232–1237, 2014.
- [45] O. Kramer, T. Djerafi, and K. Wu, "Very small footprint 60 GHz stacked Yagi antenna array," *IEEE Trans. Antennas Propag.*, vol. 59, no. 9, pp. 3204–3210, 2011.
- [46] Y. Li and K. M. Luk, "60-GHz substrate integrated waveguide fed cavity-backed aperture-coupled microstrip patch antenna arrays," *IEEE Trans. Antennas Propag.*, vol. 63, no. 3, pp. 1075–1085, 2015.
- [47] J. Xu, Z. N. Chen, X. Qing, and W. Hong, "140-GHz TE₂₀-mode dielectric-loaded SIW Slot antenna array in LTCC," *IEEE Trans. Antennas Propag.*, vol. 61, no. 4, pp. 1784–1793, 2013.

- [48] M. Zhang, J. Hirokawa, and M. Ando, "An E-band partially corporate feed uniform slot array with laminated quasi double-layer waveguide and virtual PMC terminations," *IEEE Trans. Antennas Propag.*, vol. 59, no. 5, pp. 1521–1527, May 2011.
- [49] S. S. Oh, J. W. Lee, M. S. Song, and Y. S. Kim, "Two-layer slotted-waveguide antenna array with broad reflection/gain bandwidth at millimetre-wave frequencies," *IEE Proc. Microwaves, Antennas Propag.*, vol. 151, no. 5, pp. 393–398, Oct. 2004.
- [50] B. Lee, K. Jung, and S. H. Yang, "High-efficiency planar slotarray antenna with a single waveguide-fed cavity-backed subarray," *Microw. Opt. Technol. Lett.*, vol. 43, no. 3, pp. 228–231, Nov. 2004.
- [51] Y. Kimura, T. Hirano, J. Hirokawa, and M. Ando, "Alternating-phase fed single-layer slotted waveguide arrays with chokes dispensing with narrow wall contacts," in *IEE Proceedings: Microwaves, Antennas and Propagation*, 2001, vol. 148, no. 5, pp. 295–301.
- [52] H. Kirino and K. Ogawa, "A 76 GHz multi-layered phased array antenna using a non-metal contact metamaterial waveguide," *IEEE Trans. Antennas Propag.*, vol. 60, no. 2 PART 2, pp. 840–853, Feb. 2012.
- [53] P. S. Kildal, E. Alfonso, A. Valero-Nogueira, and E. Rajo-Iglesias, "Local metamaterial-based waveguides in gaps between parallel metal plates," *IEEE Antennas Wirel. Propag. Lett.*, vol. 8, pp. 84–87, 2009.
- [54] P.-S. Kildal, "WAVEGUIDES AND TRANSMISSION LINES IN GAPS BETWEEN PARALLEL CONDUCTING SURFACES," 2011.
- [55] D. Sievenpiper, L. Zhang, R. F. J. Broas, E. Yablonovitch, and N. G. Alexopolous, "Corrections to 'High-Impedance Electromagnetic Surfaces with a Forbidden Frequency Band,'" *IEEE Trans. Microw. Theory Tech.*, vol. 48, no. 4, p. 620, 2000.

- [56] E. Rajo-Iglesias and P. S. Kildal, "Numerical studies of bandwidth of parallel-plate cut-off realised by a bed of nails, corrugations and mushroom-type electromagnetic bandgap for use in gap waveguides," *IET Microwaves, Antennas Propag.*, vol. 5, no. 3, pp. 282–289, Feb. 2011.
- [57] P. S. Kildal, A. U. Zaman, E. Rajo-Iglesias, E. Alfonso, and A. Valero-Nogueira, "Design and experimental verification of ridge gap waveguide in bed of nails for parallel-plate mode suppression," *IET Microwaves, Antennas Propag.*, vol. 5, no. 3, pp. 262–270, Feb. 2011.
- [58] E. Rajo-Iglesias and P. S. Kildal, "Groove gap waveguide: A rectangular waveguide between contactless metal plates enabled by parallel-plate cut-off," in *EuCAP 2010 - The 4th European Conference on Antennas and Propagation*, 2010.
- [59] H. Raza, J. Yang, P. S. Kildal, and E. Alfonso Alos, "Microstrip-ridge gap waveguide-study of losses, bends, and transition to WR-15," *IEEE Trans. Microw. Theory Tech.*, vol. 62, no. 9, pp. 1943–1952, 2014.
- [60] A. A. Brazalez, E. Rajo-Iglesias, J. L. Vazquez-Roy, A. Vosoogh, and P. S. Kildal, "Design and Validation of Microstrip Gap Waveguides and Their Transitions to Rectangular Waveguide, for Millimeter-Wave Applications," *IEEE Trans. Microw. Theory Tech.*, vol. 63, no. 12, pp. 4035–4050, Dec. 2015.
- [61] A. U. Zaman and P. S. Kildal, "Wide-band slot antenna arrays with single-layer corporate-feed network in ridge gap waveguide technology," *IEEE Trans. Antennas Propag.*, vol. 62, no. 6, pp. 2992–3001, 2014.
- [62] E. Pucci, E. Rajo-Iglesias, J. L. Vázquez-Roy, and P. S. Kildal, "Planar dual-mode horn array with corporate-feed network in inverted microstrip gap waveguide," *IEEE Trans. Antennas Propag.*, vol. 62, no. 7, pp. 3534–3542, 2014.
- [63] S. A. Razavi, P. S. Kildal, L. Xiang, E. A. Alós, and H. Chen, " 2×2 -Slot element for 60-GHz planar array antenna realized on two doubled-sided PCBs using SIW cavity and EBG-type soft surface fed by microstrip-ridge gap waveguide," *IEEE Trans. Antennas Propag.*, vol. 62, no. 9, pp. 4564–4573, Sep. 2014.

- [64] S. Patela, "Fabrication methods of planar waveguides and related structures Photonics technologies," pp. 1–26.
- [65] A. U. Zaman and P. S. Kildal, "Different gap waveguide slot array configurations for mmwave fixed beam antenna application," in *2016 10th European Conference on Antennas and Propagation, EuCAP 2016*, 2016.
- [66] D. Kim, M. Zhang, J. Hirokawa, and M. Ando, "Design and fabrication of a dual-polarization waveguide slot array antenna with high isolation and high antenna efficiency for the 60 GHz band," *IEEE Trans. Antennas Propag.*, vol. 62, no. 6, pp. 3019–3027, 2014.
- [67] A. Vosoogh and P. S. Kildal, "Corporate-Fed Planar 60-GHz Slot Array Made of Three Unconnected Metal Layers Using AMC Pin Surface for the Gap Waveguide," *IEEE Antennas Wirel. Propag. Lett.*, vol. 15, pp. 1935–1938, 2016.
- [68] Y. Miura, J. Hirokawa, M. Ando, Y. Shibuya, and G. Yoshida, "Double-layer full-corporate-feed hollow-waveguide slot array antenna in the 60-GHz band," *IEEE Trans. Antennas Propag.*, vol. 59, no. 8, pp. 2844–2851, Aug. 2011.
- [69] D. Zarifi, A. Farahbakhsh, A. U. Zaman, and P. S. Kildal, "Design and Fabrication of a High-Gain 60-GHz Corrugated Slot Antenna Array with Ridge Gap Waveguide Distribution Layer," *IEEE Trans. Antennas Propag.*, vol. 64, no. 7, pp. 2905–2913, Jul. 2016.
- [70] A. Vosoogh, P. S. Kildal, and V. Vassilev, "Wideband and High-Gain Corporate-Fed Gap Waveguide Slot Array Antenna with ETSI Class II Radiation Pattern in V-Band," *IEEE Trans. Antennas Propag.*, vol. 65, no. 4, pp. 1823–1831, Apr. 2017.
- [71] E. Brookner, "Phased arrays and radars past, present and future," *Microwave Journal*, vol. 49, no. 1, pp. 24–46, 2006.
- [72] R. Bansal, "Antenna theory; analysis and design," *Proc. IEEE*, vol. 72, no. 7, pp. 989–990, 2008.
- [73] C. W. Baek, S. Song, C. Cheon, Y. K. Kim, and Y. Kwon, "2-D mechanical beam steering antenna fabricated using MEMS technology," *IEEE MTT-S Int. Microw. Symp. Dig.*, vol. 3, pp. 211–214, 2001.

- [74] D. Rodrigo, L. Jofre, and B. A. Cetiner, "Circular beam-steering reconfigurable antenna with liquid metal parasitics," *IEEE Trans. Antennas Propag.*, vol. 60, no. 4, pp. 1796–1802, 2012.
- [75] Jung-Chih Chiao, Yiton Fu, Iao Mak Chio, M. DeLisio, and Lih-Yuan Lin, "MEMS reconfigurable Vee antenna," in *ieeexplore.ieee.org*, 2003, pp. 1515–1518.
- [76] M. Kaynak, İ. Tekin, M. H. Nemati, B. Tillack, and E. Öztürk, "SiGe process integrated full-360° microelectromechanical systems-based active phase shifter for W-band automotive radar," *IET Microwaves, Antennas Propag.*, vol. 8, no. 11, pp. 835–841, Aug. 2014.
- [77] A. H. Naqvi and S. Lim, "Review of recent phased arrays for millimeter-wave wireless communication," *Sensors (Switzerland)*, vol. 18, no. 10. 2018.
- [78] R. Luneberg, "Mathematical Theory of Optics. Providence," 1944.
- [79] O. Quevedo-Teruel, M. Ebrahimpouri, and F. Ghasemifard, "Lens Antennas for 5G Communications Systems," *IEEE Commun. Mag.*, vol. 56, no. 7, pp. 36–41, Jul. 2018.
- [80] L. Xue and V. F. Fusco, "24 GHz automotive radar planar Luneburg lens," *IET Microwaves, Antennas Propag.*, vol. 1, no. 3, p. 624, 2007.
- [81] M. Kamran Saleem, H. Vettikaladi, M. A. S. Alkanhal, and M. Himdi, "Lens Antenna for Wide Angle Beam Scanning at 79 GHz for Automotive Short Range Radar Applications," *IEEE Trans. Antennas Propag.*, vol. 65, no. 4, pp. 2041–2046, Apr. 2017.
- [82] M. Kamran Saleem, H. Vettikaladi, M. A. S. Alkanhal, and M. Himdi, "Lens Antenna for Wide Angle Beam Scanning at 79 GHz for Automotive Short Range Radar Applications," *IEEE Trans. Antennas Propag.*, vol. 65, no. 4, pp. 2041–2046, 2017.
- [83] J. R. Huynen, "Theory and design of a class of luneberg lenses," in *1958 IRE WESCON Convention Record*, 1958, pp. 219–230.

- [84] J. Thornton and K. C. Huang, *Modern Lens Antennas for Communications Engineering*. 2013.
- [85] S. Lee and Y. Lo, *Antenna Handbook: Antenna Theory*. 1993.
- [86] J. S.-I. A. and P. Magazine and U. 1995, "A Luneberg-lens update," *ieeexplore.ieee.org*.
- [87] K. W. Kim and Y. Rahmat-Samii, "Spherical Luneburg lens antennas: Engineering characterizations including air gap effects," in *IEEE Antennas and Propagation Society International Symposium, 1998 Digest - Antennas: Gateways to the Global Network - Held in conjunction with: USNC/URSI National Radio Science Meeting*, 1998, vol. 4, pp. 2062–2065.
- [88] B. Fuchs, L. Le Coq, O. Lafond, S. Rondineau, and M. Himdi, "Design optimization of multishell Luneburg lenses," *IEEE Trans. Antennas Propag.*, vol. 55, no. 2, pp. 283–289, 2007.
- [89] H. Mosallaei, S. Member, and Y. Rahmat-samii, "Nonuniform Luneburg and Two-Shell Lens Antennas: Radiation Characteristics and Design Optimization," *ieeexplore.ieee.org*, vol. 49, no. 1, pp. 60–69, 2001.
- [90] A. V. Boriskin, A. Vorobyov, and R. Sauleau, "Two-shell radially symmetric dielectric lenses as low-cost analogs of the luneburg lens," *IEEE Trans. Antennas Propag.*, vol. 59, no. 8, pp. 3089–3093, 2011.
- [91] M. Liang *et al.*, "A 3-D Luneburg Lens Antenna Fabricated by Polymer Jetting Rapid Prototyping," *IEEE Trans. Antennas Propag.*, vol. 62, no. 4, pp. 1799–1807, 2014.
- [92] J. Bor, O. Lafond, H. Merlet, P. Le Bars, and M. Himdi, "Technological process to control the foam dielectric constant application to microwave components and antennas," *IEEE Trans. Components, Packag. Manuf. Technol.*, vol. 4, no. 5, pp. 938–942, 2014.
- [93] K. Sato and H. Ujiie, "A plate Luneburg lens with the permittivity distribution controlled by hole density," *Electron. Commun. Japan, Part I Commun. (English Transl. Denshi Tsushin Gakkai Ronbunshi)*, vol. 85, no. 9, pp. 1–12, Sep. 2002.

- [94] N. Nikolic, G. L. James, A. Hellicar, and K. Greene, "Quarter-sphere Luneburg lens scanning antenna," in *2012 15th International Symposium on Antenna Technology and Applied Electromagnetics, ANTEM 2012*, 2012.
- [95] D. H. Kwon and D. H. Werner, "Transformation electromagnetics: An overview of the theory and applications," *IEEE Antennas Propag. Mag.*, vol. 52, no. 1, pp. 24–46, 2010.
- [96] C. Mateo-Segura, A. Dyke, H. Dyke, S. Haq, and Y. Hao, "Flat luneburg lens via transformation optics for directive antenna applications," *IEEE Trans. Antennas Propag.*, vol. 62, no. 4, pp. 1945–1953, 2014.
- [97] T. Komljenovic, R. Sauleau, Z. Sipus, and L. Le Coq, "Layered circular-cylindrical dielectric lens antennas-Synthesis and height reduction technique," *IEEE Trans. Antennas Propag.*, vol. 58, no. 5, pp. 1783–1788, 2010.
- [98] M. Šarbort and T. Tyc, "Spherical media and geodesic lenses in geometrical optics," *J. Opt. (United Kingdom)*, vol. 14, no. 7, p. 075705, Jul. 2012.
- [99] Q. Liao, N. J. G. Fonseca, and O. Quevedo-Teruel, "Compact Multibeam Fully Metallic Geodesic Luneburg Lens Antenna Based on Non-Euclidean Transformation Optics," *IEEE Trans. Antennas Propag.*, vol. 66, no. 12, pp. 7383–7388, 2018.
- [100] C. Z. Hua, X. D. Wu, N. Yang, and W. Wu, "Millimeter-wave homogenous cylindrical lens antenna for multiple fan-beam scanning," *J. Electromagn. Waves Appl.*, vol. 26, no. 14–15, pp. 1922–1929, 2012.
- [101] C. Hua, X. Wu, N. Yang, and W. Wu, "Air-filled parallel-plate cylindrical modified luneburg lens antenna for multiple-beam scanning at millimeter-wave frequencies," *IEEE Trans. Microw. Theory Tech.*, vol. 61, no. 1, pp. 436–443, 2013.
- [102] C. H. Walter, "Surface-Wave Luneberg Lens Antennas," *IRE Trans. Antennas Propag.*, vol. 8, no. 5, pp. 508–515, 1960.
- [103] Y. J. Park, A. Herschlein, and W. Wiesbeck, "A photonic bandgap (PBG) structure for guiding and suppressing surface waves in millimeter-wave antennas," *IEEE Trans. Microw. Theory Tech.*, vol. 49, no. 10 II, pp. 1854–1859, Oct. 2001.

- [104] Y. J. Park and W. Wiesbeck, "Angular independency of a parallel-plate Luneburg lens with hexagonal lattice and circular metal posts," *IEEE Antennas Wirel. Propag. Lett.*, vol. 1, pp. 128–130, 2002.
- [105] I. Uchendu and J. Kelly, "Survey of beam steering techniques available for millimeter wave applications," *Prog. Electromagn. Res. B*, vol. 68, no. 1, pp. 35–54, 2016.
- [106] W. Hong *et al.*, "Multibeam Antenna Technologies for 5G Wireless Communications," *IEEE Trans. Antennas Propag.*, vol. 65, no. 12, pp. 6231–6249, Dec. 2017.
- [107] M. Khatun, C. Guo, L. Moro, D. Matolak, and H. Mehrpouyan, "Millimeter-wave path loss at 73 GHz in indoor and outdoor airport environments," in *IEEE Vehicular Technology Conference*, 2019, vol. 2019-Sept.
- [108] O. Quevedo-Teruel, M. Ebrahimpouri, and F. Ghasemifard, "Lens antennas for 5G communications systems," *IEEE Commun. Mag.*, vol. 56, no. 7, pp. 36–41, Jul. 2018.
- [109] Y. Wang, J. Li, L. Huang, Y. Jing, A. Georgakopoulos, and P. Demestichas, "5G mobile: Spectrum broadening to higher-frequency bands to support high data rates," *IEEE Veh. Technol. Mag.*, vol. 9, no. 3, pp. 39–46, Sep. 2014.
- [110] R. C. Johnson and H. Jasik, "Antenna engineering handbook /2nd edition/," *mgH*, 1984.
- [111] Q. Cheng, H. F. Ma, and T. J. Cui, "Broadband planar Luneburg lens based on complementary metamaterials," *Appl. Phys. Lett.*, vol. 95, no. 18, p. 181901, Nov. 2009.
- [112] K. Sato and H. Ujiie, "A plate Luneburg lens with the permittivity distribution controlled by hole density," *Electron. Commun. Japan (Part I Commun.)*, vol. 85, no. 9, pp. 1–12, Sep. 2002.
- [113] X. Wu and J. J. Laurin, "Fan-beam millimeter-wave antenna design based on the cylindrical Luneburg lens," *IEEE Trans. Antennas Propag.*, vol. 55, no. 8, pp. 2147–2156, Aug. 2007.

- [114] Q. Liao, N. J. G. Fonseca, and O. Quevedo-Teruel, "Compact Multibeam Fully Metallic Geodesic Luneburg Lens Antenna Based on Non-Euclidean Transformation Optics," *IEEE Trans. Antennas Propag.*, vol. 66, no. 12, pp. 7383–7388, Dec. 2018.
- [115] O. Quevedo-Teruel, J. Miao, M. Mattsson, A. Algaba-Brazalez, M. Johansson, and L. Manholm, "Glide-Symmetric Fully Metallic Luneburg Lens for 5G Communications at Ka-Band," *IEEE Antennas Wirel. Propag. Lett.*, vol. 17, no. 9, pp. 1588–1592, Sep. 2018.
- [116] H. T. Chou and Z. Da Yan, "Parallel-plate luneburg lens antenna for broadband multibeam radiation at millimeter-wave frequencies with design optimization," *IEEE Trans. Antennas Propag.*, vol. 66, no. 11, pp. 5794–5804, Nov. 2018.
- [117] H. F. Ma and T. J. Cui, "Three-dimensional broadband and broad-angle transformation-optics lens," *Nat. Commun.*, vol. 1, no. 8, pp. 1–7, Nov. 2010.
- [118] T. Driscoll *et al.*, "Performance of a three dimensional transformation-optical-flattened Lüneburg lens," *Opt. Express*, vol. 20, no. 12, p. 13262, Jun. 2012.
- [119] Y. Su and Z. N. Chen, "A flat dual-polarized transformation-optics beams scanning luneburg lens antenna using PCB-Stacked gradient index metamaterials," *IEEE Trans. Antennas Propag.*, vol. 66, no. 10, pp. 5088–5097, Oct. 2018.
- [120] A. B. Numan, J. F. Frigon, and J. J. Laurin, "Printed W-Band multibeam antenna with luneburg lens-based beamforming network," *IEEE Trans. Antennas Propag.*, vol. 66, no. 10, pp. 5614–5619, Oct. 2018.
- [121] A. Dhouibi, S. N. Burokur, A. De Lustrac, and A. Priou, "Compact metamaterial-based substrate-integrated Luneburg lens antenna," *IEEE Antennas Wirel. Propag. Lett.*, vol. 11, pp. 1504–1507, 2012.
- [122] M. Bosiljevac, M. Casaletti, F. Caminita, Z. Sipus, and S. MacI, "Non-uniform metasurface luneburg lens antenna design," *IEEE Trans. Antennas Propag.*, vol. 60, no. 9, pp. 4065–4073, 2012.

- [123] H. C. Chou, N. L. Tung, and M. Ng Mou Kehn, "The Double-Focus Generalized Luneburg Lens Design and Synthesis Using Metasurfaces," *IEEE Trans. Antennas Propag.*, vol. 66, no. 9, pp. 4936–4941, Sep. 2018.
- [124] M. Liang, W. R. Ng, K. Chang, K. Gbele, M. E. Gehm, and H. Xin, "A 3-D luneburg lens antenna fabricated by polymer jetting rapid prototyping," *IEEE Trans. Antennas Propag.*, vol. 62, no. 4, pp. 1799–1807, 2014.
- [125] W. E. Kock, "Metal-Lens Antennas," *Proc. IRE*, vol. 34, no. 11, pp. 828–836, 1946.
- [126] O. Quevedo-Teruel, M. Ebrahimpouri, and M. Ng Mou Kehn, "Ultrawideband Metasurface Lenses Based on Off-Shifted Opposite Layers," *IEEE Antennas Wirel. Propag. Lett.*, vol. 15, pp. 484–487, Dec. 2016.
- [127] J. D. Joannopoulos, S. G. Johnson, J. N. Winn, and R. D. Meade, *Photonic crystals: Molding the flow of light*. 2011.